

Institut für Angewandte Photophysik
Fachrichtung Physik
Fakultät Mathematik und Naturwissenschaften
Technische Universität Dresden

Ultrafast Dynamics in Quasi-One-Dimensional Organic Molecular Crystals

Self-Assembled Monolayers of Photochromic Molecules

Dissertation
zur Erlangung des akademischen Grades
Doctor rerum naturalium
(Dr. rer. nat.)

vorgelegt von
Tobias W. Canzler
geboren am 28. April 1973 in Burgstädt

Dresden 2002



Eingereicht am 06. August 2002

1. Gutachter: Prof. Dr. K. Leo
2. Gutachter: Prof. Dr. V.M. Agranovich
3. Gutachter: Prof. Dr. H. Giessen

Verteidigt am 26. September 2002

Contents

I	Ultrafast Dynamics in Quasi-1D Organic Molecular Crystals	7
1	Introduction	9
1.1	The Model System of MePTCDI	11
2	Optical Properties of Organic Molecules and Crystals	15
2.1	Isolated Molecules (Monomers)	15
2.1.1	Optical Excitation	16
2.1.2	Relaxation	20
2.2	Dimers	21
2.2.1	Excimers	23
2.3	Crystal Excitons	24
2.3.1	Excitons in the Quasi-1D Crystal of MePTCDI	27
2.4	Dynamic (Vibrational) Properties	31
2.5	Exciton Self-Trapping	32
2.6	Open Questions	34
3	Techniques of Time-Resolved Spectroscopy	37
3.1	Generation and Control of Ultrashort Light Pulses	37
3.1.1	Linear Pulse Propagation	37
3.1.2	Pulse Compression and Shaping, Characterization	41
3.1.3	Generation and Amplification of White-Light Pulses	45
3.2	Spectroscopic Methods	49
3.2.1	Transient Absorption Spectroscopy	50
3.2.2	Degenerate Four-Wave Mixing	55
3.2.3	Time-Resolved Luminescence	56
3.3	Experimental Setups	57
4	Experimental Results and Discussion	61
4.1	Excitonic Relaxation	61
4.1.1	Radiative Recombination from Relaxed Excited States	62
4.1.2	The Nature of Relaxed Excited States	65
4.1.3	Ultrafast Exciton Dynamics	69
4.2	Dephasing of Free Exciton Transitions	77
4.3	Vibronic and Phononic Wave Packets	82
4.3.1	Frequency vs. Time-Domain Vibrational Spectroscopy	88
5	Conclusion	91

II Self-Assembled Monolayers of Photochromic Molecules	95
6 Introduction	97
6.1 Photochromic Reactions	99
6.2 Organic Thin Films	101
6.2.1 Concept of Self-Assembly	102
6.2.2 Status of Research / Open Questions	103
7 Techniques for Studying Monolayers	105
7.1 Scanning Tunneling Microscopy (STM)	105
7.2 Infrared (IR) Spectroscopy	106
7.3 Second Harmonic Generation (SHG)	108
8 Experimental Results and Discussion	113
8.1 Azobenzene-thiols on Au(111)	113
8.2 IR Spectroscopy	116
8.3 Second Harmonic Generation (SHG)	119
9 Conclusion	123
Bibliography	125
Publications	133

Abbreviations

1D	one-dimensional
3D	three-dimensional
AzoC ₆	4-phenylazophenoxyhexane-1-thiol
BBO	β -barium borate crystal
CTE	charge-transfer exciton
DFWM	degenerate four-wave mixing
EFISH	electric field-induced second-harmonic generation
FE	FRENKEL exciton
FTIR-RAS	FOURIER transform infrared-reflection absorption spectroscopy
FWHM	full width at half maximum
GVD	group-velocity dispersion
LBO	lithium triborate crystal
LC	liquid crystal
MePTCDI	N-N'-dimethylperylene-3,4,9,10-dicarboximide
NOPA	non-collinear optical parametric amplifier
OLED	organic light-emitting diode
OMC	organic molecular crystal
O.D.	optical density = absorbance = $-\lg T$
OPA	optical parametric amplifier
PMT	photo-multiplier tube
PTCDA	3,4,9,10-perylenetetracarboxylic dianhydride
RRS	resonant RAMAN scattering
RSIRS	resonant stimulated-impulsive RAMAN scattering
SAM	self-assembled monolayer
SHG	second-harmonic generation
SSHG	surface second-harmonic generation
STE	self-trapped exciton
STM	scanning tunneling microscopy
SPM	self-phase modulation
TA	transient absorption spectroscopy
TOD	third-order dispersion
TR	time resolved
WLG	white-light generation

Part I

**Ultrafast Dynamics in Quasi-1D
Organic Molecular Crystals**

1 Introduction

Organic molecules in solid phase form molecular crystals which differ considerably in their optical, electronic and mechanical properties from conventional inorganic solids such as covalent (atomic) or ionic crystals. This is mainly due to weak intermolecular interaction forces of the VAN DER WAALS type with bonding energies considerably lower than that of covalent or ionic bonds. The energy range of typical VAN DER WAALS intermolecular bonds ($E_{\text{vdW}} = 10^{-3} - 10^{-2}\text{eV}$) is by several orders of magnitude smaller than the intramolecular covalent bond energies ($E_{\text{cov}} = 2 - 4\text{eV}$) of aromatic molecules. In contrary to covalent and ionic crystals, where the electronic structure of valence electrons is largely determined by the crystal formation, weak intermolecular interaction forces produce only moderate changes in the electronic structure of molecules on formation of the solid phase, and, as a result, *neutral* molecules retain their identity.

The additional structural level given by the individual molecules is one main reason for interest in molecular crystals: The resources of organic chemistry provides nearly unlimited variety of molecules, which can be used to design crystals with highly specialized features. Several million organic compounds are known today, and many are commercially available.

The technological potential of organic materials concerning electronics and optoelectronics was not explored for a long time. In the 1970s, it was discovered that certain types of polymeric material can conduct electricity almost as efficiently as copper [1]. In 1987, TANG and VAN SLYKE [2] demonstrated highly efficient organic light-emitting diodes (OLED). Nowadays, the power efficiency of OLEDs exceeds that of incandescence lamps and approaches that of discharge lamps. Thus, OLED technology is very promising for lighting purposes. However, the main vision for OLED technology is in the field of large area and flat display applications.¹ Nowadays, such displays are already commercial on small scales. Further applications are in sight, e.g. electrical sensors or batteries made entirely from plastics.

In particular, molecules with a conjugated π -electron system usually exhibit semi-conducting behavior. The discovery of controlled n- and p-type doping of organic molecular systems, very similar to classical silicon technology, paved the way for organic electronics and optoelectronics [3]. All-organic thin layer devices such as transistors and diodes used for integrated circuits have already been realized. This points to one of the disadvantages of organic materials: their low carrier mobilities, which are about $1\text{cm}^2/\text{Vs}$ at room temperature for the best-ordered thin films (pentacene

¹The main advantages of OLED displays are low power consumption, low production costs, video capability, and they are self-emitters and thus viewing angle independent. In contrast, the established liquid crystal displays (LCD) only change the polarization state of the illuminating light, an effect which is viewing angle dependent.

and oligothiophene [4]), compared with mobilities somewhere between $100\text{cm}^2/\text{Vs}$ and $10^4\text{cm}^2/\text{Vs}$ for conventional semiconductors. This suggests that, in the end, organic electronics will not apply to high-speed devices as used in, i.e. telecommunication.

The group of organic materials for (opto)-electronic device applications is usually divided into polymers and "small molecules". In this context, small is meant relative to the size of a polymer. Typical representatives for small molecules contain 10 (naphthalene), 20 (perylene) or 60 (C_{60}) carbon atoms. In this thesis, we only deal with crystals of small molecules. In particular, we aim at *quasi-one-dimensional crystals*. By naming quasi one-dimensional (quasi-1D), we mean that in the crystal structure the intermolecular interactions along one lattice constant are significantly stronger than along the other two. Then, the crystal can be considered as a two-dimensional array of 1D stacks. As a model system for quasi-1D crystals, we use MePTCDI crystals.

The strong temperature dependence of the electronic bandwidths and mobilities of Organic Molecular Crystals (OMC) can be explained by a strong electron-phonon interaction. A crossover from bandlike charge transport with mobilities up to several thousand cm^2/Vs at low temperature to an incoherent hopping motion at high temperatures was observed [5]. Because of the soft lattice of VAN DER WAALS bonded molecular semiconductors, this is expected to be much more pronounced compared to covalently bonded materials, such as Si or Ge. Therefore, a detailed investigation of the exciton-phonon interaction is required. In particular, in quasi-1D materials electron-phonon coupling might play a dominant role: Theory predicts that self-trapping of free excitons always occurs for any finite exciton-phonon coupling strength (see Sec. 2.5).

In the following thesis, we will investigate excitonic and phononic properties of MePTCDI. By use of various time-resolved experimental techniques, we investigate the relaxation of excitons and phonons in time domain. The subjects of interest are threefold: First, we observe the relaxation of free excitons in the lowest exciton band to totally relaxed exciton states. Second, the homogeneity of excitonic transitions is topic of our experiments. By measuring the macroscopic polarization decay of excitonic transitions the homogeneous linewidth of these transitions can be determined. Third, the investigation of both molecular and crystal phononic properties is achieved in the time domain. Oscillations of coherent phonon wave packets and their damping are studied.

This part of the thesis is organized as follows: In the next section, we will briefly introduce our model system for a quasi-1D organic molecular crystal - MePTCDI. The specific advantages of this system will be motivated. In Chapter 2, we will give the necessary theoretical background for describing optical properties of OMCs. Additionally, the current status of modeling the optical properties of MePTCDI is presented. In Section 2.6, we address the open questions concerning this system we are going to answer. In Chapter 3, we introduce the experimental setups and techniques. As the experimental setups are rather extensive, including, e.g. the realization of a home-built optical amplifier, they are given in some detail. Therefore, it is indispensable to introduce some concepts of nonlinear optics. The necessary background for data interpretation is provided. All experimental results are given in Chapter 4. We present numerous results covering the range from the slowest relaxation processes concerning luminescence decay in the ns-time up to the fastest processes. In this context, the dephasing of excitonic transitions is the fastest relaxation process with time constants of less than 100fs. Conclusions and an outlook for further investigations are presented

in Chapter 5.

1.1 The Model System of MePTCDI

A number of perylene derivatives form quasi-one dimensional crystals, for instance the prominent representatives PTCDA and MePTCDI (for an overview see [6, 7]). These molecules have a planar conjugated π -electron system which causes strong absorption in the visible. The substituent at the periphery of the molecule, for MePTCDI the group $N - CH_3$, is sensitively responsible for the energetic position of the absorption maximum. The monomeric absorption is given in Fig. 2.3.

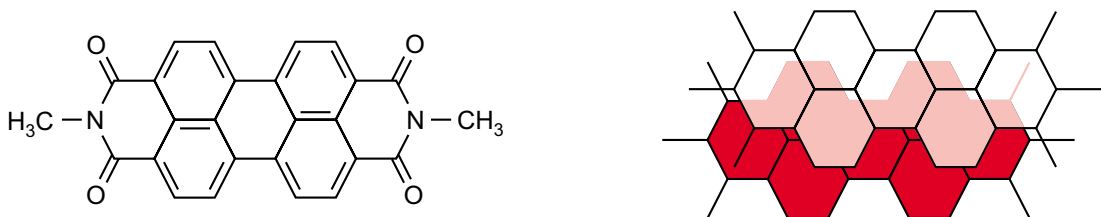


Figure 1.1: Left: Chemical structure of MePTCDI (N,N'-dimethylperylene-3,4,9,10-dicarboximide). Right: Molecular pair within the 1D stack. The offset of the molecules perpendicular to the molecular planes is 3.40\AA .

A characteristic property of the quasi-1D crystal of MePTCDI is its strong intermolecular overlap in the one-dimensional stacks. In MePTCDI, the molecular planes have a distance of 3.40\AA [6], which is on the order of the plane distance in graphite (3.35\AA). Thus, a nearest-neighbor pair within the stack has a sandwich-like geometry with the molecules shifted with respect to each other within the molecular plane as shown in Fig.1.1. Still, a large fraction ($\approx 50\%$) of the conjugated electron systems lies directly above each other [8]. This leads to a strong mutual penetration of the molecular wave functions. We refer to this situation by the term "strong intermolecular overlap". An immediate consequence expected for this system are large electronic bandwidths. Hence, such materials should develop qualitative similarities to covalent crystals with the advantage of high charge carrier mobility, which is technologically extremely important. However, experimental mobilities in the quasi-1D crystal PTCDA are about $3 \cdot 10^{-2} \text{cm}^2/\text{Vs}$ (vapor-deposited layers at room temperature [9]). Presently, it is not clear whether higher mobilities can actually be achieved or if other effects (strong electron-phonon coupling) will compensate the advantage of larger intermolecular overlap.

In the framework of this thesis, we have mainly worked with polycrystalline thin (approx. 15nm) films of MePTCDI grown by physical vapor deposition (PVD) in high vacuum ($p < 10^{-3}\text{Pa}$) on a room-temperature glass substrate. Before deposition, the material has been purified by gradient sublimation. The average size of the polycrystallites within the layer will be in the range of $20 - 100\text{nm}$. This estimate results from atomic force microscopy (AFM) and X-ray diffraction measurements on 100nm films of MePTDI and PTCDA on various substrates [10, 11, 12]. There are no systematic studies on the preferential orientation of the micro-crystallites relative to the substrate for different substrate materials. For thin layers of MePTCDI on a polymer film, the (102)

plane was found to be mainly parallel to the substrate. In other words, the molecular planes are mainly parallel to the substrate.

Thin films of MePTCDI are of technological importance for the usage in low-cost devices as OLEDs, organic solar cells, or as transport layers for organic electronics [13, 14]. However, to understand intrinsic crystal properties of MePTCDI it is favorable to compare the results with measurements on single crystals. The used crystals are of maximum size of about $300 \times 300 \times 3000 \mu\text{m}$ and stem from multi-stage gradient sublimation (see Fig. 1.2). They were kindly provided by the group of N. KARL (Stuttgart). The long lateral surfaces of the needle-like crystal are (011), resp. the equivalent planes $(0 - 11)$, $(01 - 1)$, $(0 - 1 - 1)$. The crystallographic investigations to obtain the orientation of the molecules within the crystals were also performed in this group.

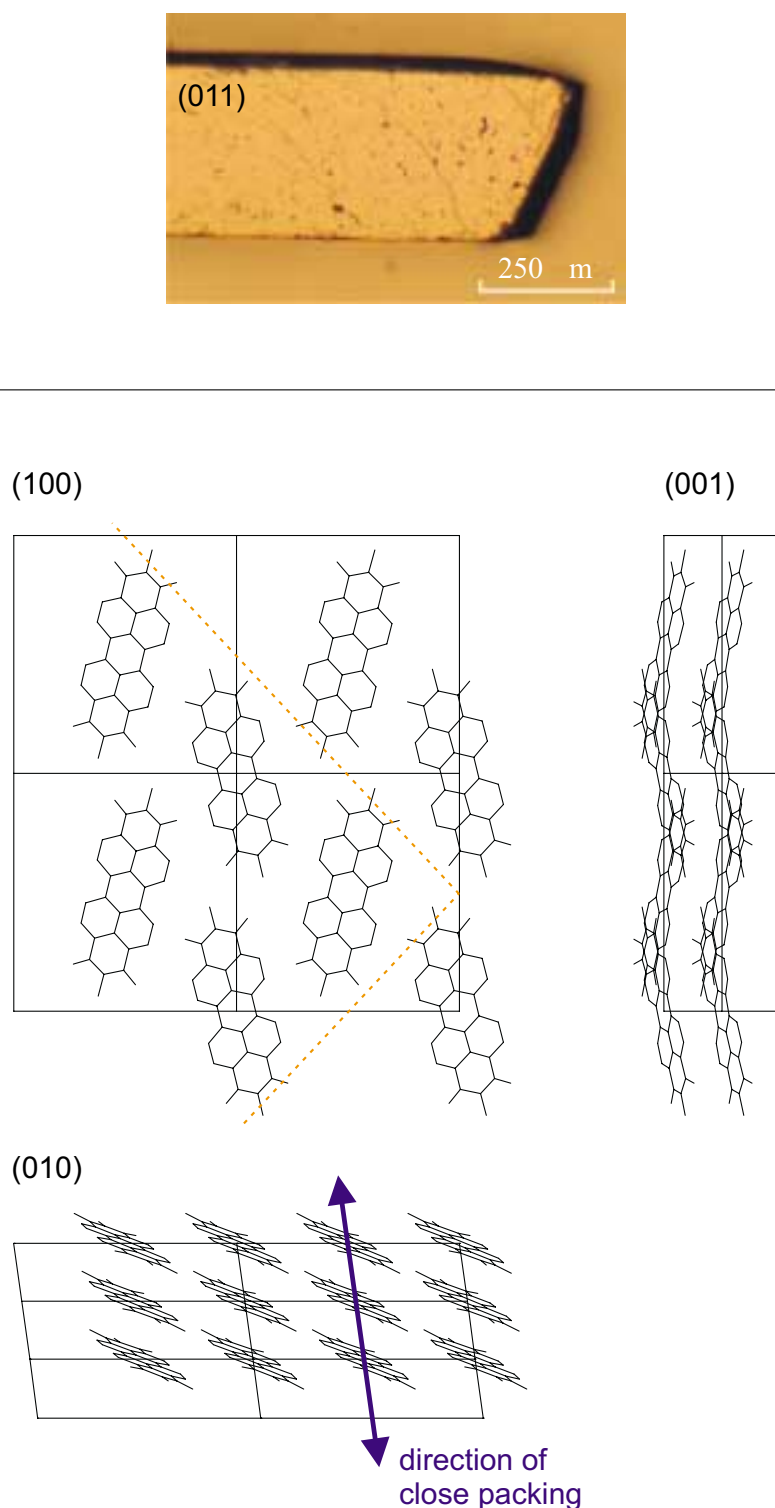


Figure 1.2: Crystal and crystal structure of MePTCDI. Top: Picture of a single crystal of MePTCDI. The long lateral surfaces of the needle-like crystal are (011), resp. the equivalent planes $(0\bar{1}1)$, $(01\bar{1})$, $(0\bar{1}\bar{1})$. Bottom: Shown are the projections of $2 \times 2 \times 3$ unit cells onto the b-c plane (100), the a-b plane (001) and onto the a-c plane (010). The crystal structure is monoclinic, space group $P2_1/c$, $Z=2$ molecules per unit cell, $a = 3.87\text{\AA}$, $b = 15.58\text{\AA}$, $c = 14.60\text{\AA}$, $\beta = 97.65^\circ$ (data from [15]). The dashed lines show possible cleavage faces of the crystal.

2 Optical Properties of Organic Molecules and Crystals

As argued in the introduction, the nature of excited states of organic molecular crystals (OMC) is mainly determined by the excited states of the corresponding isolated molecules. First, we introduce the independent problem of an isolated molecule. This is the indispensable basis for the theoretical description of the crystal. Afterwards, we treat the case of two interacting molecules, the so-called dimer. Already this smallest possible aggregate shows some properties which are important for crystal formation. Finally, the concepts for the description of excited states of OMCs are introduced. We present a model, especially developed for the case of quasi-one-dimensional OMCs, and apply it to the MePTCDI crystal.

2.1 Isolated Molecules (Monomers)

An isolated molecule consists of nuclei and electrons which interact with each other. The nonrelativistic HAMILTON operator is given by:

$$H_{\text{mol}} = \underbrace{T_{\text{el}}(\mathbf{r}) + V_{\text{el-nuc}}(\mathbf{r}, \mathbf{R}) + V_{\text{el-el}}(\mathbf{r})}_{H_{\text{el}}} + \underbrace{T_{\text{nuc}}(\mathbf{R}) + V_{\text{nuc-nuc}}(\mathbf{R})}_{H_{\text{nuc}}} \quad (2.1)$$

with T_{el} and T_{nuc} being the kinetic energy of electrons and nuclei (\mathbf{r}, \mathbf{R} representing the set of electron and nuclear coordinates, respectively). Since both kinds of particles are charged, we find COULOMB pair interaction between electrons $V_{\text{el-el}}$, between nuclei $V_{\text{nuc-nuc}}$ and between electrons and nuclei $V_{\text{el-nuc}}$.

The stationary properties of the molecular system defined so far are contained in the solutions of the time-independent SCHRÖDINGER equation:

$$H_{\text{mol}}\Psi(\mathbf{r}, \mathbf{R}) = E \cdot \Psi(\mathbf{r}, \mathbf{R}) \quad (2.2)$$

Up to now, the problem is described exactly. However, (2.2) does not tell much about what we are aiming at, namely optical absorption and emission spectra. The way to solve this equation is described in many textbooks in detail [16, here], we only want to point out the main ideas and assumptions in the following.

The practical solution of (2.2) makes use of the fact that due to the large mass difference $m_{\text{el}}/M_{\text{nuc}} < 10^{-3}$, electrons will respond instantaneously to any changes in the nuclear configuration. In other words, the interaction between nuclei and electrons,

$V_{\text{el-nuc}}$, is modified due to the motion of the nuclei only *adiabatically* and does not cause transition between different electronic states (BORN-OPPENHEIMER approximation). That motivates a separation of the molecular wave function:

$$\Psi(\mathbf{r}, \mathbf{R}) = \psi^f(\mathbf{r}, \mathbf{R}) \phi^{f\nu}(\mathbf{R}) \quad (2.3)$$

where f numbers the electronic and ν the vibronic levels. This leads to a separation of the HAMILTONIAN into an electronic and a nuclear part. The electronic part (neglecting the electron spin)

$$H_{\text{el}}|\psi^f\rangle = E_f|\psi^f\rangle \quad (2.4)$$

will *parametrically* depend on the set of nuclear coordinates as well. Because the nuclear coordinates are now only parameters, $V_{\text{el-nuc}}$ becomes a one-particle operator and we find for the nuclear HAMILTONIAN:

$$H_{\text{nuc}}|\phi^{f\nu}\rangle = (T_{\text{nuc}} + \underbrace{V_{\text{nuc-nuc}} + W_{\text{el}}}_U)|\phi^{f\nu}\rangle = W_{f\nu}|\phi^{f\nu}\rangle \quad (2.5)$$

which contains the electronic energy as effective potential W_{el} .

For small elongation, the potential U in (2.5) can be described as harmonic. After a transformation of the nuclear coordinates \mathbf{R} into the *normal mode coordinates* \mathbf{Q} , which describe the elongation of the nuclei from the ground state equilibrium position, (2.5) can be separated into $3N - 6$ independent equations (for a N -atomic molecule, $N > 2$). In one dimension, the ground state is represented by:

$$U_0(Q) = \frac{1}{2}M_{\text{eff}}\omega^2Q^2 \quad (2.6)$$

Here, the effective mass M_{eff} and the normal mode frequency ω have been introduced. It is noteworthy that the harmonic oscillations of the individual atoms within a normal mode have all the same frequency ω , but different amplitudes determined by their masses. In this potential, the vibronic wave functions $\phi^{0\nu}$ with their eigenenergies $\hbar\omega(\nu + 1/2)$ are formed, as shown in Fig. 2.1.

2.1.1 Optical Excitation

We now address the issue of the relation between normal modes belonging to different electronic states. For simplicity, we will assume that ground state and all excited states can be described by the *same* normal mode coordinate. In general, the equilibrium geometry of the molecule is different for the ground-state ($f = 0$) and the first electronically excited-state ($f = 1$). The new equilibrium position is shifted by g . Since the potential $U_1(Q)$ in the excited-state depends on all electrons but only a few electrons take part in the excitation, the curvature of $U_1(Q)$ differs not strongly from that of the ground state. Hence, the vibronic spacing is rather similar: In the case of MePTCDI in chloroform, the difference of vibronic spacing of the dominating mode derived from absorption and emission spectra amounts to 4meV compared to $\hbar\omega = 0.17\text{eV}$ (values from Fig. 2.3).

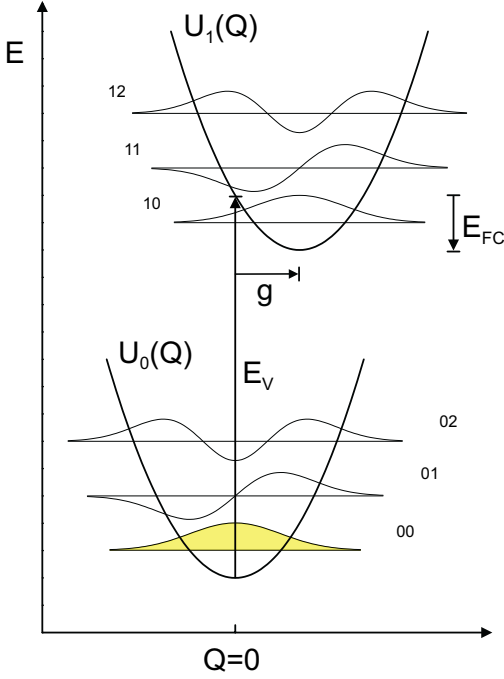


Figure 2.1: Schematic energy diagram for the vibronic potentials of ground- and excited-state which are described by the same normal coordinate Q . The excited-state potential is displaced on the Q -axis by the exciton-phonon coupling parameter g , which corresponds to a vibrational reorganization energy E_{FC} . The vibronic wave functions $\phi^{f\nu}$ are shown for the lowest three levels.

A reorganization energy $E_{FC} = \hbar\omega g^2$ (FRANCK-CONDON energy) is gained by a rearrangement of the nuclei along the normal coordinate Q by g , in simple words: by vibronic relaxation. The excited-state potential can be well described for small elongations (e.g. harmonic potentials assumed) by

$$U_1(Q) = \frac{1}{2}M_{\text{eff}}\omega^2(Q - g)^2 - E_{FC} + E_V \quad (2.7)$$

where E_V stands for the vertical excitation energy. Optical absorption corresponds to the transition $|\Psi^{00}\rangle \rightarrow |\Psi^{1\nu}\rangle$, since for $\hbar\omega = 0.17\text{eV} \gg kT$ only the lowest vibrational level of the electronic ground state is occupied. The transition dipole moment is given by the matrix element with the dipole moment operator \vec{P} :

$$\vec{p}^\nu = \langle \Psi^{1\nu} | \vec{P} | \Psi^{00} \rangle \quad (2.8)$$

This matrix element refers to integration over all electron and nucleus coordinates. In the product representation (2.3), the vibronic part $\phi^{f\nu}$ only depends on the nucleus coordinates, whereas the electronic part ψ^f contains these nucleus coordinates as a variable. Electronic motion with a typical frequency of $2 \times 10^{15}\text{s}^{-1}$ is much faster than vibrational motion with a typical frequency of $3 \times 10^{13}\text{s}^{-1}$. As a result, the light-field vector of frequencies appropriate for an electronic excitation oscillates far too fast for the nuclei to follow it instantaneously, so the wave function for the nuclear motion is still nearly the same immediately after the optical transition. Such a transition can be visualized as transition from $Q \approx 0$ in the ground-state potential U_0 to $Q \approx 0$ in the excited-state potential U_1 , which is therefore called a vertical transition. This statement is known as the FRANCK-CONDON *principle* and thus, the integration in (2.8) can be split into an electronic and a vibronic matrix element:

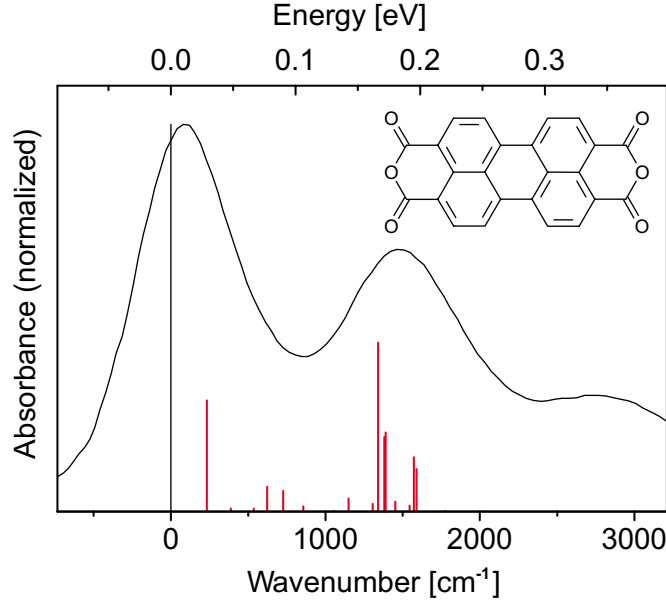


Figure 2.2: Vibrational modes of PTCDA according to [17]. The calculated modes are given as discrete vertical lines, representing the squared exciton-phonon coupling constant g^2 , normalized to the intensity of the 0-0 transition. Higher vibrational states are not shown. The optical absorption spectrum in $0.2\mu\text{M}$ solution of PTCDA is given for comparison. The spectrum is shifted by 2.37eV so that the 0-0 peak corresponds to zero vibrational energy.

$$\vec{p}^\nu = \underbrace{\langle \psi^1 | \vec{P} | \psi^0 \rangle}_{\vec{p}_{\text{el}}} \cdot \underbrace{\langle \phi^{1\nu} | \phi^{00} \rangle}_{s_\nu} \quad (2.9)$$

Here, we have introduced the electronic transition dipole moment of the lowest molecular excitation \vec{p}_{el} and the vibronic overlap factors s_ν . Thus, the oscillator strength F^ν for the ν -th transition with corresponding energy E^ν is given as

$$F^\nu = \frac{2m_e}{e^2\hbar^2} \cdot E^\nu |\vec{p}_{\text{el}}|^2 \cdot |s_\nu|^2. \quad (2.10)$$

The squared absolute values $|s_\nu|^2$ are called the *FRANCK-CONDON factors*. They determine the intensity distribution in the vibronic progression. From the graphic illustration in Fig. 2.1, the overlap factors can roughly be estimated. A detailed discussion of *FRANCK-CONDON* factors on the shape of electronic potential surfaces and the electron-phonon coupling constants g is provided in [16].

Molecules consisting of N atoms will have $3N - 6$ vibrational modes and the picture becomes more complicated: Instead of a single normal mode coordinate Q , a whole set Q_i with specific coupling constants g_i has to be considered. For each mode, vibrational quanta of specific energy can be excited and the various possible combinations may result in an unspecific absorption spectrum. However, only a limited number of modes with significant electron-phonon coupling will show up in absorption spectra. To illustrate this, we will give here the well investigated example of the perylene-derivative PTCDA. SCHOLZ et al. calculated the electronic and vibronic structure of

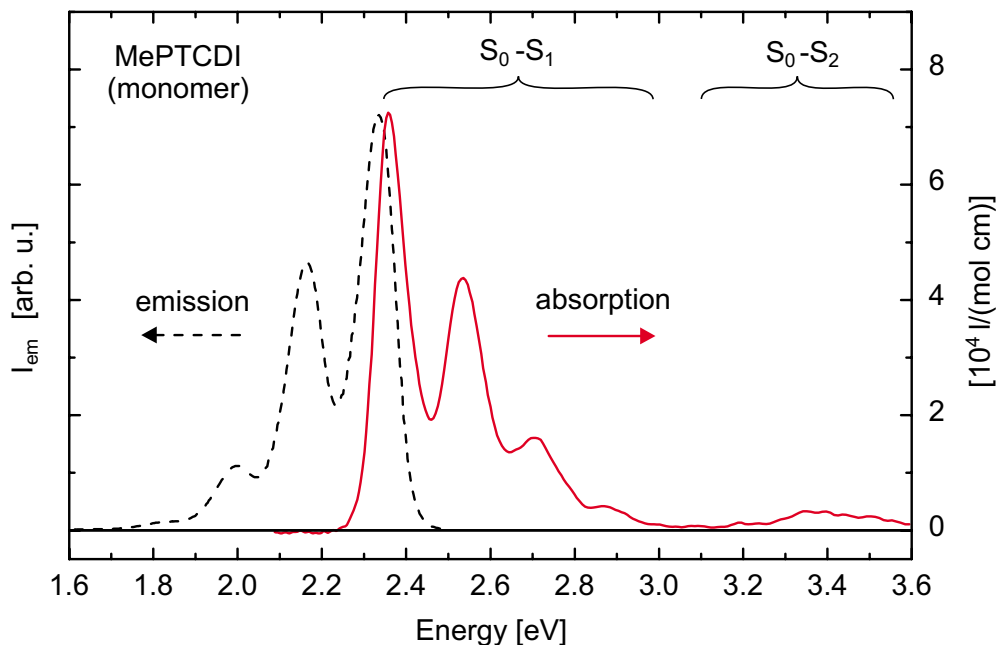


Figure 2.3: Absorption and fluorescence emission spectra of MePTCDI monomers. In terms of the involved orbitals, the S_0-S_1 absorption band is due to a $\pi\pi^*$ transition. The molecules are dissolved in chloroform with a concentration of $\leq 0.5\mu\text{mol/l}$ (adapted from [10]).

the monomer on the basis of a density-functional tight-binding method [17]. A comparison with experimental RAMAN spectra shows good agreement. With this model, the optical absorption spectrum is described by a superposition of all calculated modes and their harmonics. Introducing a sufficient broadening results in a nice agreement with the experimental absorption spectrum (see Fig. 2.2). Nevertheless, the optical absorption spectrum can be described sufficiently by one *effective vibrational mode*. This approximation will be used in the description of crystal spectra of MePTCDI in Sec. 2.3.1, whereas the results of the investigation of the full vibrational spectrum will be presented in Sec. 4.3.

Figure 2.3 shows the absorption spectrum of an MePTCDI solution in the range of the S_0-S_1 -vibronic progression. The simple scheme which is realized in Fig. 2.1 is able to explain the spectrum sufficiently: The lowest excited state is energetically well separated from higher states and it predominantly couples to an effective vibrational mode with a spacing of $\hbar\omega = 0.17\text{eV}$. The next higher optically allowed state is seen as a weak feature at $\approx 3.4\text{eV}$, which we label S_2 , independently of other dipole forbidden states that might lie below S_2 .

Up to now, we have neglected the influence of the electron spin. Taking into account the spin of the electronic system will lead to another classification of electronic states by their multiplicity, which is the number $2S+1$ of possible values of projecting the total spin vector on the direction of quantization. That leads to singlet states ($S=0$) and triplet states ($S=1$). The electric dipole and quadrupole operators do not act on spin. An electronic transition is spin allowed only if the multiplicities of the two states involved are identical. As a result, singlet-triplet absorption is practically not observable. Including spin-orbit coupling into the HAMILTONIAN will cause transi-

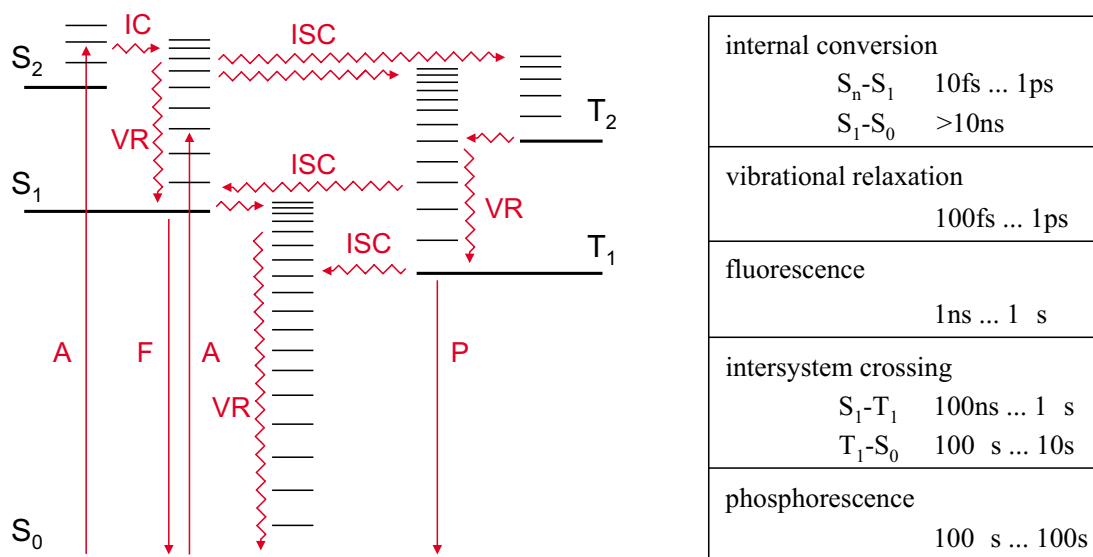


Figure 2.4: Energy scheme of a single molecule. Absorption (A) and emission processes are indicated by straight arrows (F = fluorescence, P = phosphorescence), radiationless processes by zigzag arrows (IC = internal conversion, ISC = intersystem crossing, VR = vibrational relaxation). Rough estimates of relaxation time ranges for molecules in solution, as taken from [18], are given in the table.

tions between states of different multiplicity, which is, however, negligible for molecules without heavy atoms.

2.1.2 Relaxation

Electronically excited states have only limited lifetimes. In general, several processes are responsible for the dissipation of the excess energy of an excited state. In the following we will concentrate only on photophysical pathways of deactivation (some photochemical processes will be dealt with in Part II of this thesis).

The electronically excited states are coupled to other electronic states as well as to the manifold of vibrational states. The excess energy gained by light absorption can be transferred to these states and dissipated through intramolecular processes as radiation (emission) or radiationless transitions. It can also be transferred to other molecules of the surrounding. The various intramolecular processes are schematically drawn in Fig. 2.4. This diagram displays the singlet states S_0 , S_1 , and S_2 as well as the triplet states T_1 and T_2 . The spacing between the vibrational levels decreases rapidly with increasing energy (due to anharmonicity of vibronic potentials), and the density of states increases very rapidly as the vibrational energy increases. Rotational levels have been neglected for the sake of clarity. Emission or luminescence is referred to as *fluorescence* or *phosphorescence*, depending on whether it corresponds to a spin-allowed or spin-forbidden transition, respectively. Similarly, radiationless transitions between states of the same and of a different multiplicity are known as *internal conversion* (IC) and *intersystem crossing* (ISC), respectively.

From Figure 2.4, it can be seen that a molecule can reach an excited vibrational level

of the electronically excited state S_1 either by the absorption of a photon of appropriate energy or by internal conversion from vibrational levels of a higher electronic state such as S_2 . In solution, *vibrational relaxation* (VR) to the vibrational ground state (or more accurately, to a BOLTZMANN distribution over the vibrational levels corresponding to thermal equilibrium) is ultrafast. From the zero-vibrational level of the S_1 state, the molecule either can return to the ground state S_0 by *fluorescence* (F), or it can reach the triplet state T_1 by *intersystem crossing* (ISC). After subsequent redistribution of excess vibrational energy, it can return to the ground state S_0 by phosphorescence. Radiationless deactivation from S_1 to S_0 can occur via *internal conversion* (IC) with subsequent vibrational relaxation (VR). Radiationless deactivation from T_1 to S_0 can occur by intersystem crossing followed by vibrational relaxation.

In many cases, intersystem crossing is fast enough to compete with fluorescence or even with vibrational relaxation. As indicated in Fig. 2.4, higher excited triplet states can be reached under such circumstances, and subsequent internal conversion and vibrational relaxation then proceed in the triplet manifold.

2.2 Dimers

In the preceding pages, the excitation and decay of excited states of single molecules and their respective emission and absorption spectra were described. To understand these properties for OMCs, it is helpful to spend some time with the smallest complex of molecules: the dimer. A (physical) dimer consists of two closely spaced molecules with purely physical interaction, no chemical bonding is involved. It is important to note the major differences that exist between excited-state properties of single molecules and those of small aggregates of such molecules.

A weak interaction of the molecules forming a dimer can be easily described using perturbation theory as done by KASHA [19]. Taking the non-interacting molecules with their particular HAMILTONIAN H_A and H_B as a starting point, the intermolecular potential H_{int} of the total HAMILTONIAN can be regarded as a perturbation term

$$H = H_A + H_B + H_{\text{int}} \quad (2.11)$$

Without interaction two equivalent states $|\psi_A\rangle$ of molecule A and $|\psi_B\rangle$ of molecule B are degenerate with an energy E_{isolated} . Switching on the the perturbation H_{int} will lead to a mixing of $|\psi_A\rangle$ and $|\psi_B\rangle$, and will end up in an energetic lowering and splitting of the dimer states:

$$E_{\pm} = 2E_{\text{isolated}} + W \pm \beta \quad (2.12)$$

with

$$\begin{aligned} 2E_{\text{isolated}} &= \langle \psi_A | H_A + H_B | \psi_A \rangle = \langle \psi_B | H_A + H_B | \psi_B \rangle \\ W &= \langle \psi_A | H_{\text{int}} | \psi_A \rangle = \langle \psi_B | H_{\text{int}} | \psi_B \rangle \\ \beta &= \langle \psi_A | H_{\text{int}} | \psi_B \rangle = \langle \psi_B | H_{\text{int}} | \psi_A \rangle \end{aligned}$$

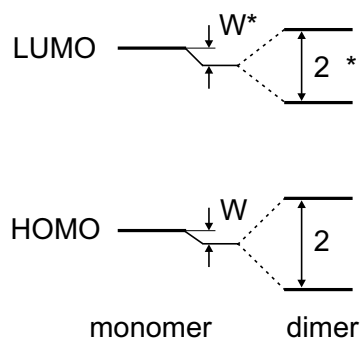


Figure 2.5: Scheme of the molecular and dimer orbital levels.

with the term W representing the VAN DER WAALS interaction energy (an energy lowering) between the states of the molecules. The term β , the *exciton splitting term*, represents an interaction energy due to the exchange of excitation energy between the two molecules. The accompanying dimer states are given as:

$$\psi_{\pm} = \frac{1}{\sqrt{2}}(\psi_A \pm \psi_B) \quad (2.13)$$

With dimer formation, the major spectral changes that have been observed experimentally are (a) a displacement of emission and absorption bands relative to the monomer, (b) a splitting of spectral lines with a corresponding change in the polarization properties, (c) a variation in the selection rules and oscillator strength for optical transitions, (d) changes in the molecular vibrational frequencies and the introduction of intermolecular lattice modes, and as a consequence, (e) the dimer spectrum is usually considerably broader than the monomer spectrum.

The selection rules for optical allowed transitions can be derived in a quasi-classical vector picture of transition dipole moments. The exciton splitting term β becomes in the point-dipole point-dipole approximation

$$\beta = \frac{\mathbf{M}_A \cdot \mathbf{M}_B}{r^3} - \frac{3(\mathbf{M}_A \cdot \mathbf{r})(\mathbf{M}_B \cdot \mathbf{r})}{r^5} \quad (2.14)$$

where \mathbf{M}_A and \mathbf{M}_B are the transition moments in molecule A and B , respectively, and \mathbf{r} is the position vector of the A dipole referred to the B dipole as origin. For the case of identical molecules with coplanar, inclined transition dipoles, (2.14) gives

$$\beta = \frac{|\mathbf{M}|^2}{r^3}(1 - 3 \cos^2 \theta) \quad (2.15)$$

where θ is the angle between the direction of the moments and \mathbf{r} . The dimer is called *H-aggregate* if the molecular transition dipoles are parallel and $\theta > 54.74^\circ$. For $\theta = 54.74^\circ$ the dipol-dipol interaction vanishes and for smaller angles the dimer is called *J-aggregate*. For the special case of an H-aggregate, only transitions to the higher energetic excited state are allowed, whereas in a J-aggregate only transitions to the lower energetic state are allowed. A more general discussion of selection rules is given in [19, 20].

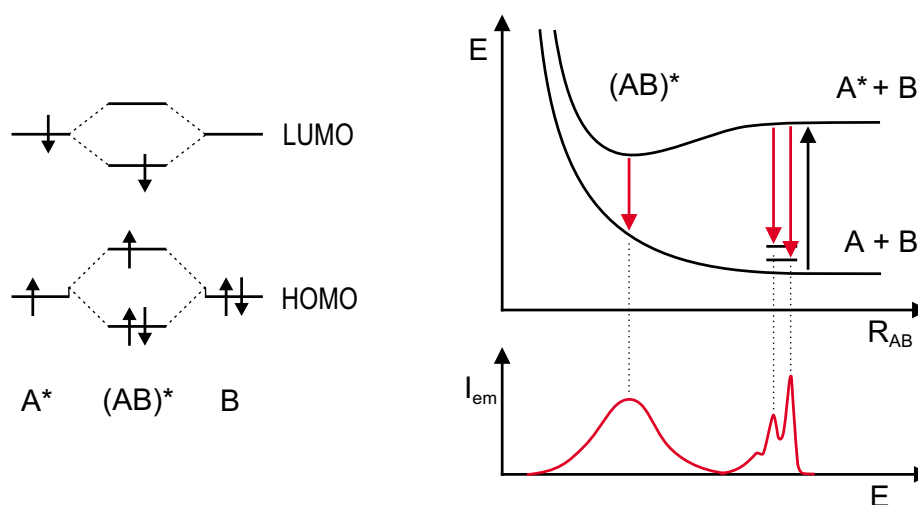


Figure 2.6: Left: Scheme of the molecular and excimer energetic levels. Right: Schematic representation of the potential energy surfaces as a function of the molecular separation R_{AB} for excimer formation. Additionally shown is the difference between monomer and excimer fluorescence (adapted from [18]).

2.2.1 Excimers

In the case of a physical dimer described above, the molecules are fixed with respect to each other, and a definite absorption and fluorescence band can be attributed to the dimer association.

Frequently it is observed that an increase in the concentration of molecules in solution is accompanied by a decrease in the quantum yield of fluorescence, a so-called self-quenching [21]. The solution exhibits the optical absorption characteristics of a monomer but also reveals a broad, structureless fluorescence spectrum with a particularly large STOKES shift. *Excimers* refer to dimers that only exist in the excited state, the ground-state of the pair is dissociative.¹

For the system $A + B$ of two molecules, the ground state of the pair is supposed to be dissociative. Thus, even if the molecules are free to move they do not form a physical dimer. Stabilizing interactions are possible if one of the molecules is in an excited-state and the HOMO and LUMO of the combined system are only singly occupied. This gives rise to the relative minimum of the excited dimer on the excited-state potential energy surface. The potential surfaces of the ground-state $A + B$ and the excited-state $A^* + B$ are represented schematically in Fig. 2.6. The excimer gains energy by reducing the molecular separation to the equilibrium distance. From this diagram, it is evident that excimer fluorescence is to be expected at longer wavelengths than monomer fluorescence and that the associated emission band should be broad and generally without vibrational structure, being due to a transition into the unbound ground state.

¹The name excimer was initially introduced in the 1960s. The definition holds for inorganic systems like $Hg^* + Hg \rightleftharpoons Hg_2^*$. Already the most prominent organic excimer, pyrene, forms a dimer-like crystal, showing that the ground state of the molecule is not purely repulsive. Therefore, there is no strict difference between dimers and excimers.

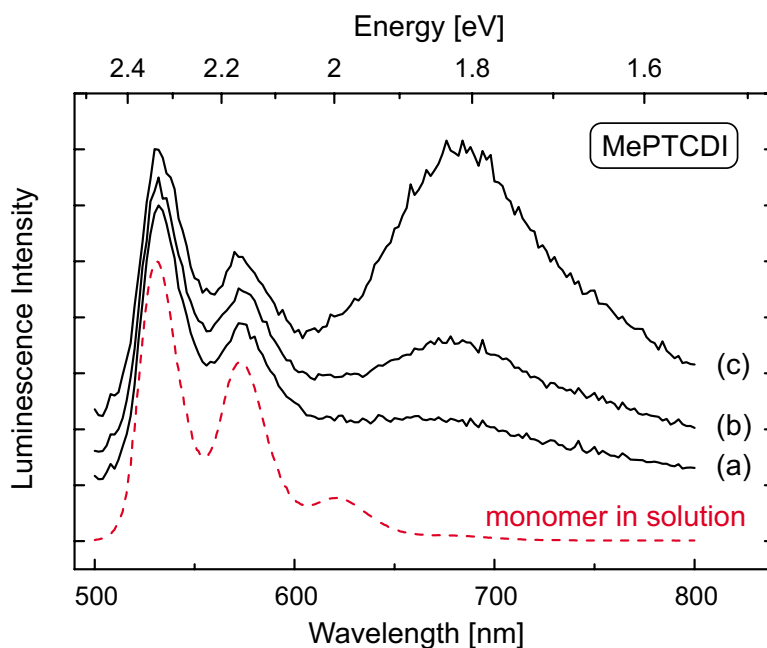


Figure 2.7: Stationary luminescence spectra of MePTCDI ultrathin films at 150K: (a) 20 molecules/100nm² corresponding to a half-monolayer, (b) 70 molecules/100nm², (c) 230 molecules/100nm². Absorption spectrum of dilute solution is shown as dashed line for comparison. Spectra are shifted and normalized with respect to the dominant monomer peak (adapted from [24]).

By definition, an excimer only exists in the excited state. However, excimer fluorescence also appears in crystals. It is therefore not necessary to insist on a purely repulsive ground state to understand the behavior described above. Notable and extensively studied examples are pyrene and α -perylene. In these crystals, the role of the "crystallographic molecule" is played by dimers. The unit cell of the crystal consists of two dimers. For α -perylene, the adjacent parallel molecules are closely spaced, the plane-to-plane separation being 3.47Å, which lies within the range of an attractive excimer interaction. When the crystal is excited, the excimer is thus easily formed by a contraction of the dimer of 0.3 – 0.4Å [22, 23]. Thus, the crystal fluorescence is that of the excimer in solution. For MePTCDI and perylene in the β -form, there are only two molecules per unit cell, dimers are not present. Nevertheless, excimer-like fluorescence was also observed for MePTCDI [24]. Layers with a nominal thickness much less than a monolayer show monomer-like emission similar to that of dilute solutions as shown in Fig. 2.7. With increasing molecular concentration on the surface the monomer emission decreases while the excimer-like emission appears and increases. Excimer-like emission in the condensed phase is closely connected to *exciton self-trapping* and will be discussed more detailed in Sec. 2.5.

2.3 Crystal Excitons

Since the interactions between the molecules in the crystal are much weaker than the intramolecular (covalent) interactions, the low-energy electronic structure of the isolated

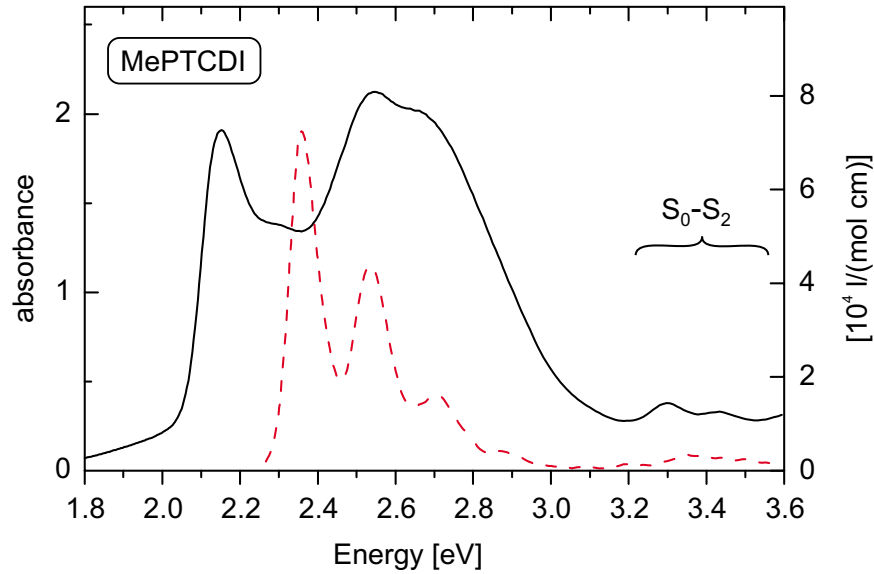


Figure 2.8: Comparison of crystal (solid) and monomer (dashed) absorption spectra for MePTCDI. Measurements were performed at room temperature.

molecules is not completely destroyed in the crystal but only modified. Therefore, on a coarse scale (0.5eV), the UV-VIS absorption spectrum of a crystal is related to the spectra of the isolated molecules described in Sec. 2.1. A direct comparison of the spectra is shown for MePTCDI in Fig. 2.8. For crystalline MePTCDI, the strong absorption bands between 2 and 3eV correspond roughly to the electronic transition of the monomer at 2.36eV. However, on the scale of vibrational excitations (0.17eV), the crystal spectrum deviates dramatically from the monomeric spectrum due to the intermolecular interactions of the same energetic magnitude.

A band-structure model, which is able to explain the absorption features of the MePTCDI crystal will be introduced in Sec. 2.3.1. First, we introduce some general aspects for the description of OMCs.

Types of Excitons

It is well known that neutral electronic excitations, known as *excitons*, play a fundamental role in the determination of optical properties of dielectric solids. This type of excitation corresponds to a bound state of an electron and a hole. It can be created by light or can appear as a result of relaxation processes of high-energy excited states, e.g., states of free electrons and holes generated by electric pumping. The first theories of excitons were already formulated in the 1930s by FRENKEL, PEIERLS and WANNIER and aimed at a description of UV-VIS light absorption and related phenomena in non-metallic solids [25]. Three models are usually employed to classify excitons - the small radius FRENKEL exciton model, the large radius WANNIER-MOTT exciton model and, as intermediate stage, the charge-transfer exciton model.

The states of WANNIER-MOTT excitons appear due to COULOMB attraction between free electron and hole and is based on the effective mass approximation for

quasi-particles in the periodic crystal potential. Therefore the internal structure of WANNIER-MOTT excitons can be represented by hydrogen-like functions. The radius of the exciton may be defined as the average separation of the electron from its corresponding hole. The electron-hole distance for this type of excitons should be larger than the lattice constant: sometimes it is more than an order of magnitude larger (40 – 100Å). This condition can only be fulfilled, if static dielectric constant is large enough and at least one of the charge carriers has sufficiently small effective mass, i.e., if its bandwidth is large compared to the COULOMB attraction between electron and hole in the exciton. Such a situation is typical for inorganic semiconductors (Si, Ge, GaAs etc.) due to the large overlap of the atomic orbitals and the high static dielectric constants.

On the other hand, the FRENKEL exciton (FE) model considers an excited state in which the electron and hole are placed on the same molecule. Intermolecular interactions give rise to a finite hopping integral for the transfer of the electronic excitation from one molecule to another. As a result, in ideal crystals the FRENKEL excitons, just like the WANNIER-MOTT excitons, are represented by one-particle excitation waves coherently propagating through the crystal. The FE model is applicable if the binding energy (i.e. the energy difference between a crystal with a free electron and hole with respect to the crystal with a FE) is large compared to both free carrier bandwidths. Then, the deviation from electroneutrality of the molecules in the lowest energy excitations is negligible small.

However, the consideration of the electrical properties of organic molecular crystals often requires extension of the simple FE theory to include excited ionized states (charge-transfer states) in which an electron has been removed from one molecule and placed on a nearby molecule of the crystal [26]. Thus, the *charge-transfer exciton* (CTE) occupies an intermediate place in the classification of excitons based on their internal structure. MERRIFIELD [27] considered CTEs with arbitrary electron-hole separation n , which is given in units of the molecular separation ($n \geq 1$). The WANNIER-MOTT exciton corresponds in this description to the case of $n \rightarrow \infty$.

The localization of a pair of charge carriers at different molecules is supported in organic crystals, because, in contrast to semiconductors the binding energy of the lowest CTE is usually large compared to the valence and conduction bandwidth. The localization can also be stabilized due to a strong tendency of CTE to undergo self-trapping [28], which will be explained in Sec. 2.5.

The 1D Crystal

The extension of the description of excited states of a dimer given in Sec. 2.2 to an array of identical molecules introduces no formal difficulties. For moderate distances of the molecules within the crystal (assuming weak interaction of neighboring molecules), the description using only FRENKEL type excitons shall be sufficient. The first application of this concept to organic crystals was given by DAVYDOV in 1948 [29].

A description for the most simple model, a linear chain composed of identical molecules, is given in standard text books [30]. Like in the dimer case, the interaction part of the HAMILTONIAN, which describes now a transfer probability of FRENKEL exciton from one to a neighboring molecule, will lead to the modification of the excited states:

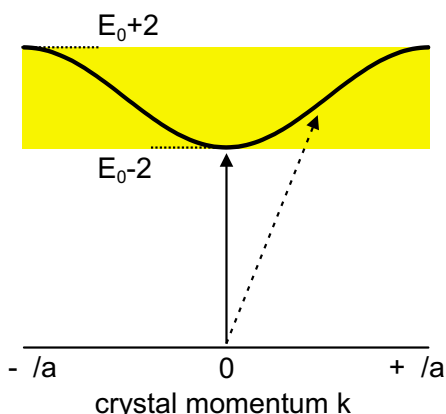


Figure 2.9: Energy band of a linear crystal with nearest-neighbor interactions. Absorption can only occur as a vertical transition at $k \approx 0$ (solid arrow). The transition represented by the dashed arrow is forbidden in first order and only occurs with the inclusion of phonon interactions.

In the case of dimers, the degeneracy of the monomer levels is broken and two levels of different energy are formed. In the case of an ideal chain of N molecules without exciton-phonon interaction the energy of exciton states in approximation of nearest neighbor interaction is equal to

$$E_j = E_0 + 2\beta \cos\left(\frac{\pi j}{N+1}\right) \quad (2.16)$$

where β is the matrix element of transferring the excitation to the neighboring site (which can be either positive or negative), $j = 1, \dots, N$ numbers the states and E_0 is the energy of molecular excitation including the gas-condensed matter shift. We have neglected here the variation of this quantity at the ends of the chain. The states form an exciton band of levels; each of the excitonic states is distributed over the whole length of chain and we can call them "bulk" states. The excitation energy will in time be shared with all the molecules in the chain. For $N \gg 1$ and $k := (\pi j)/L$, where L denotes to the length of the chain, we have

$$E_k \cong E_0 + 2\beta \cos(ka) \quad (2.17)$$

where a is the 1D lattice constant. It can be shown [31] that only eigenstates with odd j have nonzero oscillator strength and that state $j = 1$ (i.e. $k \approx 0$) contains an overwhelming part of the total oscillator strength: up to 81% for $N \gg 1$. The oscillator strength of higher states drops as $1/j^2$ for $j \ll N$. In real systems, the exciton-phonon interaction leads to widening of lines corresponding to states with different j . However, the model presented here is only valid if the exciton-phonon coupling is weak and self-trapping is absent. An introduction of a more realistic model, including not only FRENKEL but also CT excitons, will be given in the following section.

2.3.1 Excitons in the Quasi-1D Crystal of MePTCDI

In this section, we want to describe a band structure model for quasi-one-dimensional crystals with strong orbital overlap between neighboring molecules developed by HOFFMANN et al. [32]. In such crystals, the energy difference between lowest FRENKEL exciton and the lowest charge-transfer excitons becomes small. Therefore a one-dimensional model including FRENKEL and nearest-neighbor CT excitons will be introduced.

The distance between the molecular planes within the one-dimensional stacks of MePTCDI is 3.40\AA , which is small in comparison to other lattice constants and also small in comparison to the size of the molecules. This causes strong interactions of the π -electron system within the stacks, but a very weak interaction in the other directions. Due to these strong interactions in the stack the qualitative difference between FRENKEL and CT excitations becomes small. The energies of FRENKEL and CT excitons approach each other and a strong mixing determines the nature of lowest energy states. The first model for the mixing of FRENKEL and CT excitons was presented by MERRIFIELD [27].

The absorption spectrum of MePTCDI crystals is roughly described by four peaks in the range of $S_0 - S_1$ transition (see Fig. 2.8). Since the lowest energy monomer absorption is dominated by only three peaks, it can be well described by the lowest energy electronic transition with three molecular vibronic levels. These three molecular levels plus consideration of nearest-neighbor CT states become four optically active mixed exciton bands if we take into account the mixing of molecular configurations arising due to intermolecular resonance interaction. The corresponding 1D HAMILTONIAN is given by:

$$\begin{aligned}
 H &= H^F + H^{FF} + H^C + H^{FC} & (2.18) \\
 H^F &= \sum_{n\nu} \Delta_F^\nu B_{n\nu}^\dagger B_{n\nu} \\
 H^{FF} &= \sum_{\substack{n\nu \\ m\mu}} M_{nm}^{\nu\mu} B_{n\nu}^\dagger B_{m\mu} \\
 H^C &= \sum_{n\sigma} \Delta_{CT} C_{n\sigma}^\dagger C_{n\sigma} \\
 H^{FC} &= \sum_{n\nu} \{ \epsilon_e^\nu (B_{n\nu}^\dagger C_{n,+1} + B_{n\nu}^\dagger C_{n,-1}) + \epsilon_h^\nu (B_{n\nu}^\dagger C_{n+1,-1} + B_{n\nu}^\dagger C_{n-1,+1}) + \text{h.c.} \}
 \end{aligned}$$

Here, the operator $B_{n\nu}^\dagger$ ($B_{n\nu}$) describes the creation (annihilation) of a neutral molecular excitation (FRENKEL exciton) at lattice site n . Only the lowest electronically excited molecular state is considered, and the index $\nu = 0, 1, 2$ specifies the three excited vibrational levels. Then Δ_F^ν is the FE on-site energy and $M_{nm}^{\nu\mu}$ the hopping integral for excitation transfer from level ν at site n to level μ at site m . The terms for $n = m$ are omitted in the summation in H^{FF} . The HAMILTONIAN $H^F + H^{FF}$ can be used to describe the well-studied case of mixing of molecular configurations for FE with several excited states in HEITLER-LONDON approximation.

In addition to these FRENKEL excitons, nearest neighbor charge transfer excitons are included. A localized CT exciton with the hole at lattice site n and the electron at lattice site $n + \sigma$ ($\sigma = -1, +1$) is created (annihilated) by the operator $C_{n\sigma}^\dagger$ ($C_{n\sigma}$). Only the vibrational ground state is considered for the CT excitons with Δ_{CT} as their on-site energy. Hopping of CT states will not be considered.

The mixing between FRENKEL and CT excitons is expressed in H^{FC} . Here, the transformation of a CT state into any FRENKEL state at the lattice site of either hole or electron is allowed. The relevant transfer integrals ϵ_e^ν (ϵ_h^ν) can be visualized as

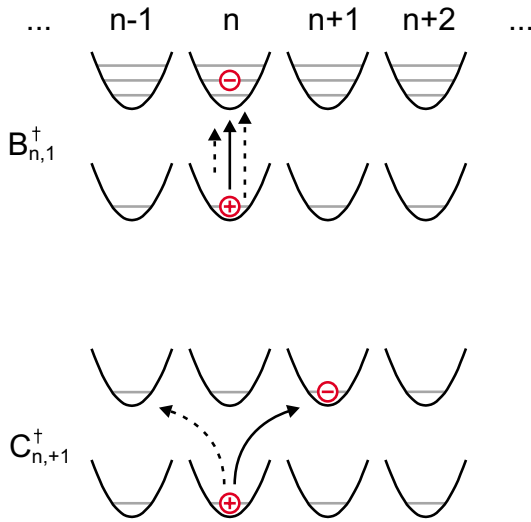


Figure 2.10: Scheme of basis states from the model HAMILTONIAN (2.18). The upper scheme depicts one of three FRENKEL excitations considered, whereas the lower scheme depicts one of two charge-transfer excitations considered.

transfer of an electron (hole) from the excited molecule n to its nearest neighbor.

In the following, we outline the main steps described in detail in [32]. Transforming all operators into momentum space representation results in a HAMILTONIAN that is already diagonal with respect to k , but still contains mixed terms of the three operators for the FRENKEL excitons and the two operators for CT excitons. These are altogether five molecular configurations, which would yield five mixed exciton bands. Then, only nearest neighbor FE transfer are considered, keeping M as the electronic part of the FE hopping integral. In addition, coupling of CT excitons to the considered vibrations is neglected, the remaining electronic part of the transfer integral ϵ_e' (ϵ_h') is ϵ_e (ϵ_h). Using adapted operators with even and odd symmetry with respect to the direction of the charge transfer, one finds that the odd operator does not mix anymore, reducing the number of mixed bands by one. The remaining HAMILTONIAN can be diagonalized numerically.

With the knowledge of the excited states, it is possible to calculate the total transition dipole moment \vec{P} for optical excitation into the $k = 0$ state of each band. The transition dipole can be written as a sum of a FRENKEL and a CT transition dipole $\vec{P} = \vec{P}_{\text{FE}} + \vec{P}_{\text{CT}}$. If intermolecular exchange effects are neglected, these can be related to molecular transition dipoles by $\vec{P}_{\text{FE}} = a_{\text{FE}} \vec{p}_{\text{FE}}$ and $\vec{P}_{\text{CT}} = a_{\text{CT}} \vec{p}_{\text{CT}}$. Here, \vec{p}_{FE} and \vec{p}_{CT} are the transition dipole moment of the molecular FE and of the even CT state of the crystal dimer. The contribution of the FRENKEL exciton states (CT state) to state $k=0$ of each band is considered by the prefactor a_{FE} (a_{CT}). This composition, especially the CT parentage, varies for the different bands. Even if the CT transition dipole is vanishingly small, the oscillator strength of the FRENKEL exciton is distributed over all mixed exciton bands. This is expressed by the notion that the CT exciton "borrows" oscillator strength from the FRENKEL states. In addition, it follows from quantum chemical calculations that \vec{p}_{CT} has a large component within the molecular plane. This component is not parallel, but forms an angle of about 68° with \vec{p}_{FE} . Therefore, the direction of the total transition dipoles \vec{P} will vary from band to band.

Absorption measurements of highly oriented MePTCDI films for perpendicular incidence and two orthogonal polarization directions at 5K were performed to apply the model and adjust the parameters. One finds that the peak positions are slightly dif-

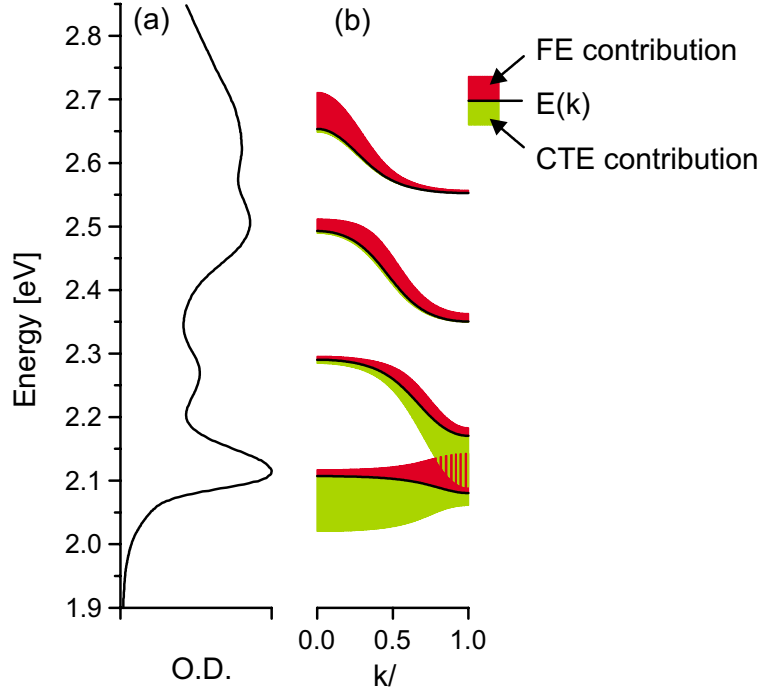


Figure 2.11: One dimensional exciton band structure in MePTCDI. (a) Absorbance of thin film at 5K. (b) Dispersion of the mixed exciton bands $E(k)$ (solid lines). The upper, dark shaded stripes show the contribution of FRENKEL exciton states. The lower, light shaded stripes show the contribution of the charge transfer exciton (adapted from [32]).

ferent for both polarization directions. These peak shifts are a DAVYDOV splitting due to the two molecules in the MePTCDI unit cell. From the occurrence of DAVYDOV splitting, it follows that the exciton states of the two non-equivalent stacks are coherently coupled. Finally, one extracts the following values from polarized absorption spectra: $\Delta_F^0 = 2.23\text{eV}$, $\Delta_{CT} = 2.17\text{eV}$, $M = 0.10\text{eV}$, $\epsilon_+ = 0.10\text{eV}$ and $p_{CT}^{\text{rel}} = 0.31$. As the extraction of the given values is based on the specific model assumptions, the physical accuracy of the values might be smaller than the two decimal places suggest. Quantum chemistry also provides the parameter $|\epsilon_e - \epsilon_h| = 0.05\text{eV}$, which is not accessible from absorption experiments. With this parameter, the full momentum dependent band structure for the excitons can be calculated. The result is shown in Fig. 2.11. There, the composition of the bands is also indicated by a schematic visualization of the k -dependent values $|\vec{P}_{FE}^\beta|^2$ and $|\vec{P}_{CT}^\beta|^2$.

In summary, there are two main features of the model HAMILTONIAN (2.18): (i) if the FE-CT coupling is on the same order as the energetic separation between the CT and the FRENKEL excitons, the model predicts a strong mixing resulting in four significantly absorbing bands. (ii) With a finite CT transition dipole, the polarization direction of the bands will vary due to the varying composition of the bands. The model HAMILTONIAN presented is capable to describe energetic positions, peak intensities and a varying polarization ratio for absorption spectra of MePTCDI and other quasi-one-dimensional crystalline perylene-derivatives. The exciton structure is essentially determined by a strong mixing of FRENKEL and CT excitations. This is up to now the only model introducing a mechanism that leads to polarization dependent spectra

due to the contribution of a CT transition dipole. Very recently, HOFFMANN presented an extension of the 1D model, including not only exciton-phonon configurations at the same molecular site but also displaced exciton-phonon configurations [33].

We also want to mention a distinctive different exciton band-structure model developed by VRAGOVIĆ et al. [34]. It is also based on Frenkel excitons coupled to an single effective intramolecular-vibrational mode, while neglecting any CT contribution. In contrast to the 1D model presented above, it includes the full 3D-crystal geometry with two molecules in the unit cell. It shows also nice agreement to unpolarized absorption spectra, while it is not able to explain any anisotropy for polarized absorption spectra.

2.4 Dynamic (Vibrational) Properties

Molecular crystals show two kinds of vibrations. First, there are intramolecular, i.e. the "normal" vibrational modes of molecules dominating at high frequencies. Second, we find intermolecular modes (predominantly at low frequencies) connected to the lattice vibrational modes, i.e., to lattice acoustic and optical phonons. Since the dynamic processes play a very important role in interaction phenomena of charge carriers and excitons in OMC, they shall be briefly introduced in an exemplary fashion on MePTCDI. An important example of intermolecular dynamic processes, the formation of excimers, was already introduced in Sec. 2.2.1.

The isolated MePTCDI molecule belongs to symmetry group C_{2h} or C_{2v} depending on the orientation of the methyl groups. Therefore, the molecules possesses $3N - 6$ normal vibrational modes, where N is the number of atoms in the molecule (linear molecules have $3N - 5$ normal vibrations). Hence, for MePTCDI ($C_{26}N_2O_4H_{14}$) we have $3 \times 46 - 6 = 132$ vibrational modes. 66 of them, with odd parity $P = -1$, are RAMAN active. Only the totally symmetric A_g breathing modes are active in resonant-RAMAN spectroscopy, which are 23 in our case. For aromatic molecules, like perylene-derivatives, intramolecular modes predominantly cover the energy range from ~ 100 to some 1000cm^{-1} . For instance, the effective vibrational mode of MePTCDI, which dominates the monomer absorption spectrum has an energy of $\hbar\omega = 0.17\text{eV} = 1370\text{cm}^{-1}$ (see Sec. 2.1.1). However, there are also intramolecular vibrational modes of lower symmetry (B_g) at energies below 100cm^{-1} , as observed in our time-resolved experiments on MePTCDI (see Sec. 4.3).

MePTCDI forms a crystal of monoclinic centrosymmetric symmetry group $P2_1/c$ with two molecules per unit cell. It has therefore 12 (external) phonon branches: three translational acoustic (TA), three translational optic (TO), and six rotational optic phonons (librational optic - LO). The translational optic phonons are infrared active only, whereas the librational modes with even parity (three A_g and three B_g modes in terms of representations of the group $P2_1/c$) are RAMAN active. In general, librations should show strong RAMAN activity if the difference between the polarizability values of the molecules perpendicular to the axis of libration is large. A comprehensive study of the lattice vibrational modes of α - and β -perylene is given by KOSIC, SCHLOSSER and DLOTT [35]. The energies found for β -perylene, as a similar system to MePTCDI, cover the energy range from ~ 40 to 150cm^{-1} . Due to crystallization, the symmetry of the single molecules is also lowered to point group C_i , which contains unity (E) and

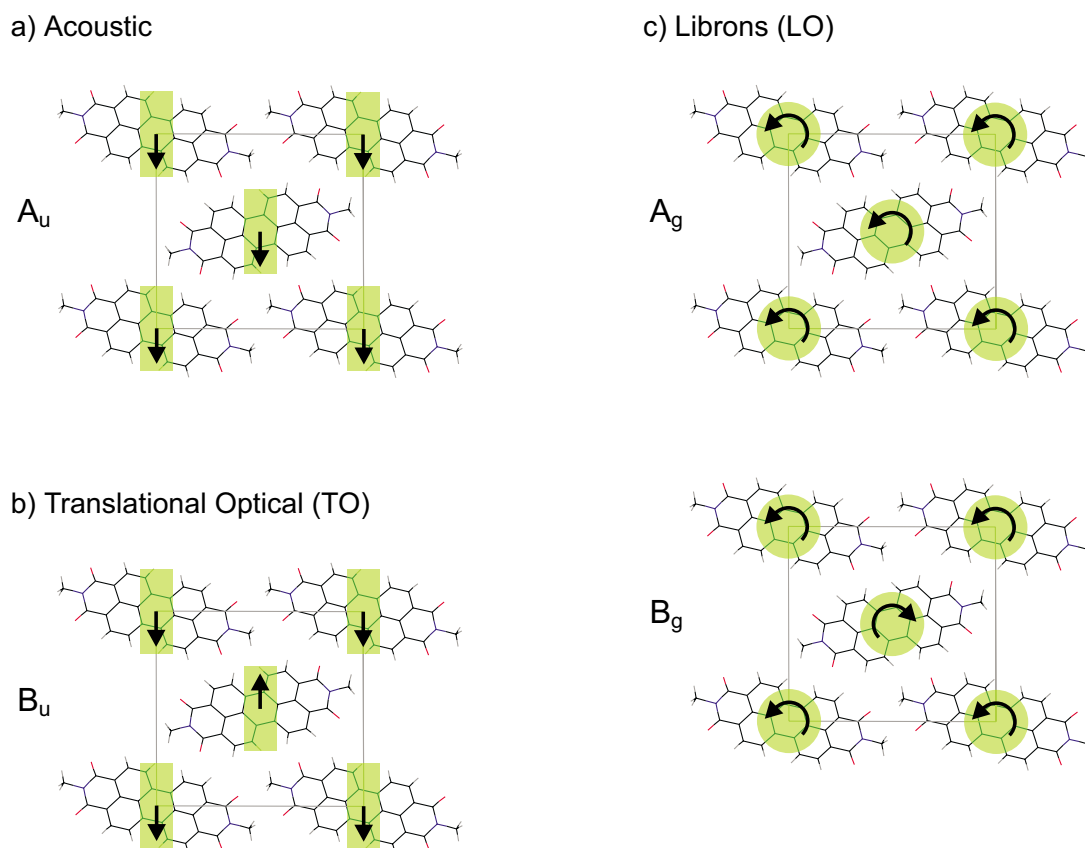


Figure 2.12: Schematic illustration of lattice vibrational modes of MePTCDI. There are 12 phonon branches, 3 acoustic (a), 3 infrared active translational optic phonons (b), and 6 RAMAN active librons (c).

inversion (i) as the symmetry operations to project each molecule on itself.

There is another possible dynamic process: *exciton self-trapping*. In contrast to the vibrational eigenmodes of an OMC discussed so far, this process requires an electronic transition. We have already introduced this process for pairs of molecules, so-called excimers (see Sec. 2.2.1). The concept can be extended to crystals, as shown in the following.

2.5 Exciton Self-Trapping

Owing to the translational symmetry of the crystal lattice, the wave-function of the exciton spreads over the crystal. However, in a crystal in which excitons interact strongly with phonons, excitons are trapped by lattice distortions produced by excitons themselves. Those trapped excitons are called self-trapped excitons (STE), whereas excitons whose wave functions are spread over a crystal are called free excitons. STE are of fundamental importance for electronic processes of energy transport. They can not only be found in numerous OMC, but also in a wide variety of halide crystals, condensed rare gases, and quasi-1D materials. It is still a considerable challenge to theory to predict any instability of the electronic excited lattice, and to predict the corresponding

relaxed configurations. In the same way, it is experimentally challenging to adapt spectroscopy to dynamic processes occurring as fast as a few hundred femtoseconds. In the following, we want to introduce the *adiabatic* description of self-trapping. It results in a very interesting prediction for quasi-1D systems: There is a strong tendency for self-trapping!

A charged carrier in a deformable lattice creates an attractive potential well, either long-range or short-range, in which it is momentarily trapped. This is called a *polaron*. The time scale of such momentary trapping can vary within a wide range, depending on the strength and the type of carrier-lattice coupling. A (neutral) exciton also introduces a lattice polarization, but it ranges not as far as the COULOMB range of an electron, nor is it as strong. Under appropriate conditions, an exciton moving in an deformable lattice can become a stable or metastable self-trapped state. This is then called a *exciton polaron*. A simple model, that gives the criteria for self-trapping in the adiabatic approximation,² has been given by TOYOZAWA [36]. A short summary will be given here following [37, 38]. Self-trapping is a short-range exciton-phonon coupling caused mainly by *acoustic* phonon modes. It is described by an exciton-phonon coupling constant g which can be determined phenomenologically as the following ratio:

$$g = \frac{E_{\text{lr}}}{2\beta} \quad (2.19)$$

where E_{lr} is the lattice relaxation energy and term β represents the width of the exciton band. Equation (2.19) characterizes the relative energy gain for both stable exciton states. If $E_{\text{lr}} < 2\beta$, corresponding to $g < 1$, it is energetically more favorable for the exciton to exist in the form of a free exciton, and vice versa, if $g > 1$, the formation of a STE is probable. In the case of strong exciton-phonon coupling, a double minimum adiabatic potential is formed in which the free exciton is metastable and the ST exciton is the stable one (see Fig. 2.13). The criterion of instability for an exciton to undergo self-trapping is given by:

$$g > \frac{\pi^2 N^{[1-(2/d)]}}{2d} \quad (2.20)$$

N is the number of sites in a cube of dimension d . In the limit $N \rightarrow \infty$, this predicts that self-trapping of excitons always occurs in a one-dimensional systems for any finite exciton-phonon coupling strength g . For $d = 3$, the free exciton is predicted to be locally stable for any g ; i.e. there is always a barrier to self-trapping in 3 dimensions, as shown in Fig. 2.13. For $d = 2$, $g > \pi^2/4$ is needed for instability in this model.

The exciton self-trapping phenomena, particularly in the dimer-like crystals of pyrene and α -perylene, have been extensively studied: For pyrene, MATSUI et al. obtained a self-trap depth $E_{\text{lr}} - 2\beta = 660\text{cm}^{-1}$ and a barrier height of 260cm^{-1} by applying temperature dependent time-resolved luminescence [40]. Using the same technique, a similar barrier height of 310cm^{-1} was found for α -perylene [41], whereas the self-trap depth $E_{\text{lr}} - 2\beta = 2400\text{cm}^{-1}$ has been estimated to be much bigger [23]. Relaxation into the self-trapped state occurs with a self-trapping time $\tau_{\text{st}} \approx 140\text{fs}$, as obtained in

²Adiabatic means in that context that the electron charge adjusts to the new configuration of atoms instantaneously.

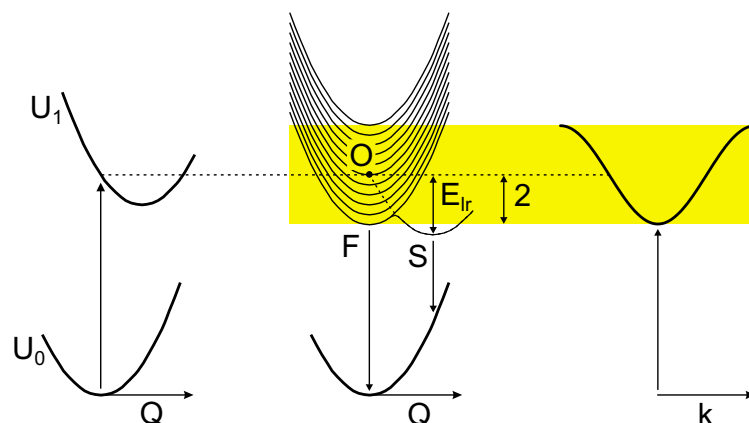


Figure 2.13: Configuration coordinate models for a single molecule (left), an exciton (middle) in a rigid lattice in adiabatic approximation (according to [39]). The according excitonic band (right) as a function of wave vector k has a band width of 4β . U_0 and U_1 are vibronic potentials as a function of configuration coordinate Q for ground and excited state, respectively. O denotes the energy of the lowest excited level of the free molecule. F and S denote, respectively, the bottom of the free-exciton band and the lowest-energy state of the self-trapped exciton. Between the free-exciton state and the self-trapped state is a potential barrier, which is called self-trapping barrier. E_{lr} represents the lattice relaxation energy.

transient absorption spectroscopy by WILLIAMS and NELSON [42]. Some more experimental results for the excimer crystal of α -perylene were already given in Sec. 2.2.1. Self-trapping dynamics were also investigated for some quasi-one-dimensional systems: For polydiacetylene, KOBAYASHI et al. measured ≈ 150 fs for the relaxation to a thermalized STE using transient absorption spectroscopy [43]. Using the same technique, DEXHEIMER et al. investigated a quasi-1D halogen-bridged platinum complex, obtaining similar values of about 200fs [44]. Using time-resolved luminescence up-conversion TOMIMOTO et al. could nicely observe the self-trapping in a similar halogen-bridged platinum complex [45, 46]. Self-trapping itself was estimated to occur within 140fs, whereas the STEs have a lifetime of about 5.5ps at room temperature.

2.6 Open Questions

In the present chapter, we have reviewed the theoretical description of electronic and phononic states of single molecules on the example of MePTCDI. The closely related properties of optical absorption and emission are well understood. Even though molecular crystals of MePTCDI and other perylene derivatives have been investigated for more than ten years, the knowledge about crystal absorption, relaxation and recombination processes is still limited. The attempts to explain the absorption properties got the most advanced stage. The exciton-band model by HOFFMANN et al., introduced in Sec. 2.3.1, is able to explain the puzzling polarized absorption spectra. The strong electron-phonon coupling of those small molecules and the role of charge-transfer excitons seems to be crucial for the free exciton states of the crystal. However, the accuracy of the model concerning the derived parameters is limited. There are also distinctively different approaches to explain the optical spectra and the discussion about this topic

is still lively [34, 47]. In contrast to that, the ultrafast relaxation of the electronic excited states is still unclear and was not investigated so far. Also the photoluminescent properties are not yet understood. Low-temperature photoluminescence (PL) spectra have been investigated for MePTCDI and PTCDA [48, 49, 50, 51]. The results are puzzling and the interpretations differ considerably. The nature of the emitting states is unknown.

There are several possible pathways of relaxation after an optical transition: First, the free excitons at $k = 0$ might relax down to the bottom of its band at $k = \pi$ (*intra*band relaxation), and, if a higher band was excited, from there to the lowest exciton band at $k = \pi$ (*inter*band relaxation). It might be also vice versa, first *inter*band relaxation to the lowest band at $k = 0$ and subsequent *intra*band relaxation to $k = \pi$. In both cases, the steady-state luminescence will stem from free-exciton states of the lowest band edge at $k = \pi$. A completely different scenario includes ultrafast localization of the free-excitons due to self-trapping. The band-like character of the states will vanish due to the deformation of the crystal lattice around the exciton. Luminescence stems from self-trapped states, which differ considerably from the free exciton band states of the rigid lattice. The first main questions of this thesis are the following:

- On which time-scale are optically excited states depopulated (away from $k = 0$)?
- How long does it take to complete excited-state relaxation? To say it in other words, how long does it take to populate the luminescent states?
- What is the nature of the emitting states? (free-exciton band states, self-trapped states, or even defect trapped states)

The concept of a band-like description of excitons in MePTCDI is only sensible, if the inhomogeneous broadening of the participating states is smaller than the predicted bandwidth. Therefore, it is a very useful information to which extent the linewidth of an optical transition is determined by homogeneous and inhomogeneous broadening. Experimental techniques, like DFWM are able to discriminate between the two broadening mechanisms. Concerning the dephasing of electronic coherence, which determines the homogeneous linewidth, there only a few results on organic solids. The interpretation of the results is inconsistent so far. The question remains:

- Are the optical transitions dominated by homogeneous or inhomogeneous broadening?

As we have stressed already, the strong exciton-phonon coupling determines the optical properties of the single molecule of MePTCDI. Exciton-phonon interaction seems to be also very important for the crystal, however, it is much less understood. Especially the possibility of a quasi 1D crystal to undergo self-trapping requires a detailed investigation of its dynamic properties. This topic can be focused to the rather general question:

- What can we learn about the phononic properties of a quasi-1D crystal of small molecules?

3 Techniques of Time-Resolved Spectroscopy

Time-resolved experiments in the pico- and femtosecond time range require ultrashort laser pulses of the same time range. At the beginning of this chapter, we shortly review properties of ultrashort laser pulses, their generation, control, and propagation in dispersive media. Therefore, some useful concepts of non-linear optics are given. In the second part, we introduce the used experimental techniques of ultrafast spectroscopy.

3.1 Generation and Control of Ultrashort Light Pulses

Phononic relaxation in solids happens on a picosecond timescale, electronic even on a femtosecond timescale. It is elucidating to visualize this order of magnitude. The speed of light in vacuum is about 300000kms^{-1} . This implies that a light pulse circles the Earth about 7.5 times each second. In one nanosecond, the same light pulse traverses only 30cm. Currently the shortest pulses in the visible are less than 5fs, e.g. [52], what already requires a spectral width of nearly 100nm. The fs laser pulses we are working with are of about 20fs, what corresponds to a pulse length of about $6\mu\text{m}$. This represents the positional accuracy of optical elements that is required in a so-called pump-probe experiment. A pump laser pulse drives the system investigated out of its thermodynamical equilibrium. A second, time-delayed probe pulse subsequently monitors the decay of this excited state. The whole process is repeated stroboscopically many times.

Ultrashort pulses are generated by mode-locked lasers. By constructive interference, a short pulse is formed when many longitudinal modes are held in phase in a laser resonator. With the invention of mode-locked lasers in the mid-1960s, the picosecond timescale became accessible, but many measured rate constants, e.g. such as energy redistribution in molecules, electron transfer reactions, photoisomerization and dissociation, and relaxation in semiconductors were found to be instrument limited. However, ultrafast spectroscopy was revolutionized in the 1980s by the invention of the "CPM", the colliding-pulse mode-locked dye laser, and again in the early nineties by the invention of the self mode-locking in titanium-sapphire lasers (Ti:Sapphire). Its simplicity of use led to the commercialization of ultrashort pulse technology.

3.1.1 Linear Pulse Propagation

Laser pulses are formed by the superposition of many longitudinal modes of different frequencies. Essential condition for getting short pulses is that the phases have to be

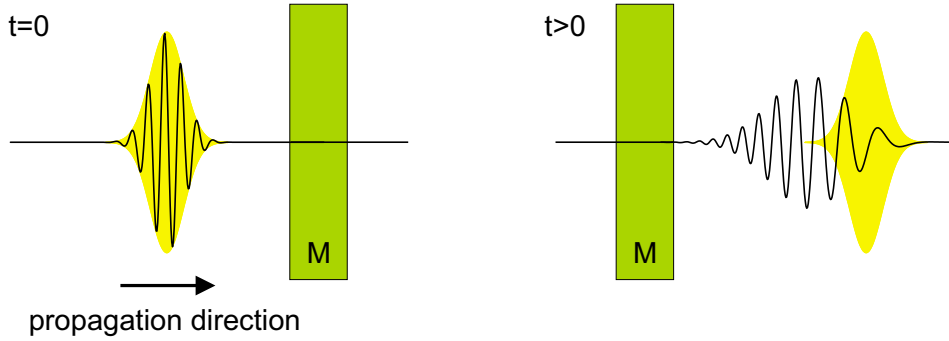


Figure 3.1: Schematic diagram of the electric field of an undispersed GAUSSIAN pulse (left) and the same pulse after traveling through a positively-dispersing medium M (right). The pulse is delayed with respect to a reference pulse in vacuum and a frequency sweep from low to high frequency (right to left) can be observed.

fixed with respect to each other in a certain way. Shortest pulses are achieved, if all contributing waves have the same phase.¹ These are then called *bandwidth-limited* pulses. For a given spectral profile, the shortest pulse is given simply by its FOURIER transform. The *bandwidth product* of a pulse of a full width at half maximum (FWHM) τ_p and a spectral bandwidth $\Delta\nu_p$ is given by

$$\tau_p \cdot \Delta\nu_p \geq K \quad (3.1)$$

where the dimensionless parameter K solely depends on the spectral shape of the envelope. Equality to K is reached for the bandwidth-limited case. Table 3.1 gives values of K for the cases of GAUSSIAN and Hyperbolic secant shape, which are relevant for ultrashort pulses.

A bandwidth-limited 20fs (FWHM) GAUSSIAN pulse, centered at 600nm, has a bandwidth of 28nm. Taking into account the wings of the spectrum, this pulse actually covers nearly 100nm. When this pulse travels through a dispersive medium, the frequency components are separated in time. Figure 3.1 shows the effect of dispersion on a GAUSSIAN pulse traveling through a piece of glass. There are two points to notice. First, the center of the pulse is delayed with respect to a pulse traveling in vacuum. This is usually called the group delay, which is not a broadening effect. Sec-

¹A linear frequency dependence of the phase $\varphi(\omega)$ will also result in shortest pulses, yielding an additional delay of the pulse (see (3.2)).

Table 3.1: Values of K for pulses with GAUSSIAN and Hyperbolic secant envelope, in the inequality $\tau_p \cdot \Delta\nu_p \geq K$, when $\Delta\nu_p$ and τ_p are FWHM values.

Shape	$E(t)$	K
GAUSSIAN	$\exp(-(4 \ln 2)t^2/\tau_p^2)$	0.441
Hyperbolic secant	$\text{sech}^2(1.76t/\tau_p)$	0.315

ond, normally-dispersive media like glass impose a positive frequency sweep or "chirp" on the pulse, meaning that the blue components are delayed with respect to the red. Thus, the 20fs pulse (at 600nm) will be stretched by a 4mm piece of glass (BK7) to 45fs.

The propagation of an optical pulse is commonly described in frequency domain [53, 54]. By propagating inside a medium, each spectral component of the original pulse experiences a phase shift φ . The spectral phase $\varphi(\omega)$ can be developed into a power series around the central frequency ω_0 , assuming the phase varies only slowly with frequency as

$$\varphi(\omega) = \underbrace{\varphi(\omega_0)}_{\varphi'(\omega_0)} + \underbrace{\frac{\partial\varphi}{\partial\omega}\bigg|_{\omega_0}}_{\varphi''(\omega_0)} (\omega - \omega_0) + \frac{1}{2} \underbrace{\frac{\partial^2\varphi}{\partial\omega^2}\bigg|_{\omega_0}}_{\varphi''(\omega_0)} (\omega - \omega_0)^2 + \frac{1}{6} \underbrace{\frac{\partial^3\varphi}{\partial\omega^3}\bigg|_{\omega_0}}_{\varphi'''(\omega_0)} (\omega - \omega_0)^3 + \dots \quad (3.2)$$

The term φ is a trivial phase term, and $\varphi'(\omega_0)$ is the *group delay*. Both they do not affect the pulse shape, whereas all higher order terms cause temporal broadening. The quadratic term $\varphi''(\omega_0)$ is the *group-velocity dispersion* (GVD), and $\varphi'''(\omega_0)$ is simply the third-order dispersion (TOD). Now, we consider a transform-limited GAUSSIAN pulse with a central frequency ω_0 and a pulse width (FWHM) τ_{in} . Then, its electric field E_{in} takes the form

$$E_{in}(t) = \text{Re} \left(E_0 \cdot e^{-(2 \ln 2)t^2/\tau_{in}^2 + i\omega_0 t} \right) \quad (3.3)$$

The electric field, after traveling a distance l through a dispersive, non-absorbing medium, can be found by transforming E_{in} to the frequency domain and adding the components from the phase expansion $\varphi(\omega)$ in (3.2) and transforming it back to time domain. For the sake of simplicity, we truncate the phase expansion after the GVD term, neglecting phase terms of higher order. The resulting expression is given by:

$$E_{out}(t) = \text{Re} \left(\frac{E_0}{\sqrt{1 + i\varphi''/\tau_{in}}} \cdot e^{-\Gamma[t-\varphi']^2 + i(\omega_0 t - \varphi)} \right) \quad (3.4)$$

where

$$\Gamma = \left(\frac{\tau_{in}^2}{2 \ln 2} + 2i\varphi'' \right)^{-1} \quad (3.5)$$

By inspecting the GAUSSIAN part of E_{out} , one realizes that the pulse is delayed by the amount of φ' with respect to a pulse traveling in vacuum. The effects of pulse dispersion are two-fold. First, the pulse width τ_{out} of E_{out} is increased with respect to the input-pulse width:

$$\tau_{out} = \tau_{in} \sqrt{1 + \left(\frac{4 \ln 2 \cdot \varphi''}{\tau_{in}^2} \right)^2} \quad (3.6)$$

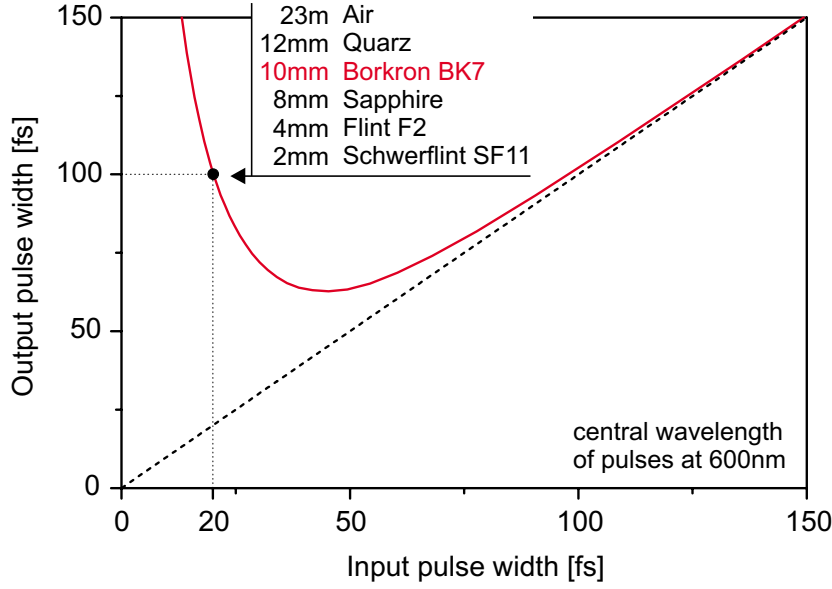


Figure 3.2: GAUSSIAN pulse width before and after 10mm of Borkron glass BK7 (solid line) for pulses centered at 600nm. The input pulses are band width limited. The broadening is due to group-velocity dispersion. A comparable broadening of a 20fs pulse by a factor of five will be achieved by materials of the given thickness.

Second, a frequency sweep is introduced in the output pulse (because the expression in (3.5) is complex) with a sign that is opposite to that of φ'' . The pulse dispersion effects considered up to now, and caused by φ'' are called *linear chirp*, because the change of frequency is linear in time. Higher-order expansion coefficients in (3.2) will also cause chirp effects. The *TOD* term φ''' describes a change of frequency which is quadratic in time and is therefore called *quadratic chirp*. For the control of 20fs pulses, as used in our experiments, this nonlinear chirp is already an important contribution.

The dispersion of a transparent material is described by the refractive index $n(\omega)$. Sometimes it is more convenient to work with the wavelength dependent term $n(\lambda)$.² After passing a physical path length l inside a medium, each spectral component of the original signal experiences a phase shift $\varphi = n(\omega)\omega l/c$, where c denotes the vacuum speed of light. The group delay φ' , the linear chirp φ'' , and the quadratic chirp φ''' accumulate due to the material to:

$$\varphi'(\omega) = \frac{l}{c} \left(n + \omega \frac{dn}{d\omega} \right) = \frac{l}{c} \left(n - \lambda \frac{dn}{d\lambda} \right) \quad (3.7)$$

$$\varphi''(\omega) = \frac{l}{c} \left(2 \frac{dn}{d\omega} + \omega \frac{d^2n}{d\omega^2} \right) = \left(\frac{\lambda}{2\pi c} \right) \frac{l}{c} \left(\lambda^2 \frac{d^2n}{d\lambda^2} \right) \quad (3.8)$$

$$\varphi'''(\omega) = \frac{l}{c} \left(3 \frac{d^2n}{d\omega^2} + \omega \frac{d^3n}{d\omega^3} \right) = \left(\frac{\lambda}{2\pi c} \right)^2 \frac{l}{c} \left(3\lambda^2 \frac{d^2n}{d\lambda^2} + \lambda^3 \frac{d^3n}{d\lambda^3} \right) \quad (3.9)$$

Using (3.8) together with refractive-index data, we can calculate values for the *GVD*

²The refractive index n of transparent substances of high density is typically expressed as a SELLMEIER equation with properly chosen coefficients. It is given as a function of wavelength.

arising from material. Figure 3.2 shows the effect for 10mm of Borkron glass (BK7), the most commonly used optical glass, on a short pulse. BK7 is standard material for lenses and 10mm is chosen to represent one or two optical components, which might be part of an experimental arrangement. If we consider a pulse of around 100fs in duration (centered at 600nm), the effect is minimal but visible. However, a 20fs pulse is broadened by a factor of five! The same effect will be achieved by 2mm of Schwerflint glass (SF11) or 23m propagation in air.

A good understanding of dispersion is essential in order to deliver a short pulse to the sample, and careful control of the phase shift is necessary. Fortunately, a number of pulse compressors have been devised by which this can be achieved. There are all-optical techniques using prism and grating pairs or chirped mirrors, as well as electronically driven pulse shapers, which have the advantage of compensating the linear chirp and higher orders of chirp independently. In the next section, we will give a short introduction of the pulse compressing techniques applied to our experiments.

3.1.2 Pulse Compression and Shaping, Characterization

Pulse Compression and Shaping

In the last section, we have seen that pulse propagation in any medium is accompanied by the spectral phases developing apart. The dominant effect is group velocity dispersion (GVD), introducing a linear chirp. Chirp of higher order and self-phase modulation (SPM) might also become important for ultrashort, intense laser pulses. A pulse of a given spectral width can, at least in theory, be reduced in its duration to its FOURIER limit. We will shortly introduce the most successful and widely adopted approaches to recompress and shape optical pulses.

The most common approach of a pulse compressor is a dispersive delay line, formed by a pair of opposing prisms, cut for propagation under BREWSTER's angle, as introduced by FORK et al. [55]. Like in a grating compressor, the dispersion of a prism pair is based on angular dispersion. The first prism spatially disperses the different wavelengths and the second one recollimates the beam. As seen in Fig. 3.3, the optical path through the prism pair is longer for the red part than for the blue part. This system introduces a negative GVD, which can be used to compensate for the positive chirp of normally-dispersive elements, e.g. glass filters. The second pass of the dispersive delay line cancels the spatial chirp on the beam while doubling the dispersion of the system. In the case of the prisms, the dispersion can be varied by changing the amount of prism material. This is simply done by adjusting one of the prisms in a direction normal to its base. In the case of gratings, the dispersion can be varied by changing the distance between the gratings. Even if these two compressors are able to compensate the linear chirp of a pulse exactly, they both introduce nonlinear chirp at the same time. To compensate the linear chirp, double-prism compressors are permanently implemented in our setup. The remaining nonlinear chirp of the pulses, measured by frequency gating, is given exemplarily in Fig. 3.4. By limiting the spectral width of these pulses to about 50nm, we can achieve a minimum pulse duration of 20fs (FWHM) for central frequencies at around 600nm. Spectral selection of the pulses can be achieved inside the compressor by introducing a slit in the spectrally dispersed beam.

The sign of the third-order contribution (TOD) from the grating pair is opposite

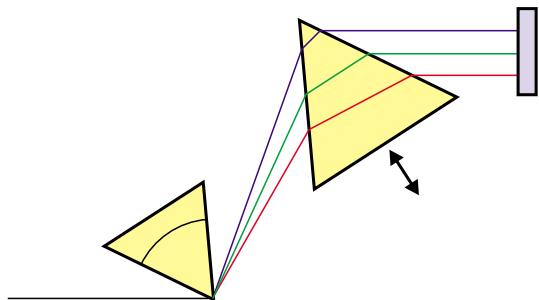


Figure 3.3: Double prism delay line. The central line (green) represents the symmetric path of a plane wave (λ) in BREWSTER configuration. Therefore, the apex angle is chosen to be $\alpha = 2\text{arccot}(n(\lambda))$. The two outward lines (blue and red) represent the beam paths for shorter and longer wavelengths ($\lambda \mp \Delta\lambda$).

to that of the prisms, allowing a combined approach to improve TOD compensation, which has been used to compress 620-nm pulses to 6fs [56]. However, one has to admit that the application of combined prism-grating compressors is quite uncomfortable. In practice, any alignment is very time consuming, and it is difficult to efficiently reduce GDD without exact characterization of the pulse phase. Additionally, the intensity losses are rather high. As an alternative, mirror coatings have been developed, which also can provide second and third-order compensation. This so-called "chirped" mirror reflects each wavelength from a different depth through the dielectric coating, which is made up of multiple stacks of varying thickness. In combination with a prism pair, this technique has been as successful as the grating/prism combination without the associated losses. However, this type of system has to be tailored to the individual requirements and is therefore not flexible to use.

Finally, the pulse compression of white-light pulses by a double-prism compressor was not sufficient for all experiments, e.g. FWM measurements concerning dephasing of exciton transitions (see Sec. 4.2). The remaining nonlinear chirp and, thus, the restricted time-resolution can be overcome the best by use of modern shaping methods.

Over the past decade, powerful computer-controlled optical pulse shaping methods have been developed [57]. These methods can be used for flexible and comfortable control of higher order chirp. Furthermore, they allow generation of complicated ultra-fast optical waveforms according to user specification. The approach most widely used today is based on a *liquid crystal* (LC) modulator array [58]. The pulses have to be dispersed by a grating and collimated onto the transmissive LC array. The LC array allows continuously variable phase control of each separate pixel. Therefore, it allows programmable control of the pulse shape on a millisecond time scale. Independent control of spectral phase and amplitude requires the use of two LC arrays placed between a pair of polarizers.

We use a different approach based on an acousto-optic effect, allowing a flexible chirp control, but with lower losses than the liquid-crystal row approach. The *acousto-optic programmable dispersive filter* (AOPDF) was proposed by TOURNOIS [59] in 1997. As it is available from only one company ("Dazzler" by Fastlite) so far, our lab is equipped with the second AOPDF at all designed for use in the visible !

It is based on collinear acousto-optic interaction in TeO_2 crystal. A main advantage is its simultaneous control of phase and amplitude. The programming of the AOPDF allows arbitrary spectral shapes and phase control up to cubic chirp φ''' . However, the acoustic signal has to be synchronized with the laser timing, what might become critical for pulses of less than 10fs. Furthermore, at 600nm material of 25mm long TeO_2 crystal has to be compensated externally. Therefore, the AOPDF usually has been used in

combination with double prism compressor. At the stage of this thesis, implementation and characterization of AOPDF are not yet finished. None of the results presented herein are gained by the use of it. The final possibilities and limitations of the "Dazzler" for use in the visible are not yet explored.

Measurement of the Pulse Temporal Profile

The characterization of the temporal profile of the laser pulse is the basis of any measurement in ultrashort-pulse laser techniques. Unfortunately, photoelectric response times are seriously limited when one is dealing with picosecond or even femtosecond laser pulses. Although some electronic systems are able to recover pulse envelopes of less than a picosecond (e.g. high-end streak cameras), we use only optical methods based on autocorrelation techniques. All these methods are indirect approaches, and one has to use a model to retrieve pulse shapes from the experimental data. Experimentally, one splits the laser pulse into two replica $\mathbf{E}(t)$ and $\mathbf{E}(t - \tau)$ to be able to construct an autocorrelation function. For instance, the output of an interferometric (collinear) second-order setup is given by $I_2(t)$ as a function of the delay τ :

$$I_2(\tau) \propto \int_{-\infty}^{+\infty} \left| \chi^{(2)} [\mathbf{E}(t) + \mathbf{E}(t - \tau)] \right|^2 dt \quad (3.10)$$

where $\chi^{(2)}$ is the 2nd-order susceptibility of the frequency doubling crystal. Due to the detection in direction of the incident light, this setup always measures a constant background. The maximum contrast is given by 8 : 1. Modifying this technique to the non-collinear geometry one measures the so called "intensity autocorrelation without background":

$$I_2(\tau) \propto \int_{-\infty}^{+\infty} |2\chi^{(2)} \mathbf{E}(t) \mathbf{E}(t - \tau)|^2 dt \quad (3.11)$$

It is often sufficient to measure this type of correlation to obtain the pulse width and the point of zero delay.³

We have implemented a second-order autocorrelator in the shared experimental setup for TA spectroscopy and DFWM. For a cross-correlation between pump and probe pulses only one flipping mirror has to be switched, and the beams are sent to a frequency-doubling crystal instead of the sample. We use a photomultiplier tube (PMT) for detection of the SHG signal. The harmonic signal will only be generated along the bisector of the incoming beams. In this direction, the phase-matching condition for all wavelengths contributing to the pulses has to be fulfilled. For white-light pulses of about 100nm one has to ensure this by choosing an appropriate thin crystal and/or tuning the crystal axis relative to the beam for different central wavelength. Therefore, we use a BBO crystal of only 25 μ m thickness. A typical experimental trace for an autocorrelation is exemplarily given in Fig. 3.6.

³It is generally assumed here that the response time of the SHG process is much shorter than the pulses to be measured, which is reasonable assumption since the second-order nonlinearity is a nonresonant electronic process.

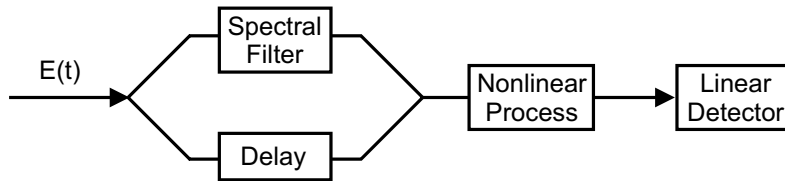


Figure 3.4: Principle of frequency gating. A portion of the pulse spectrum is selected by a spectral filter in one arm of the interferometer. The detected signal is the second-order cross-correlation of the selected portion with the input pulse.

From the intensity autocorrelation trace the *full width at half maximum* (FWHM) τ_{ac} is extracted. As already mentioned, we have to select a realistic pulse shape and compute the expected signal in the intensity autocorrelation function. The best (most optimistic) result can be obtained for a sech^2 pulse, with a reduction factor $\tau_{ac}/\tau_p = 1.543$.⁴ We usually assume a GAUSSIAN pulse shape, which is more realistic for our laser system, with $\tau_{ac}/\tau_p = 1.414$. A list of some more relevant pulse shapes is given in [60].

Phase Measurement

Basically, two different approaches can be used to retrieve the amplitude and phase of a laser pulse. This will completely determine the pulse shape. In time domain, one can measure when a given frequency occurs by *frequency-resolved optical gating* (FROG) of the pulse envelope. In the frequency domain, the time of arrival of a given frequency can be measured. Both methods associate a spectral measurement with a cross-correlation acting as a temporal gate. We have used the second technique of *frequency gating*.

The frequency gating approach is shown in Fig. 3.4. The laser pulse is spectrally filtered before gating it with the original pulse. At each frequency ω_i , one scans the delay τ to find the position of the maximum of the cross-correlation τ_i , while measuring the amplitude $A(\omega_i)$. In the (ω, τ) plane, one obtains directly the derivative of the spectral phase as a function of frequency:

$$\tau(\omega_i) = \frac{\partial \varphi}{\partial \omega}(\omega_i) \quad (3.12)$$

This function is easily integrated and gives the characteristic of the pulse in the frequency domain. The charm of this method is that there is no need of any algorithm! However, the need of spectral filtering might make frequency gating a rather time consuming approach.

Figure 3.5 shows experimental results of a frequency gating measurement. The spectral filtering was done by a pair of razor blades in the spectrally dispersed beam within the prism compressor. The prism compressor was used to remove the linear chirp. The remaining chirp can nicely be fitted by a quadratic function, corresponding to a quadratic chirp of $\varphi''' = 1.6 \times 10^3 \text{fs}^3$.

⁴This is one of the reasons, why most of the scientific community agrees to choose this standard, regardless of the actual pulse shape. The latter has to be analyzed by more sophisticated methods.

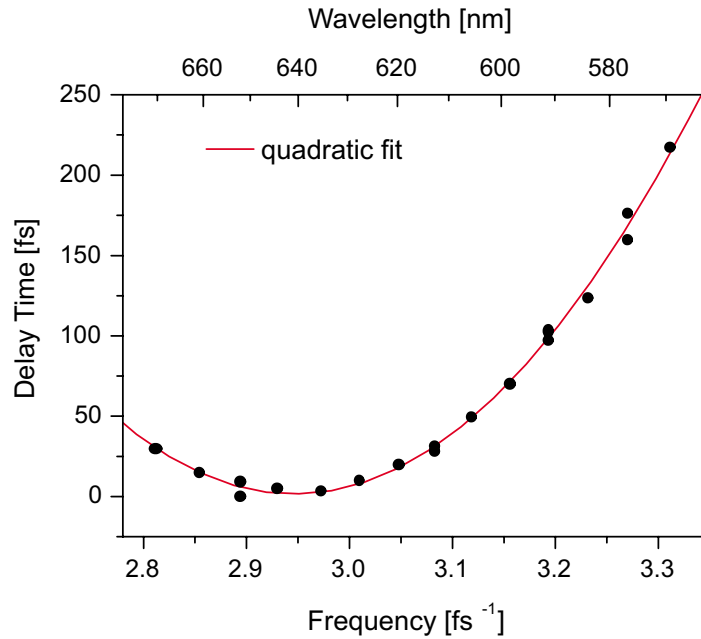


Figure 3.5: Chirp measurement of white-light pulses by frequency gating. The pulses were compressed minimizing the chirp at around 640nm. The measurement reveals the remaining nonlinear chirp which can nicely be described by a quadratic dependence of zero-delay vs. frequency. The solid line is a second-order fit function with the parameter $\varphi''' = 1.6 \times 10^3 \text{fs}^3$. The spectral slices of the white-light continuum are of approx. 10nm (FWHM).

3.1.3 Generation and Amplification of White-Light Pulses

Ultrafast lasers and amplifiers typically operate at a very limited range of wavelengths. For example, Ti:Sapphire-based ultrafast lasers are tunable in the near infrared from about 700 to 1000nm but typically work best at about 800nm. However, the high peak power of these lasers can be used to convert the light to different wavelengths. In fact, in some cases ultrafast laser systems may be the ideal or only route to make radiation at certain wavelengths. We will describe a technique to convert femtosecond laser pulses from a Ti:Sapphire system at near infrared (800nm) to white-light continuum pulses, covering the whole visible spectrum, as used in our experiments.

M.K. REED et al. have shown that tight focusing of less than $1\mu\text{J}$ of 100fs pulses at 800nm into sapphire leads to generation of a single filament continuum [61]. The visible and NIR part of the spectral distribution of such a continuum is shown in Fig. 3.6. The main part of the pulse energy is still contained in the range around 800nm, with significant modulations as a result of *self-phase modulation* (SPM) process. Note, that we have chosen a logarithmic scale to show also the much weaker but nearly flat distribution in the visible range. The continuum pulse is strongly chirped due to SPM and the dispersion in the sapphire itself and needs to be recompressed for experimental use.

White-light generation (WLG) is a rather complex phenomenon which involves changes in the temporal and spatial beam characteristics. However, the dominant process and starting mechanism is SPM. At high intensities, such as on the peak of an

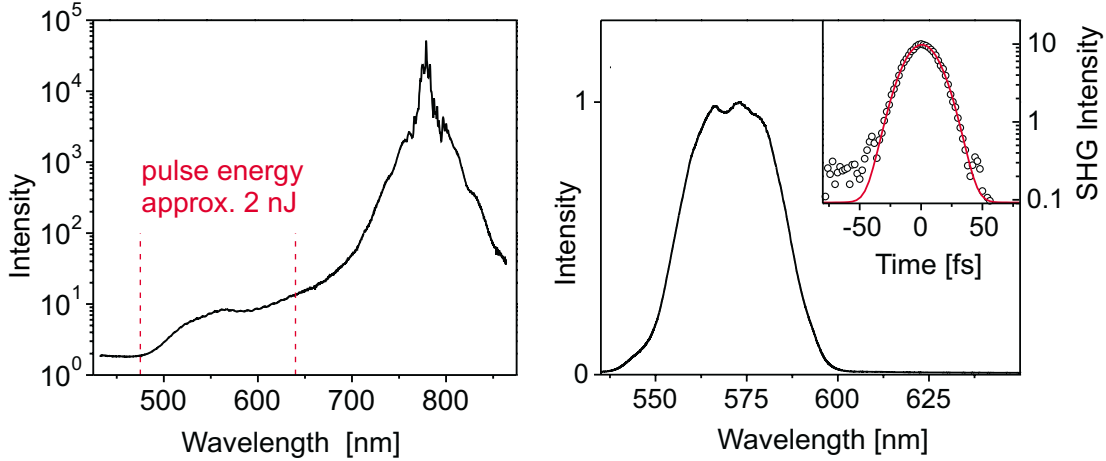


Figure 3.6: Left: Experimental spectrum of white-light continuum pulses generated in a 1-mm sapphire crystal. The dominant peak is at the spectral position of the pump pulses at 800nm. Right: Spectrum of typical amplified white-light pulses as used in the experiments. The pulses are spectrally shaped by razor blades in the prism compressor. The inset shows the accompanying autocorrelation of 33fs (FWHM). This corresponds to a pulse width of 23fs and the bandwidth product results in $K = 0.62$.

ultrashort laser pulse, the refractive index of any medium becomes a function of the incident intensity. This effect, which is often referred to as the optical KERR effect (OKE), can be described by the equation:

$$n(I) = n_0 + n_2 I + \dots \quad (3.13)$$

where n_0 is the normal refractive index of the medium and n_2 is the nonlinear refractive index. The nonlinear refractive index is very small, for example, in fused silica $n_2 \approx 3 \cdot 10^{-16} \text{cm}^2/\text{W}$. What is the influence of this nonlinear modification of the refractive index on the laser pulses? We consider again the electric field of a GAUSSIAN laser pulse

$$E(t) = \text{Re} \left(E_0 \exp(-2 \ln 2 t^2 / \tau_p^2 + i \omega_0 t) \right) \quad \text{e.g.} \quad I(t) = I_0 \exp(-4 \ln 2 t^2 / \tau_p^2) \quad (3.14)$$

The phase of the pulse, after propagation of a short length l of the nonlinear medium, is given by

$$\begin{aligned} \varphi(t) &= n(t) \omega_0 l / c \\ &= \left(n_0 + n_2 I_0 \exp(-4 \ln 2 t^2 / \tau_p^2) \right) \omega_0 l / c \end{aligned} \quad (3.15)$$

The instantaneous frequency, being the time derivative of the phase, can be written as

$$\omega(t) = \frac{\partial \varphi(t)}{\partial t} = \omega_0 - \omega_0 n_2 l / c \frac{\partial I(t)}{\partial t} \quad (3.16)$$

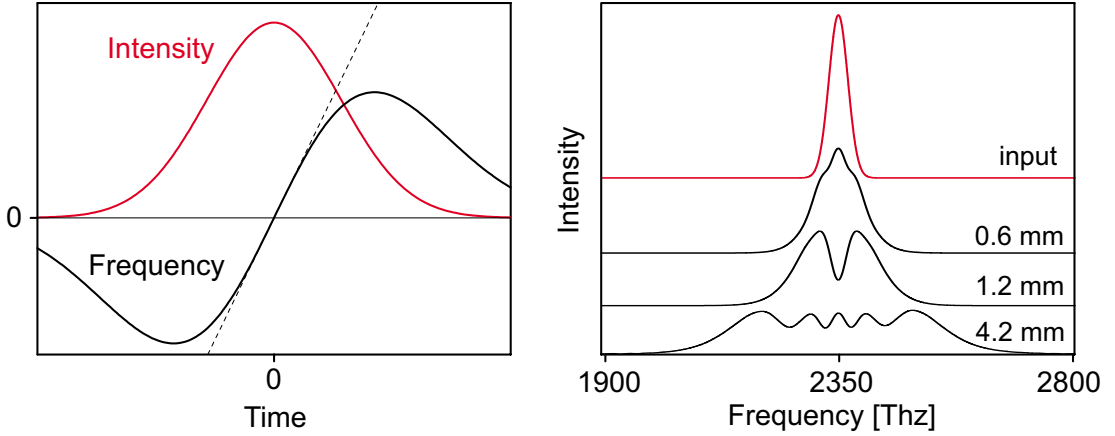


Figure 3.7: Frequency modulation and frequency spectrum of self-phase modulated GAUSSIAN pulses. The left figure shows the instantaneous frequency within the pulse. A TAYLOR expansion around the peak of the pulse shows that the frequency sweep is approximately linear around time zero. The right figure shows the spectral broadening for different propagation lengths l (see text for details).

Assuming n_2 positive, the instantaneous frequency develops in the following way: New low frequencies are created in the leading edge of the pulse envelope and new high frequencies are created in the trailing edge. In other words, the spectrum of the pulse has broadened due to the nonlinear interaction. Because the single pulse modifies its own characteristics this way, the effect is often referred to as self-phase modulation. Expanding (3.16) around $t = 0$ shows, that n_2 induces an approximately linear frequency sweep

$$\omega(t) \simeq \omega_0 - \underbrace{\frac{2\omega_0 n_2 (4 \ln 2) l}{n_0 \tau_p}}_{\varphi''} \cdot t \quad (3.17)$$

similar to the linear chirp found in (3.4). Figure 3.7 shows some examples of the chirp and frequency spectrum of self-phase modulated pulses. The spectral broadening was calculated for 100fs pulses of 100mJ/cm² energy, centered at 800nm, after propagation of the given length of sapphire.⁵ The process of SPM alone, however, is not sufficient to fully characterize the phenomenon of WLG, and a number of other linear and nonlinear effects play a role as well. The self-focusing effect, parametric four-wave mixing, stimulated RAMAN and BRILLOUIN scattering and shock-wave formation may contribute to the broadening of the spectrum [60, 63]. Finally, all these nonlinear interactions must be considered in combination with group-velocity dispersion; the pulses leave the medium strongly broadened in time, as introduced in Sec. 3.1.1.

A stable white-light continuum can be generated in a sapphire plate by a small fraction of the 800nm output of the regenerative amplifier. This commonly used technique was also applied in our setup. The energy of such pulses are restricted to about 0.1nJ in a spectral interval $\Delta\lambda = 10\text{nm}$. Recently, it was reported [64] that, by use of CaF₂ instead of sapphire, the pulse energies can be increased in the visible range by a factor

⁵The numerical simulation of SPM was done by alternating calculations of the linear modulation in spectral domain and nonlinear modulation in time domain [62].

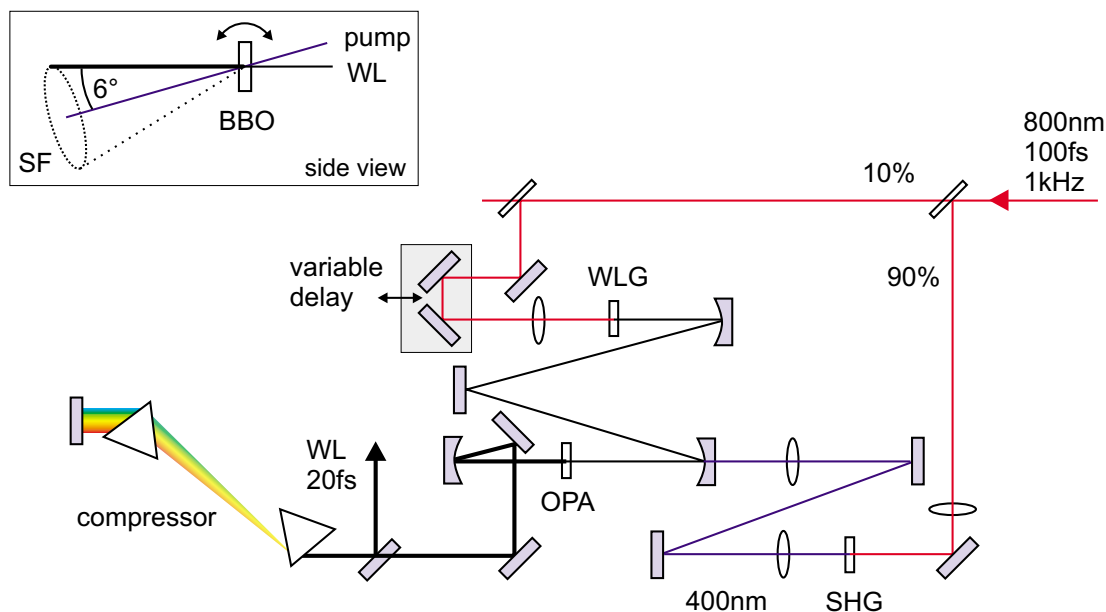


Figure 3.8: Schematic of a non-collinear optical parametric amplifier: SHG, second-harmonic generation (LBO crystal); WLG, white-light generation (sapphire crystal); OPA, optical parametric amplification (BBO crystal). The pump-seed angle matches the apex angle of the superfluorescence cone, as shown in the inset: WL white-light seed, SF superfluorescence ring.

of eight.⁶

The ultrafast spectroscopy applications we are aiming at are nonlinear techniques and require pulses with energy levels in the μJ range. The required amplification of a spectrally broad part of a white-light continuum can be achieved by non-collinear optical parametric amplification, as described in the following.

Non-collinear Optical Parametric Amplification

Non-collinear optical parametric amplification (NOPA) is a technique used to generate sub-20-fs, tunable, visible and near-infrared pulses of μJ pulse energies [65]. In an optical parametric amplifier, photons contained in a short wavelength (blue) pump beam are split into one signal (visible) and one idler photon (NIR) each. The "active" medium is a nonlinear optical crystal, such as a BBO. For efficient conversion, the phase velocities of pump, signal and idler are matched by proper rotation of the birefringent crystal. Unfortunately, this does not simultaneously assure matching of the three group velocities. In collinear geometry, the spectral output of parametric generators and amplifiers is then restricted by the group-velocity mismatch between the pump and the generated signal and idler fields. In a non-collinear arrangement, this effect can be overcome since only the projection of the idler group velocity onto the seed is important. GALE et al. [66] have demonstrated that arranging the pump and seed incidence angles with respect to the phase-matching angle correctly, this group-velocity mismatch can be zeroed in some nonlinear crystals. A NOPA consists of three main functional blocks:

⁶Additionally, the spectrum of the pulses is extended to at least 350 nm. Besides that, the CaF_2 plate has to be moved all the time to overcome damage, making this a rather sophisticated approach. We have not implemented this technique in our setup so far.

- White-light generation of a small fraction of the NIR pump light (e.g. in a sapphire disk).
- Parametric amplification of white-light pulses (which act as seed) in a nonlinear crystal pumped by the frequency doubled pump light.
- Compression of broadband output to 20fs pulses.

As seed pulse, we use a single filament of white-light continuum generated in a 1-mm-thick piece of sapphire. The seed pulses are amplified in type I BBO crystal (cut at $\Theta = 32^\circ, \varphi = 90^\circ$) by the frequency-doubled output of a Ti:Sapphire regenerative amplifier. Type I LBO ($\Theta = 90^\circ, \varphi = 31.7^\circ$) is used to generate the second harmonic of the Ti:Sapphire around 400nm. The pump beam, focused onto the BBO, generates a cone of parametric superfluorescence (inset of Fig. 3.8). When the angle of incidence at the crystal is correct, there is no appreciable spatial divergence of the superfluorescence. By directing the continuum seed beam along the cone axis, a large spectral bandwidth from the white light can be simultaneously phase matched. Adjustment of the relative delay between pump and seed continuum change the center wavelength of the amplified light. An important advantage of this scheme is that relatively thick crystals can be employed (in our case 1mm), which results in high single-pass gain. Amplification factors of up to 10^8 were reported [67], whereas, under working conditions, amplification factors are in the range of 10^5 . Finally, the amplified output has to be recompressed. The broad bandwidth output pulses of the NOPA are chirped due to the initial chirp of the seed continuum and additional chirp caused by the dispersive properties of the BBO crystal, the optics and the air. It could be shown that no additional chirp is added by the amplification process [68]. Pulses as short as 5fs have been generated [69] using a prism/double chirped mirror recompression scheme. Pumping with about $10\mu\text{J}$ of blue light, $2\mu\text{J}$ can be generated at the signal wavelength.

Figure 3.8 shows schematically the NOPA which we have set up for our experiments. It is pumped by an amplified Ti:Sapphire laser system running at a repetition rate of 1kHz (Spectra Physics "Spitfire"). The amplified output is in our case recompressed using a prism pair (quartz, separated by approx. 50cm) yielding 20fs visible pulses continuously tunable from 480 to 700nm. Additionally, the spectrum of the pulses can be shaped by a pair of razor blades in the compressor. A typical example of pulses as used in our experiments is given in Fig. 3.6.

3.2 Spectroscopic Methods

In this chapter, we have dealt so far with ultrashort laser pulses by themselves, their generation and manipulation. Now, we will introduce the experimental methods used in our experiments. First of all, why are ultrashort laser pulses interesting to use for behavior analysis of light-induced perturbations?

Atomic motions, interactions of photoexcited electrons with each other, lattice vibrations of crystals, molecular vibrations, and chemical reactions take place on the femtosecond scale. Nothing but ultrafast pulsed-laser techniques allow direct exploration of this temporal domain. The high time resolution is accompanied by a high bandwidth allowing simultaneous observation of a broad energy range. Besides that,

ultrashort laser pulses can have very large peak power, even for weak pulse energies. Thus, nonlinear spectroscopic techniques may be applied at moderate energy while remaining below the damage threshold of the investigated system.

Two nonlinear methods, *transient absorption* (TA) spectroscopy and *degenerate four-wave-mixing* (DFWM) are applied and will be introduced in the following. As a third method, we use a streak camera for measuring time-resolved luminescence. All methods provide unique information about the various relaxation properties compared with each other (TA: relaxation of optically excited states, phononic wavepackets and dephasing, DFWM: electronic dephasing, TR-Luminescence: radiative recombination). In the end, the combination of the various information allows to draw an extensive picture.

3.2.1 Transient Absorption Spectroscopy

Transient absorption (TA) spectroscopy is a widely used form of pump-probe spectroscopy. Two laser beams with wavevectors \mathbf{k}_1 and \mathbf{k}_2 are focused onto the sample. The first pulse, the so-called "pump" pulse (with \mathbf{k}_1), perturbs the sample at time $t = 0$. The second one, delayed by $t = \tau$ with respect to the pump pulse, crosses the perturbed sample and acts as a probe, this is the so-called "probe" pulse (\mathbf{k}_2).

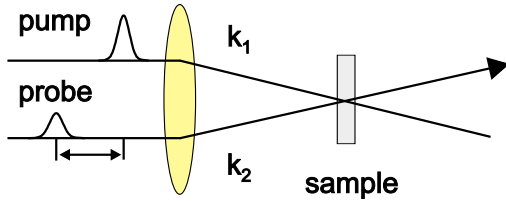


Figure 3.9: Scheme of a transient absorption (TA) experiment.

In the classical theory of electromagnetism, the response of the medium to the incident optical radiation is formulated in terms of the induced macroscopic polarization. For simplicity, we assume an isotropic medium. In electric dipole approximation, one can express the polarization P of sample in a power series of the excitation field strength E :

$$P = \chi^{(1)} \cdot E + \chi^{(2)} \cdot EE + \chi^{(3)} \cdot EEE + \dots \quad (3.18)$$

where $\chi^{(n)}$ is the optical susceptibility of n -th order. In the above equation the term that is quadratic in the field strength describes the lowest nonlinear effect. TA spectroscopy makes use of third-order nonlinear processes described by $\chi^{(3)}$.⁷ The quantity to be measured is the pump-induced change of transmission measured by the probe pulse. The origin of the signal is the third-order polarization which radiates into direction of the probe beam \mathbf{k}_2 :

$$P^{(3)}(\mathbf{k}_2) = \chi^{(3)} \cdot E_{pu}(\mathbf{k}_1) \cdot E_{pu}(\mathbf{k}_1) \cdot E_{pr}(\mathbf{k}_2) \quad (3.19)$$

⁷To be correct, higher order nonlinear effects, such as $\chi^{(5)}$, might also contribute to the TA signal. However, these contributions are expected to be small, and are neglected here.

For a specified wavelength, T_{TA} is the transmission of the probe through the pumped sample and T is the transmission of the probe through the unpumped sample. The fractional change in the probe intensity (often referred to as *differential transmission*) induced by the pump is then given by

$$\frac{\Delta T}{T} = \frac{T_{\text{TA}} - T}{T} \quad (3.20)$$

In this way, the contribution from steady-state absorption is subtracted off. However, one will both measure the linear and the third-order response in the direction of \mathbf{k}_2 :

$$\frac{\Delta T}{T} = \frac{(P^{(3)}(\mathbf{k}_2) + P^{(1)}(\mathbf{k}_2))^2 - (P^{(1)}(\mathbf{k}_2))^2}{(P^{(1)}(\mathbf{k}_2))^2} \quad (3.21)$$

for $\chi^{(3)} \ll 1$:

$$\simeq \frac{2\chi^{(3)}}{\chi^{(1)}} E_{pu}^2$$

where the term $(\chi^{(3)})^2$ has been skipped, because $\chi^{(3)} \ll 1$. The differential transmission is proportional to pump-pulse intensity, whereas it is independent on probe-pulse intensity:

$$\frac{\Delta T}{T} \propto I_{pu} \quad (3.22)$$

This allows to check whether an experimental signal stems from the correct nonlinear process: simply by proving the expected (in)dependence of the signal on I_{pu} and I_{pr} . Another advantage of measuring a probe-independent quantity is the reduction of noise due to fluctuations of probe intensity. Furthermore, we make use of the lock-in technique to effectively reduce noise (see Sec. 3.3).

Population and Phonon Wave-Packet Dynamics

Up to now, we have given a phenomenological description of TA spectroscopy. In this part, we want to introduce a more detailed picture of the interaction within the sample for, at least, a qualitative interpretation of the experiments.

Molecular crystals being optically excited can be described by their electronic and phononic population.⁸ Due to the excitation by the ultrashort pump pulse, the initially prepared system additionally shows electronic and vibrational coherence. The excited states couple to the various electronic and vibrational degrees of freedom, as introduced in Sec. 2.1.2. This will lead to the loss of electronic as well as of vibrational coherence, as well as to depopulation of the initially excited states.

At this stage, we will solely concentrate on *sequential interactions*. That means, we only discuss the signal for positive time delays, after the system has lost the pump-induced electronic coherence. In contrast, *non-sequential interaction* is relevant during

⁸In that context, *phononic* stands for both intramolecular vibrations and intermolecular lattice vibrations.

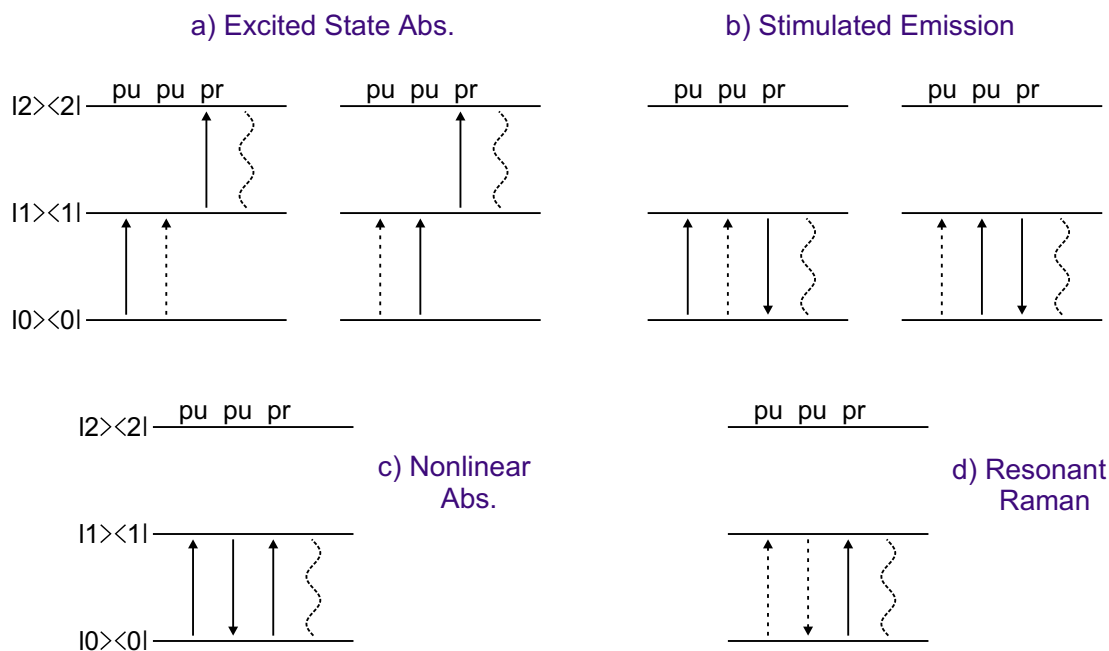


Figure 3.10: Time-ordered diagrams representing the six terms which contribute to the transient absorption at third order. The solid and dashed vertical arrows mark the transitions of the *ket* and *bra* wave functions, respectively, between the electronic surfaces. Time moves forward from left to right. The labels indicate characteristic processes to which each diagram may contribute (adapted from [70]).

the in-phase conditions, e.g. if the probe pulse is coincident with or ahead of the pump pulse. The coherent processes may be superposed on incoherent processes. They are often referred to the "coherence artifact" [54, and references therein] and will be neglected in the following. It should be mentioned that, while neglecting electronic coherence, coherence in the vibrational manifold might still be present.

In the TA experiment, the first (pump) pulse prepares a coherent vibrational state (wave packet) on an excited electronic surface and on the ground-state surface. The second (probe) pulse interrogates the states by absorption or by stimulated emission back to the ground state. The differentiation of population decay and pure vibrational coherence loss is very important. In order to correctly capture this distinction, it is necessary to adopt the density matrix formalism, as done by POLLARD et al. [70]. The theory is based on the third-order susceptibility $\chi^{(3)}$ of a three-level system. Our specific interest is in the temporal behavior of coherent vibrational states and in the exciton population relaxation.

For a system of three electronic states and their associated vibrational manifolds, the polarization response at third order (only the components which propagate in direction of the probe) consists of six terms. The physical meaning of the six terms can be easily understood through a schematic representation as given in Fig. 3.10. The solid and dashed lines denote the *ket*- and *bra*-side evolution of the electronic density at each order of the perturbative interaction with the pump and probe fields. Note that, in stimulating a transition from one electronic state to another, each interaction also transfers a vibrational wave packet from the initial to the final potential surface of the transition. Between field interactions, these *bra* and *ket* wave packets evolve under the

vibrational HAMILTONIANS of their electronic states. The macroscopic polarization is modulated by the time-dependent overlap of the *bra* and *ket* wave packets, which may lead to a rather complex signal.

Pure Population Relaxation

All six terms of Fig. 3.10 may contribute to an experimental signal, and furthermore, every term will transfer information about the population relaxation dynamics as well as information about vibrational wave-packet motion. To simplify the discussion, we disregard any vibrational coherence at this stage. That way, we concentrate on the rather simple discussion of population relaxation dynamics.

- Excited State Absorption (a)

First, the pump pulse moves the initial *bra* and *ket* wave packet to the first excited state (at different times). We can speak of the first excited state as being populated at second order. After some delay period, the probe pulse comes in to send either the *bra* or *ket* wave packet to the second excited state at third order. The resulting macroscopic polarization leads to a *negative* contribution to the differential transmission $\Delta T/T$, and will be interpreted as an excited state absorption. Measuring the transmitted intensity of the probe pulses tells us about the present population of the first excited state. This will change with time (pump-probe delay) as the excited species decay to lower energy states (which might be the ground state, but does not have to be). By measuring the intensity of the transmitted probe at known times after pumping, the population at these times can be deduced.

- Stimulated Emission (b)

The physical interpretation is the same as that of excited state absorption, except that the probe pulse comes in to send either the *bra* or *ket* wave packet to the ground state, describing a third order coherence between the ground and first excited state. The two processes of stimulated emission lead to a *positive* contribution to the differential transmission $\Delta T/T$.

All four processes concerning excited state absorption and stimulated emission represent the excited state contributions to the time-resolved signal since their appearance and behaviour directly reflect the relaxation of the first excited state population created by the pump.

- Nonlinear Absorption (c) / Resonance RAMAN (d)

The ground state contributions to the signal are given by these two processes. The first two interactions of the pump field moves either the *bra* or *ket* wave packet to the first excited state and (partly) back to the ground state. After some delay period, the *ket* is promoted back, up to the excited state by the probe pulse, resulting in the third-order ground-excited state polarization. Physically, the ground-state terms associated with diagrams (c) and (d) account for both the depletion of the initial state and for the process that has been referred to *Stimulated Impulsive RAMAN Scattering* [71]. As any other vibrational contribution,

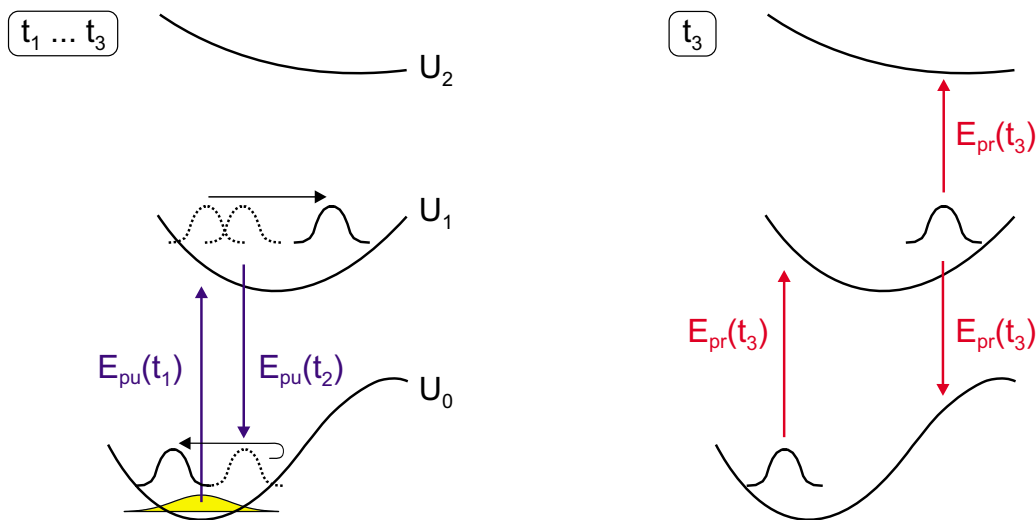


Figure 3.11: Left: Components of the perturbed ground- and excited-state wave functions through second order in the pump field. Vertical arrows mark the transitions between the electronic states at times t_1 and t_2 . Horizontal arrows indicate free propagation of the vibrational wave packets on the potential surface. Right: The probe pulse might couple the wavepackets at $t_3 = \tau$ in three different ways to a different potential surface at third order ($t_1 < t_2 < t_3$).

we neglect this for the moment, and refer to Sec. 4.3. Depletion means a reduced ground state absorption which will lead to a *positive* contribution to the differential transmission $\Delta T/T$. Measuring the transmitted intensity of the probe pulses tells us about the present population of the ground state. This will change with the pump-probe delay as the ground state will be repopulated (the time constant for the depopulation of the excited state will usually be much smaller than for the repopulation of the ground state).

Vibrational Wave Packets

For the discussion of the population relaxation dynamics, we have disregarded the influence of coherent vibrational wave packet motion on the signal. Since the coupling of vibrational modes to electronic transition in OMCs is strong, we have to extend the picture from "pure" electronic states to potential surfaces. What we have called ground state, first excited state, and second excited state are, in a more realistic picture, multi-dimensional potential surfaces coupled to the respective state.

The system begins as an equilibrium vibrational population in the electronic ground state. Upon one interaction with the electric field of the pump, amplitude is impulsively transferred to the excited potential surface, creating phonon wave packets that are a coherent superposition of the phonon eigenstates. Between the certain field interactions of a pump-probe experiment, the non-stationary phonon wave packets evolve under the vibrational HAMILTONIAN of their electronic states.

The concept of separate *bra* and *ket* wave packet propagation, according to the six distinct interaction schemes contributing to the TA signal, is extensively discussed in [70]. At this stage, we simplify the picture of possible interactions, as introduced in the

previous paragraph, neglecting the distinct contribution of *bra* and *ket* wave packets. Finally, we can summarize all six contributions to the TA signal to just one general scheme, as shown in Fig. 3.11. The phonon wave packets, which can be formed on both the ground and the (first) excited potential energy surfaces, will oscillate at the characteristic phonon frequencies of the material and are observed as a modulation of the differential transmission signal [72].

3.2.2 Degenerate Four-Wave Mixing

To study the coherent regime of optically excited free excitons, *four-wave mixing* (FWM) is the suitable technique. FWM is, like transient absorption (TA) spectroscopy, a pump-probe technique which is sensitive to the nonlinear third-order polarization $\chi^{(3)}$, as introduced in (3.18). A comprehensive study of FWM spectroscopy can be found in, e.g. [73, 74]. The electric fields of three incoming beams produce a nonlinear polarization which leads to the emission of a fourth signal beam in a background-free direction. In this work, we restrain ourselves to the case of *degenerate four-wave mixing* (DFWM), i.e. all fields have the same frequency ω . In particular, the method of *self-diffracted* DFWM is employed. In this case, two laser beams with wavevectors \mathbf{k}_1 and \mathbf{k}_2 are focused onto the sample - the second pulse \mathbf{k}_2 interacts twice with the sample. The third order polarization of this particular type of FWM is given by:

$$P^{(3)}(\mathbf{k}_3) = \chi^{(3)} \cdot E(\mathbf{k}_1) \cdot E(\mathbf{k}_2) \cdot E(\mathbf{k}_2) \quad (3.23)$$

The direction of the signal beam is given by the phase-matching condition:

$$\mathbf{k}_3 = 2\mathbf{k}_2 - \mathbf{k}_1 \quad (3.24)$$

The basic principle of the method is shown in Fig. 3.12 and can be described as follows: The first ultrashort pulse (\mathbf{k}_1) is focused onto the sample and interacts once with the sample by inducing a macroscopic polarization. The polarization oscillates in the sample and instantaneously starts to dephase due to scattering events with the characteristic electronic dephasing time T_2 . The second pulse with wavevector \mathbf{k}_2 , which is delayed in time by τ , interacts twice with the sample: First, it interferes with the remaining polarization of the first pulse \mathbf{k}_1 which results in a population grating with grating vector $(\mathbf{k}_2 - \mathbf{k}_1)$ in the sample. The grating represents a modulation of optical properties due to the excited carriers or excitons in the respective bands. Second, the electric field of the second pulse will be diffracted on the grating with interference maxima of the third order polarization in the background-free direction $(2\mathbf{k}_2 - \mathbf{k}_1)$. When the two pulses are separated in time, a grating can still be formed, provided that the dephasing time T_2 is sufficiently long. Since the persistence of the grating relies on the coherence of the polarization induced by the first pulse $[\propto \exp(-\tau/T_2)]$, the recorded transient intensity provides information about the dephasing of the electronic states involved. The scattered DFWM intensity in the background free direction reads:

$$I_{\text{DFWM}}(\tau) \propto \int_{-\infty}^{+\infty} dt |P_{\mathbf{k}_3}^{(3)}(t)|^2 \quad (3.25)$$

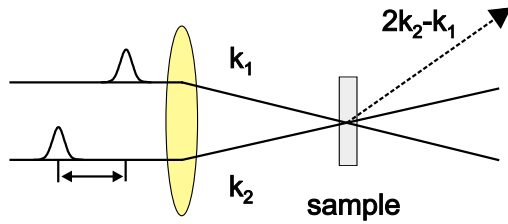


Figure 3.12: Scheme of a four-wave mixing (FWM) experiment.

In the case of an *inhomogeneously* broadened transition, the situation is more complicated: The net polarization decays rapidly due to destructive interference of excitations with different energies, although no scattering processes are involved. The second interaction of the second pulse inverts the phases of the excitations, which leads to the observation of a "photon echo" after a delay time which is identical to the delay time between the pulses. Since we only trace the time-integrated diffracted signal as a function of the delay τ between the two pulses, we cannot directly observe the echo pulse.

A detailed theoretical account of the self-diffracted DFWM experiment has been given by YAJIMA and TAIRA [75], starting out from a two-level system. It solves the equations of motion up to third order in the density matrix formalism in the analytically solvable δ -pulse limit. The dephasing is introduced phenomenologically. In real materials, the excitonic system is coupled to a bath of other degrees of freedom (vibrons, phonons, solvent modes, etc.). The bath is assumed to be either very fast or very slow compared to the characteristic inverse exciton-bath coupling. The broadening of the linear absorption line shape in these two limits is usually denoted *homogeneous* and *inhomogeneous*, respectively. A *homogeneously* broadened transition is described by a LORENTZIAN function, and in many cases, one assumes a GAUSSIAN distribution for *inhomogeneous* broadening. The dependencies of the diffracted signal for $\tau > 0$, as calculated by YAJIMA and TAIRA, are found to be:

$$I_{\text{DFWM}}^{\text{hom}}(\tau) \propto \exp(-2\tau/T_2) \quad (3.26)$$

$$I_{\text{DFWM}}^{\text{inhom}}(\tau) \propto \exp(-4\tau/T_2)$$

The dephasing time T_2 should correctly be named "phase-relaxation time of the free induction decay", to point out the intrinsic character of this quantity. At high excitation densities the dephasing will be accelerated mainly by exciton-exciton scattering [76, 73]. We will discuss this point more detailed in the experimental part (Sec. 4.2).

3.2.3 Time-Resolved Luminescence

Measurements of time-resolved (TR) luminescence usually require not the very high time resolution as, e.g., the measurements of electronic or phononic dephasing. Detection in the time range from several tens of nanosecond down to about a picosecond is very conveniently covered by streak cameras. The basic principle of a streak camera is given in standard ultrafast text books or on the web pages of manufacturers [74, 77, 78]. Therefore, we give here only the very basic principles.

An incident photon produces a photo-electron on the photocathode of the streak tube, the central element of the streak camera. Thus, the photocathode converts the

photons into electrons. These electrons are accelerated towards a phosphorus screen by electrodes. A high-speed high-level voltage synchronized to the incident light is applied to the sweep electrodes, so that the advancing electrons are swept in the direction from bottom to top. The sweep electrodes "streak" the electrons vertically along the screen transforming a delay into a spatial separation. The swept electrons fly to an micro-channel plate (MCP), where they undergo amplification. An electron can be multiplied into as many as 1000 using this process. Finally, the electrons arrive at the phosphorus screen, where they are converted back into light.

The entrance slit of the streak camera which is imaged on the photo-cathode is additionally placed in the the exit plane of a spectrometer. Spectral and temporal resolution are arranged perpendicular to each other. This setup allows one to measure the signal intensity directly as a function of photon energy and of time. The optical image produced on the phosphorus screen is called the "streak image". A CCD camera is used behind the screen to read out the streak image.

The streak camera is used in connection with a mode-locked laser running at a repetition rate of 80MHz. As we use the streak camera to accumulate over many excitations, the exciting pulse train has to be synchronized to the sawtooth-deflection voltage of the sweep unit. Therefore, a portion of the excitation beam is diverged by a beam splitter and received by a high-speed detector to serve as trigger signal.

When a phenomenon is being repeated in order to measure it (streak images are being added), the position of the streak image on the phosphorus screen slightly changes each time the phenomenon is repeated, because of fluctuation in the operating timing of the sweep circuit. This fluctuation is called trigger jitter and might limit the time resolution of the system. The time resolution of the whole experiment can also be limited by the length of the laser pulses and the fluctuations of the repetition rate of the laser system (laser jitter).

3.3 Experimental Setups

Because the experimental setups of TA and DFWM spectroscopy are similar in their setups, we treat them together in the next section. The setup for time-resolved luminescence is rather simple, and a streak camera is a commercial and standardized tool. We do not present all experimental details, just stress the crucial points.

Common to all experiments is the possibility to measure at low temperatures. We have used a continuous flow cryostat "Optistat" (Oxford Instruments), which allows to cool the sample down to the temperature of liquid helium of 4.2K.

Transient Absorption and Four Wave Mixing

The TA and DFWM experiments require a similar experimental setup. The general setup in its specific TA geometry is shown exemplarily in Fig. 3.13. In TA spectroscopy, the intensity of the weaker probe beam \mathbf{k}_2 transmitting the sample is detected as a function of the delay τ with respect to the stronger pump beam \mathbf{k}_1 . Therefore, probe pulses stem from WLG, whereas pump pulses stem from NOPA amplification. The expected transient changes in intensity are in the order of 10^{-4} , so, to efficiently cancel

out laser noise, differential detection was utilized.

The pump beam is chopped mechanically to give a series of pump pulses at half the repetition rate of the probe. This requires a chopping system, which is phase-locked to the laser-pulse source, in our case to the regenerative amplifier (Spectra Physics "Spitfire"). In this way, every 2nd probe pulse measures the unpumped (ground-state) absorption, while the $(2n+1)$ th probe pulses measure the pumped (excited-state and remaining ground-state) absorption. A disadvantage of this technique is the very small *fill factor* for the lock-in amplifier: The detection using lock-in technique integrates the signal as well as the noise over the time of two successive pulses. In our case the integration time is 2ms (corresponding to 500Hz repetition rate for the pump pulses), whereas the signal generated in the sample will usually have a time constant in the sub-ns regime. The fill factor, defined by the ratio of the time constants, would be in the range 10^{-6} . That sounds dramatically, but this is not the whole truth: Already the response time of the used photo detector (Si-PIN diodes) will stretch the signal to more than 10ns. The differential amplifier, used to subtract the reference signal, was driven to further stretch the electronic signal by several orders of magnitude (without impeding the dynamic range of the signal). Finally, we obtain fill factors of about 10^{-2} , what is sufficient for our experiments. However, one might use a combined electronic system applying the techniques of a boxcar/lock-in or sample&hold/lock-in to efficiently maximize the fill factor [79].

For frequency resolved TA measurements the probe and reference pulses have to pass a monochromator before detection. We do this by arranging both beams parallel but vertically separated in front of the monochromator. The beams are then focused in the horizontal plane with a single cylindrical lens to the entrance slit of the monochromator.

The setup for DFWM experiments is similar to that of TA spectroscopy (see Fig. 3.13) with some modifications: White-light pulses, amplified by the NOPA, are used for both the pulse trains \mathbf{k}_1 and \mathbf{k}_2 . The DFWM signal in the phase matching direction $2\mathbf{k}_2 - \mathbf{k}_1$ is selected by an aperture, which blocks the transmitted pulses. Furthermore, the signal is imaged to an intermediate image plane, where another spatial selection is done using a cross slit. Finally, the signal is focused on the detector.

Time-resolved Luminescence

The setup for time-resolved luminescence is rather simple, therefore we do not present a scheme of it. The excitation was done using a KERR-lens mode-locked Ti:Sapphire laser providing ps-pulses at 880nm at a repetition frequency of 80MHz. A portion of the excitation beam is diverged by a beam splitter and received by a high-speed photodiode, to serve as trigger signal as described in Sec. 3.2.3.

The laser pulses were frequency doubled using a 3mm BBO crystal to excite MePTCDI above the lowest four excitonic transitions. For detection we use a streak camera "Hamamatsu C 5680" (tube type: N5716 - covering a spectral range of approx. 250 – 750nm) with a synchroscan unit "M 5675". This streak-camera setup allows a maximum time resolution of 2ps. However, the time resolution of the experiment is not necessarily limited by the Streak Camera and/or length of the laser pulses. Crucial for a multishot streak experiment is the requirement of a synchronization of the exciting laser pulses with the detection system. If the repetition jitter of the laser is larger than

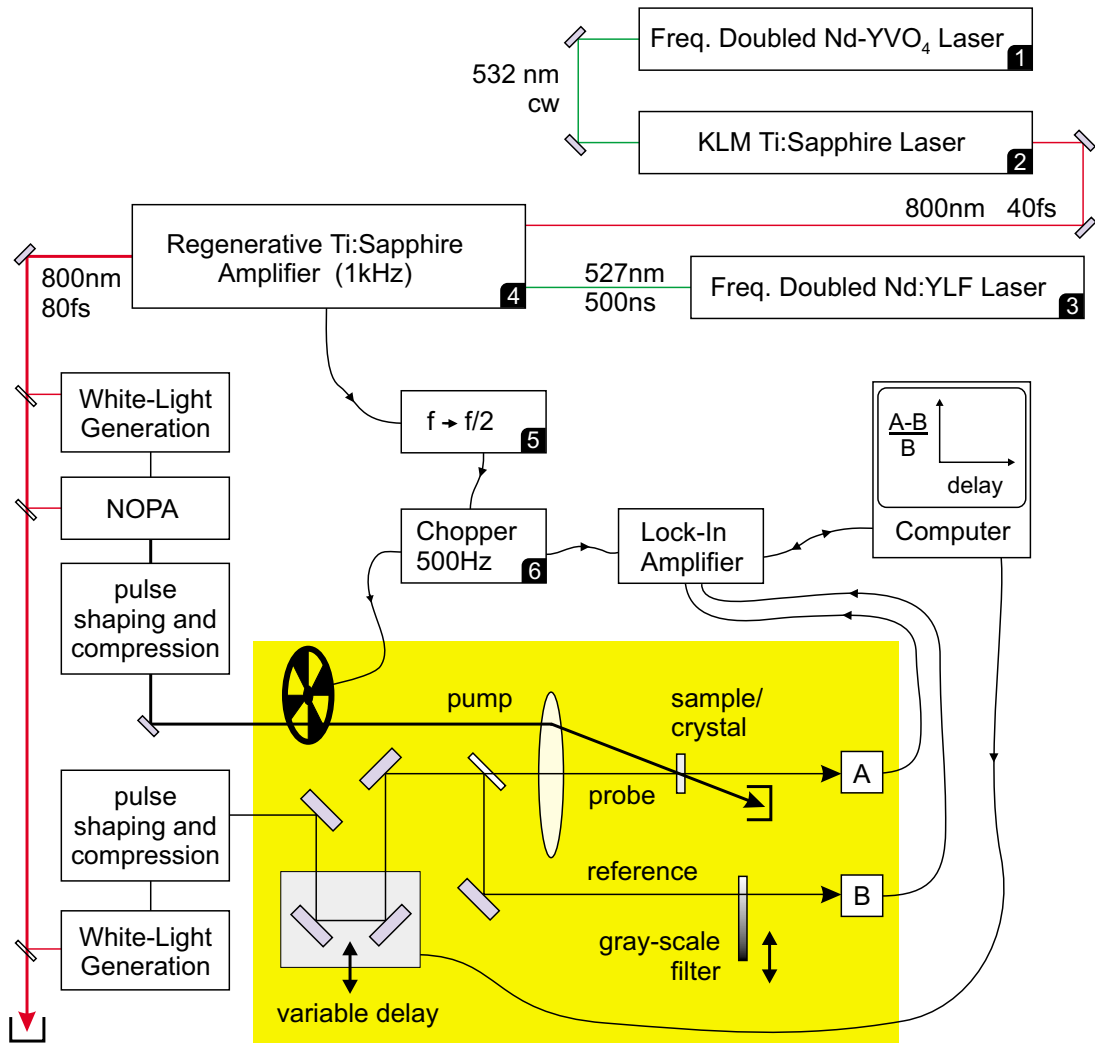


Figure 3.13: General experimental setup for transient absorption (TA) spectroscopy. The beam path of the intense pump is depicted as a thick line. The pulses from the non-collinear optical parametric amplifier (NOPA) and white-light generation (WLG) might be spectrally shaped, and are compressed to its temporal minimum. The detector A and B are diodes or photo-multiplier tubes (PMT), and might be placed behind a jointly used spectrometer (frequency-resolved measurements). When using diodes, the subtraction $A - B$ is done by a low-noise preamplifier (SRS, Model SR 560). For the case of PMT, two current amplifiers (HMS, Model 564) are used, and the subtraction $A - B$ is done by the lock-in amplifier itself.

- 1.) "Millenia V" (Spectra Physics; 5 W cw).
- 2.) Kerr-lens mode-locked Ti:Sapphire laser (homemade; 1 nJ pulses).
- 3.) "Merlin" (Spectra Physics; 10 mJ pulses).
- 4.) "Spitfire" (Spectra Physics, 1 mJ pulses).
- 5.) Frequency converter to divide in half (homemade).
- 6.) Phase-stabilized chopper (HMS, Model 221).

2ps, it is limiting the time resolution of the experiment. And this is the case in our experiments: The highest time resolution, which is achieved in time range II, is limited to 10ps.

4 Experimental Results and Discussion

In this chapter, the experimental data, their evaluation and discussion are presented.

First, the energy relaxation of the electron system will be investigated. Therefore, we present data from time-resolved (TR) luminescence and transient absorption (TA) spectroscopy. After optical excitation, the free excitons relax very fast towards emitting states, and from these states they will be transferred back to the ground state, partly by radiative recombination. Second, we investigate the coherent properties of the electron and phonon system. We discuss the homogeneous linewidth of the optical transition to the lowest free-exciton band by use of four-wave mixing results. Furthermore, the observation of wavepackets of intramolecular and lattice phonons will be presented. The data from TA spectroscopy are compared to theoretical calculations and literature data from different experiments.

4.1 Excitonic Relaxation

By illuminating MePTCDI with visible light ($> 2\text{eV}$), we excite optical transitions to free-exciton states at $k = 0$. The Eigenfunctions of such a free exciton are BLOCH wave functions spread over the (perfect) crystal. However, in its relative coordinate, describing the electron - hole separation, the BOHR diameter is in the range of the smallest lattice constant, depending on its actual band state. What will happen to such a free exciton? And, what are the time scales for the various relaxation processes?

The relaxation of free excitons is investigated by TR luminescence and TA methods. The two techniques obtain different information on different time scales. Fortunately, both methods have sufficient overlap in their time resolution: The TA experiment has access to the sub-ns time range, down to a maximum time resolution of about 20fs. The streak technique, as used in our experiments, works in the sub-100ns time range and has a lower limit of 10ps. By investigating TR luminescence, we try to learn something about the nature of the emitting states, the relaxed excited states. Furthermore, we collect information about the recombination to the electronic ground state. In contrast, TA spectroscopy monitors both emission and absorption processes, involving also higher excited states. We use TA spectroscopy in order to get insight into the very first steps of free-exciton relaxation. The high time resolution and its power to observe population changes allow to investigate the ultrafast depopulation of the initially excited free-exciton states.

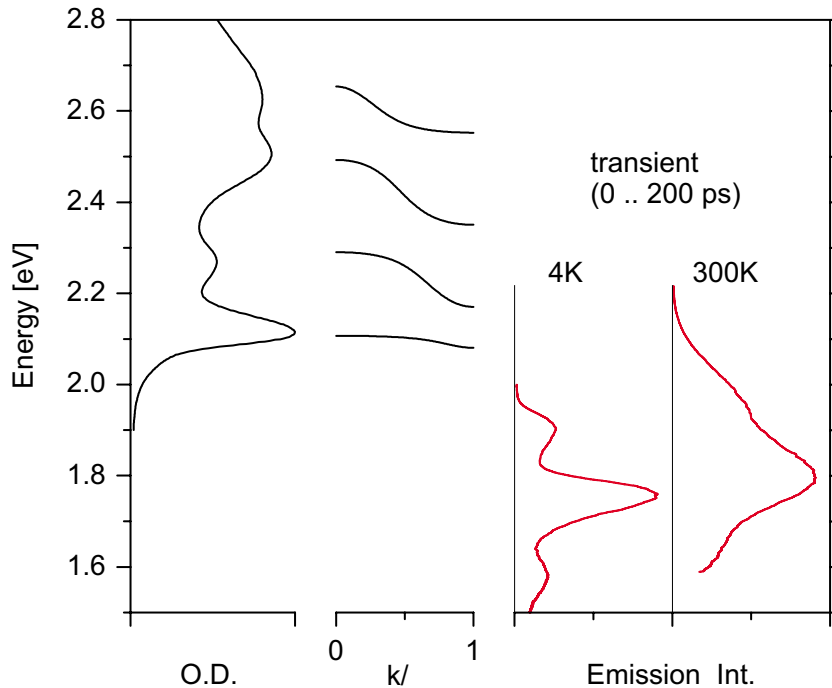


Figure 4.1: Absorption and emission spectra of MePTCDI. The diagram in the center shows the exciton-band structure as introduced in Sec. 2.3.1. The absorbance spectrum (left) is from a polycrystalline thin film sample at 4K. The emission (right) is from a single crystal. Shown is the transient luminescence of the first 200ps after short-pulse excitation at room temperature and at 4K.

4.1.1 Radiative Recombination from Relaxed Excited States

A complete description of exciton-energy relaxation in quasi-1D OMCs involves various steps, starting with the initial, very fast depopulation of free excitons towards emitting states and ending with the final recombination of the relaxed excitons. The radiative recombination can be observed in experiments of TR luminescence.

TR luminescence of MePTCDI was measured using a streak-camera setup. We investigate both technologically relevant polycrystalline layers as well as single crystals (details given in Chap. 1) to separate the influence of defects. All luminescence measurements were performed using a frequency doubled Ti:Sapphire laser for excitation at around 440nm. With this setup, a maximum pulse energy of about 0.5nJ is available. To prevent sample heating or high-excitation effects, pulses of typically 10pJ were used. The luminescence signals were recorded using a streak camera as described in Sec. 3.2.3. The given spectra are corrected concerning the spectral response of the spectrometer and the streak camera.

Figure 4.1 shows the luminescence of a single crystal at low and at room temperature. The given emission spectra are the transient signal, time-integrated over the first 200ps after excitation. Besides narrower linewidths, the spectra are very similar to the emission of thin-film samples. As the emission properties depend much more on defects than, e.g. absorption, this proves that our thin film samples are, at least, of reasonable crystal quality. The most conspicuous feature is the large STOKES shift of the

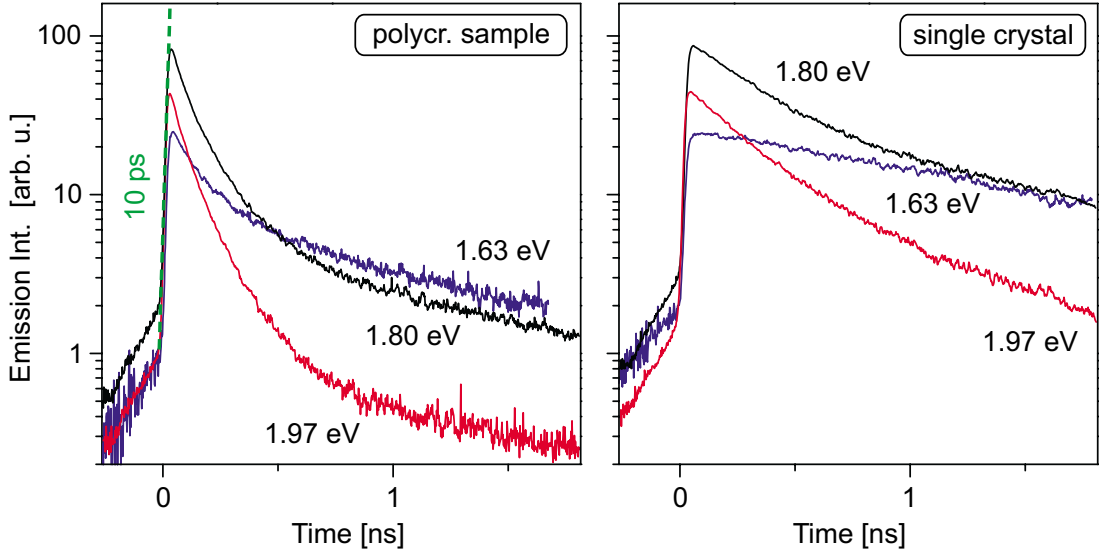


Figure 4.2: Time-resolved luminescence of MePTCDI at room temperature. The decay of emission of the main peaks at around 1.97eV (h-en.), 1.80eV (m-en.), and 1.63eV (l-en.) for a polycrystalline thin film and a single crystal is shown.

luminescence relative to absorption of about 200meV, compared to only 30meV for the molecules in solution (see Fig. 2.3). We have depicted the predicted free-exciton bands to show the large energetic shift of the low-temperature emission to any free-exciton state, even for $k \neq 0$. The emission spectrum shows three distinct peaks: for low temperature the highest energetic (h-en.) peak is at 1.90eV, the next lower energetic peak (m-en.) is at 1.75eV, and the lowest energetic (l-en.) peak is at 1.58eV. The energetic shift of the peaks from 4K to 300K is in the range of 50 – 70meV, accompanied by a broadening of the emission peaks by a factor of two.

The emission of the peaks at room temperature is noticeably non-exponential in

Table 4.1: Results of exponential fit to the decay of MePTCDI luminescence. Given are values for the main peaks (high energetic (h-en.) peak: for 300K at 1.97eV, for 4K at 1.90eV; middle energetic (m-en.) peak: for 300K at 1.80eV, for 4K at 1.75eV; low energetic (l-en.) peak: for 300K at 1.63eV, for 4K at 1.58eV) for a polycrystalline thin film and a single-crystal sample. The decays at room temperature are not well described by a single-exponential law. To take this into consideration, we used two independent exponential functions (respective time windows 0 – 0.5ns and 0.8 – 1.7ns) resulting in two time constants.

peak pos.	polycr. thin film			single crystal		
	h-en. [ns]	m-en. [ns]	l-en. [ns]	h-en. [ns]	m-en. [ns]	l-en. [ns]
T = 300 K	0.13 / 1.3	0.15 / 1.3	0.3 / 1.3	0.36 / 0.8	0.45 / 1.2	1.6 / 1.6
T = 4 K	13 ± 2	11 ± 2	14 ± 2	75 ± 10	50 ± 10	50 ± 10

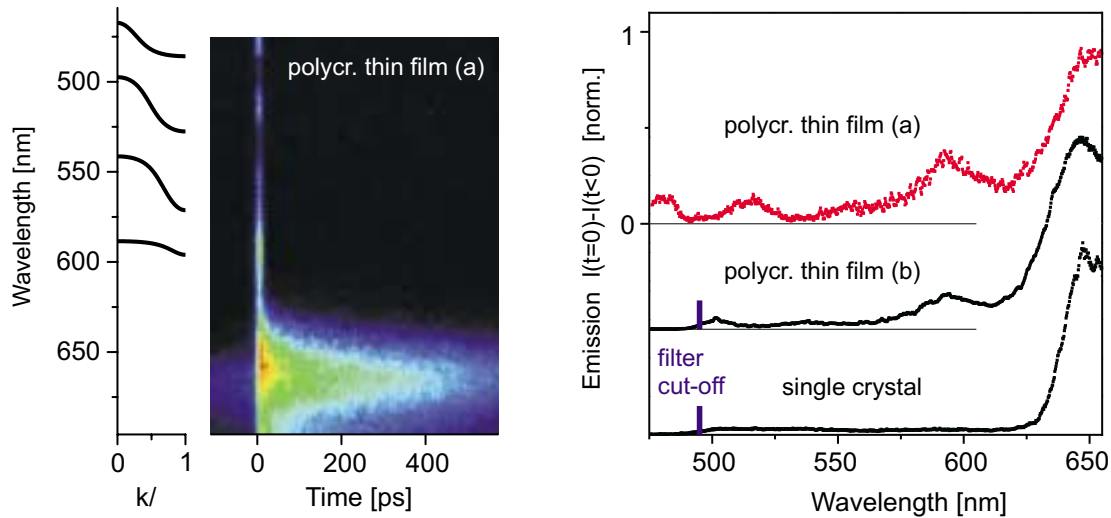


Figure 4.3: Time-resolved luminescence spectra of MePTCDI at 4K. The left diagram shows a color plot for a polycrystalline thin-film sample (a). The exciton-band structure as introduced in Sec. 2.3.1 is additionally shown. The plot shows the long-lived luminescence of the highest energetic emission peak, the lower ones are out of the given energetic window. At times around $t = 0$ this sample shows very short-lived luminescence at energetic positions of the predicted band structure. The spectrum of the luminescence of the first 40ps after short-pulse excitation is given as the upper graph in the right diagram. A different thin-film sample shows agreement only for the emission around 590nm. However, the single crystal shows no significant emission within the energetic range of the free-exciton bands. See text for discussion.

time, as shown in Fig. 4.2. The measurements were performed at rather low excitation densities using pulses of about 10pJ. We have checked the decay dynamics to be independent of excitation density for several orders of magnitude. The non-exponential decay could at least partly be attributed to the presence of defects: It was found that polycrystalline samples grown at higher substrate temperature and therefore with larger crystallites and less crystal defects show luminescence decays with the non-exponential contribution significantly reduced [12].

The decays were simply fitted by two independent exponential decays for different time windows (see Fig. 4.2). This is because of the lack of a deeper understanding of the processes leading to the non-exponential decay. As we use the obtained decay constants only for comparison, the robustness of this simple fit is advantageous. The luminescence decays at low temperature are much slower. Within the time window of two successive excitation pulses (12.5ns) emission does not vanish. Therefore, the fits for the first 12.5ns contain only a single exponential law for both polycrystalline and single-crystalline samples. The error of this procedure is estimated to be rather large. Typical values of the fits are given in Table 4.1.

The rise of luminescence directly after excitation can be fitted by an exponential function with a time constant of 10ps. This value is limited by the time resolution of the streak-camera setup. The 440nm laser pulses ($= 2.82\text{eV}$) excite high-energetic free excitons. These states are well above the highest band as described by the exciton model. The relaxation from the initially excited states down to the lowest, relaxed exciton states, from which luminescence arises, has a time constant of less than 10ps.

This is already a crucial information from measurements of TR luminescence. We will use this result for the interpretation of TA measurements (see Sec. 4.1.3). Finally, it turns out that relaxation from free-exciton states at $k = 0$ to the emitting states is an ultrafast process on a time scale of less than 100fs.

An interesting observation could be made for the transient emission in polycrystalline samples at very early times: The color plot of Fig. 4.3 shows emission features at energetic positions of the predicted band structure for $t \approx 0$. This emission can not be observed in time-integrated measurements because of its very short life time. We can not determine a decay constant due to the limited time resolution of the setup. However, the maximum value is given by 10ps. These emission features were only observed for polycrystalline samples. For single crystals, they are completely absent, as shown in Fig. 4.3. Therefore, this emission can not be assigned to intrinsic crystal states, probably it stems from defects. Further measurements on different samples support this interpretation: Even if the dominant short-lived luminescence at 590nm was present in comparable samples, it differs in intensity. However, other small features are not reproducible, as shown for two different thin-film samples. From comparison with measurements of single crystals, artifacts by stray light can be excluded. Nevertheless, there might be a connection of the short-lived emission features to the band states. One might imagine defect states strongly coupling to the free-exciton band states. The luminescence from these defects might be quenched by a self-trapping process and therefore show up only at very early times. However, ideas like this are highly speculative and need further experimental investigations.

The quantum efficiency of isolated MePTCDI molecules in solution is of about 93% [81]. In contrast, the internal quantum efficiency of evaporated thin films of MePTCDI at room temperature was measured to be only 3 – 4% [80]. This quantity is defined as the number of photons emitted per photons absorbed, taking into consideration the outcoupling losses and reabsorption. Thus, the decay dynamics in thin films are dominated by nonradiative recombination processes. To our knowledge, there are no reports on the fluorescence quantum yield for single crystals of MePTCDI or similar perylene derivatives. However, luminescence of single crystals of MePTCDI decays distinctly slower (see Fig. 4.2), especially at low temperatures. This suggests that the low fluorescence quantum yield is not an intrinsic property, but caused by defects. We do without a quantitative analysis, as our thin films are probably not comparable to the samples used in [80]. Nevertheless, the intrinsic fluorescence quantum yield of the MePTCDI crystal will be much larger than the value found for evaporated thin films.

Finally, after discussing the various luminescence properties, the question arises: What is the nature of the emitting states?

4.1.2 The Nature of Relaxed Excited States

Even though the knowledge about optical absorption of crystalline MePTCDI is already understood in principle, relaxation and recombination processes are still puzzling. We have discussed the emission properties in the previous section. Let us first summarize the obtained knowledge, which might be helpful for the following discussion. Concerning luminescence, we found:

- a large energetic shift between lowest absorption and highest emission (STOKES

shift) of about 200meV,

- a spectral shape with three peaks,
- a strong temperature dependence of the emission spectrum (broadening and blue shift for increasing T),
- a low fluorescence quantum yield (only 3 – 4% for polycrystalline samples; unknown for single crystals, but probably much higher),
- and a strong change of the transient emission spectrum with time.

What is the physical origin of the emission features with its two main peaks? There are at least two possible and reasonable explanations:

1.) Band states at $k = \pi$

In the case of a rigid lattice, the band-like description of free-exciton states would not only explain the absorption properties, but it would also hold for the emission properties. By optical excitation of the lowest free-exciton band, states at $k = 0$ are populated. The subsequent relaxation to the emitting states is simply a relaxation to the band edges at $k = \pi$, as shown in Fig. 4.4. This is accompanied by the emission of low-energy phonons, or in other words, by redistribution of the various excited vibrational degrees of freedom. As a consequence, recombination, solely by emitting a photon, is dipole forbidden due to the requirement of the conservation of momentum k . Thus, the emission spectrum would need to be explained by phonon-assisted recombination. In this context, a low fluorescence quantum yield seems reasonable. By radiative recombination, the crystal goes into the electronic ground state, which is not relaxed in its phononic degrees of freedom. The three observed peaks would correspond to the vibronic progression of an effective phonon mode in the electronic ground state ($\phi^{01}, \phi^{02}, \phi^{03}$ - compare Fig. 2.1). The observed splitting of the peaks at low temperature is of about 0.15eV for the two upper (01 – 02) and 0.17eV for the two lower energetic peaks (02 – 03). That differs only slightly from the values of the *effective mode* $\hbar\omega = 0.17\text{eV}$ for (01 – 02) and 0.14eV for (02 – 03) of molecules in solution, as derived from Fig. 2.3.

However, because of the different decays of the transitions, this explanation becomes questionable. The spectral shape of emission from one common excited state to several different states would not change in time. This can only be understood by assuming more than one emitting state. Very recently, KOBITSKI et al. proposed a simple model which is capable to explain a similar luminescence decay for PTCDA [51]. Due to the existence of two molecules within the unit cell, all states exist as a DAVYDOV-split doublet. Then, the spectral change of luminescence in time can be explained by different radiative lifetimes for the doublet states.

2.) Self-trapped States

After optical excitation, free excitons will interact with phonons. For the dimer-like crystal of α -perylene, strong exciton-phonon interaction was shown to result in solid-state excimer formation [23]. For the perylene derivative MePTCDI, the crystal of which is not dimer-like, exciton-phonon interaction is expected to be strong [24] (see

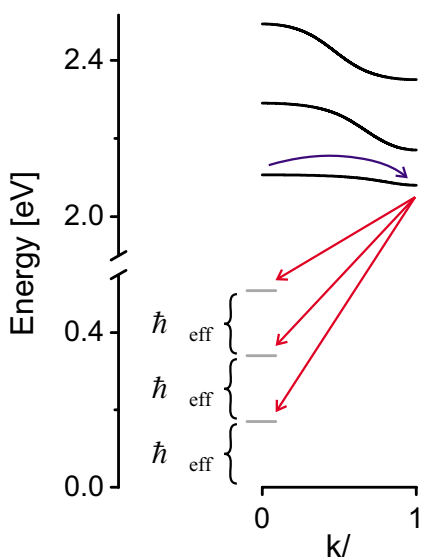


Figure 4.4: Excited-state relaxation and recombination in a band-like description. An optical excitation populates free exciton states at $k = 0$. Intraband relaxation to the band edges at $k = \pi$ is visualized by a bent arrow. Allowed optical transitions to the three lowest energetic states are phonon assisted (given as straight arrows).

Sec. 2.2.1). In that case, the crystal can not be treated as a rigid lattice anymore. Excitons might be trapped by lattice distortions, produced by excitons themselves (see Sec. 2.5). In contrast to self-trapping in the gas phase and in solution (excimer formation) with only one broad emission band, in solids one sometimes encounters an additional precursor state. The existence of self-trapping precursor states is inferred from low-temperature spectral studies of a number of materials [22, 24, 41].

The only available descriptions of this behaviour were derived for dimer-like crystals of α -perylene by the groups of WOLF [41] and LINDENBERG [23]. These simple kinetic pictures describe the so called E and Y -state emission for dimer-like crystals and were shown to be satisfactory in considerable detail. It should be mentioned explicitly that our system is distinctly different because MePTCDI forms a quasi-1D crystal which is not dimer-like, at least in the electronic ground state. The existence of a third emission band and the noticeable different temperature dependence of the spectral shape might give expression to the distinct differences of α -perylene [41]. A possible self-trapping process in MePTCDI might be distinctly different. Nevertheless, we want to introduce this model briefly in the following.

There is a commonly used nomenclature, introduced for the dimer-like molecular crystal of α -perylene: The luminescence from the lower self-trapped state, also named *solid-state excimer*, is called " E " luminescence. This E state has been dubbed the precursor state " Y ". The E state is derived from the symmetric pair state of the excited dimer. This is based on the assumption that the picture developed for excimers in the gas phase and in solution (see Sec. 2.2.1) will also work in solids. The reason appears to be that the mutual interaction of the molecules comprising the excimer pair is so strong that the influence of the host environment amounts only to a weak perturbation. Still, there are clear indications that the restrictive environment of a crystal lattice does modify excimer equilibrium configurations and may in some cases inhibit excimer formation. Figure 4.5 shows a rough scheme of the electronic levels for an isolated excimer and the modifications in a crystal following the ideas of LINDENBERG: The Y state is derived from the antisymmetric state of the excited dimer. For excimers in the gas phase and in solution this state is not stable, what is consistent with the experimental observations of only one luminescent transition. The different symmetry

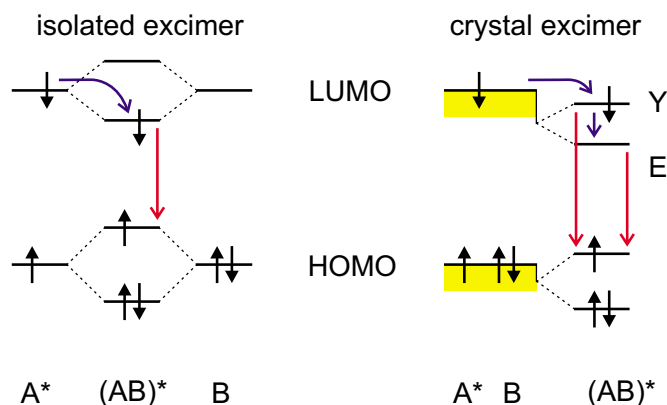


Figure 4.5: Scheme of the energetic levels of an isolated and a solid-state excimer. Molecule *A* is electronically excited to form an excimer $(AB)^*$ with the unexcited molecule *B*. The red downarrows depict the luminescent recombination. Left: In the gas phase and in solution only the lower electronic excited state of the excimer is energetically accessible. Right: In the crystal, electronic states are described by bands. Due to self-trapping the band-like description collapses for the involved molecules. The crystal environment is responsible for a shift of excimer states in a way that the upper electronic excited state of the excimer (*Y* state) is involved in the relaxation process. This results in the appearance of a second luminescent transition.

of the *E* and *Y* state would result in different selection rules. Therefore, the transition from the antisymmetric *Y* state to the symmetric ground state is largely allowed and the *E* to ground-state transition is largely forbidden.

The model is capable to explain the thermal changes of luminescence-decay times of α -perylene. However, it is more or less a phenomenological model and contains no satisfactory microscopic description of self-trapping. For MePTCDI, there are no detailed investigations to apply this model.

The model only allows to assign the two higher energetic luminescence peaks to emission from two different electronic excited states to a common ground state. The lowest energetic peak would need to be explained by any further effect not considered yet, e.g. by the vibronic progression of the internal effective mode in the electronic ground state. However, there is no requirement for the (questionable) assumption of a DAVYDOV-split doublet with different radiative lifetimes. Furthermore, one can nicely motivate the strong energetic shift between absorption and luminescence and their temperature dependence: The luminescence exhibits the characteristic excimer-type blueshift and broadening with increasing temperature. This behaviour can be understood in the simple excimer picture as introduced in Sec. 2.2.1. With increasing temperature, higher intermolecular vibrational states in the electronic excited state will be populated. The strong asymmetry of the potentials and the steep drop of the ground-state potential will directly lead to the observed shift and broadening of the emission peaks.

To summarize the discussion of the two proposed scenarios for relaxation and recombination, none of them is solely able to explain all main experimental features. Nevertheless, they seem to be reasonable. At this stage, we can not exclude one of them. To

take this fact into account, we will use the term *relaxed excited states* in the following, including both delocalized band states at $k = \pi$ and localized, self-trapped states. To clarify the nature of relaxed excited states, detailed investigation of temperature-dependent luminescence and/or different experimental approaches will have to be done (see Chap. 5).

4.1.3 Ultrafast Exciton Dynamics

In this section, we further discuss the exciton relaxation dynamics after optical excitation in MePTCDI. Our main goal is to time-resolve the relaxation of free excitons at $k = 0$ to the relaxed exciton states. From measurements of time-resolved luminescence, as presented in the previous section, we know a maximum value for this process of 10ps (determined by the time resolution of the streak-camera setup). It is not clear, whether relaxation from the initially excited states to the emitting states is a direct process - intermediate states might be involved in the relaxation process during the first 10ps. Due to the much higher time resolution of our TA setup, we will find that the relaxation to the emitting states is an ultrafast process on the sub-picosecond timescale.

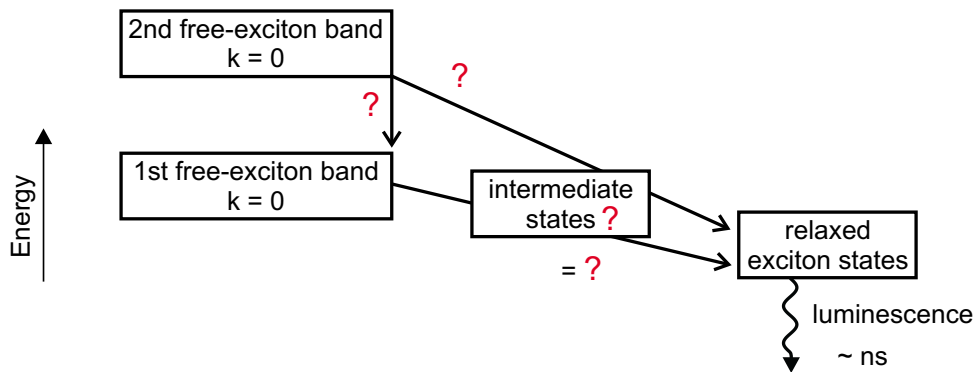


Figure 4.6: Schematic of exciton relaxation in the quasi-1D crystal of MePTCDI. Details are given in the text.

We have performed various TA measurements with different excitation conditions. All TA measurements were done at room temperature. As samples, we use polycrystalline thin (approx. 15nm) films of MePTCDI on a glass substrate. We use linearly polarized light pulses of about 25fs FWHM duration.

Relaxation out of the lowest exciton band (B1)

First, we present spectrally integrated TA measurements: The pump pulse is chosen to resonantly excite the lowest-energy exciton band B1 at around 2.1eV. The weak probe pulse is similar to the pump pulse in its spectral shape (pump-probe: B1-B1). The pulses are spectrally broad ($\approx 200\text{meV}$) to cover the whole width of this transition. The experimental conditions are given schematically in Fig. 4.7. Some typical experimental traces of time-resolved transmission change $\Delta T/T$ are given in Fig. 4.8. The dominant feature of these traces is a positive signal, decaying in the ps-time range. We show data, taken over the first 80ps, for three different excitation densities. Even if the

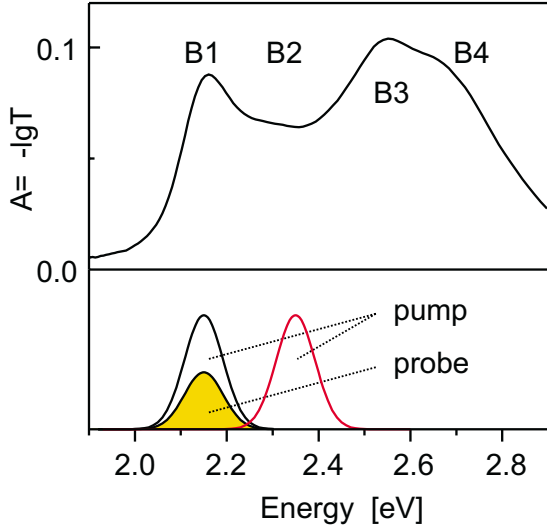


Figure 4.7: Top: Room-temperature absorbance spectrum of MePTCDI layer with indication of the four free-exciton bands. Bottom: Scheme of the excitation conditions for the two spectrally integrated TA measurements of this section. Either the pump pulses excite the lowest band *B1*, or the second band *B2*, whereas the probe pulses are always resonant to *B1*.

signal gets more noisy by reducing the pump power, there is a clear trend to slow down the observed decay. For reducing the pump power by a factor of 10, the decay constant of an exponential fit increases from 7.5ps to about 20ps.

Even though the complexity of physical phenomena taking place during the initial stages after excitation is apparent, the most important aspects of the exciton energy relaxation can be assigned: In comparable thin films of phthalocyanine, processes of inter- and intramolecular vibrational energy redistribution, exciton-exciton annihilation, and local heating were found to contribute to the relaxation dynamics [82, 83]. Local heating phenomena influence the signal on rather long time scale of more than 100ps, whereas for the case of high exciton density *exciton-exciton annihilation* is present only at short time delays. This process will lead to a non-exponential decay. The exciton density is usually described by the following bi-molecular rate equation:

$$\frac{dn}{dt} = -\gamma n - \alpha n^2 \quad (4.1)$$

where n represents the average exciton density, γ and α are the linear and nonlinear decay rates, respectively [83]. Finally, we interpret the signal as follows: The long-lived contribution (> 20 ps) is dominated by *nonlinear absorption* from the bleached ground state. The decrease of the decay constant from 20ps to about 7.5ps with increasing pump power can be mainly assigned to *exciton-exciton annihilation*. However, this effect is not relevant for relaxation we focus on. The relaxation of free excitons is a sub-ps process, as we will find out in the following. Therefore, we always fit the observed decays by assuming single exponential dependencies.

As $\Delta T/T$ is positive in Fig. 4.8, the signal is dominated by *nonlinear absorption* and/or *stimulated emission* (see Sec. 3.2.1). For not too high excitation densities, the given time constants in the ps-range of Fig. 4.8 are larger than the rise of luminescence (≤ 10 ps) as obtained from TR luminescence (see Sec. 4.1.1). Therefore, the TA signals are attributed to *nonlinear absorption*, and describe, depending on the influence of exciton-exciton annihilation, the recovery of the bleached ground state.

At time delays around $t = 0$, we observe an additional positive, but very short-lived contribution to the signal. It decays with a time constant of about 50fs (also shown

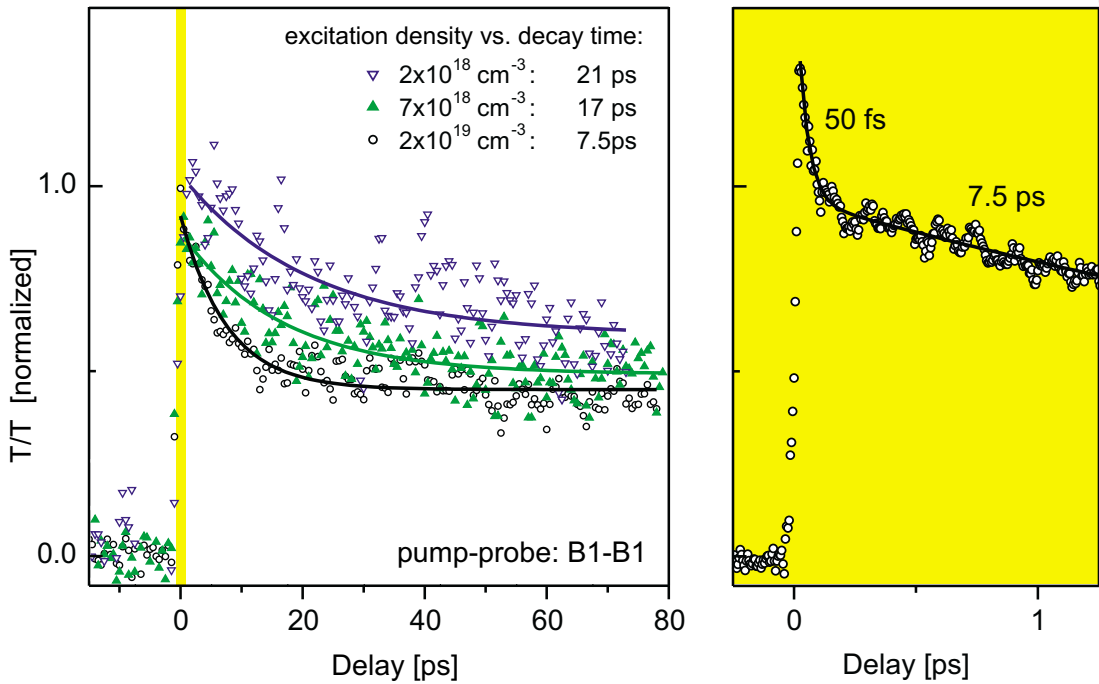


Figure 4.8: Spectral-integral transient absorption of MePTCDI at room temperature. The pump and probe pulses are chosen to be resonant to the lowest free-exciton transition (*B1*). Left: Normalized traces for various densities of optical excitation. The signals are fitted by a single exponential decay; the results are given as inset. Right: TA signal of the first picosecond at highest excitation density. The signal is fitted by a sum of two exponentially decaying contributions, the fast component has a time constant of about 50fs.

in Fig. 4.8).¹ The assignment of this fast decay is straightforward: It represents the disappearance of *stimulated emission* from the free-exciton states to the ground state. In other words, the optically-excited free-exciton states are depopulated within this time range. However, we have to assure that the very short lived contribution is not caused by the *coherent artifact* (reflecting pump-polarization coupling and perturbed polarization decay) [54, and references therein]: The time dependence of the signal can not be fitted properly by assuming a *coherent artifact*, what is mainly caused by the fact that the rise of this contribution is faster than its decay. In contrast, the fit of a sum of two exponential decays, representing two independent relaxation contributions, works very well.

Another information is provided by the relative intensity of the fast decaying contribution (*stimulated emission*) and the slow one (*nonlinear absorption*). In the case of a system without any *excited-state absorption*, at very early times both contributions to the signal should be of same strength. The trace in Fig. 4.8 reveals a ratio of about 1/2. This might be caused by the additional contribution of *excited-state absorption* to the signal and limited time resolution, which smears out the fast decaying contribution at very early times. Thus, we can not exclude *excited-state absorption* to contribute to the signal, but it is not the dominant contribution.

¹The modulations of the signal within the first picoseconds are no noise! They are attributed to coherent phonon wavepacket motion (see Sec. 4.3).

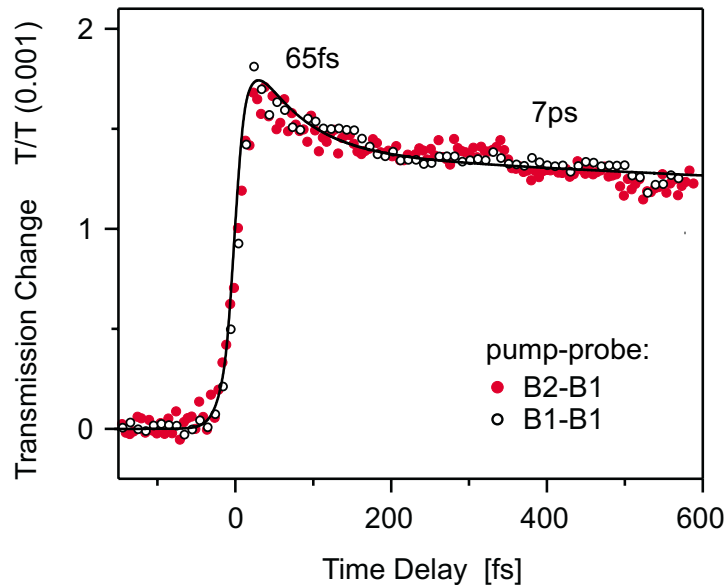


Figure 4.9: Spectral-integral transient absorption of MePTCDI at room temperature. Whereas the pump pulses excite either the lowest free-exciton band $B1$ (open circles) or the next higher band $B2$ (solid circles), the probe pulses are always chosen to be resonant to $B1$. Given are the experimental signals for the two different excitation conditions for the first 600fs. The fit reveals a sum of two exponentially decaying contributions with the given time constants.

Relaxation out of the second exciton band ($B2$)

In a further spectrally integrated TA experiment, we have modified the experimental conditions: Now, the pump pulse is resonant to the second free-exciton band ($B2$), and not to the lowest band ($B1$). The delayed probe pulse is still chosen to be resonant to the lowest band (pump-probe: $B2-B1$). A scheme of the excitation conditions is given in Fig. 4.7. By this experiment, we intend to monitor the excitons depopulating the states of the second band at $k = 0$. Additionally, we monitor states at $k = 0$ of the lowest band. If the free-exciton states at $k = 0$ of the lowest band are involved in the relaxation towards relaxed exciton states, their population and depopulation would show up in the signal. For comparison, we have performed again the measurement with excitation of $B1$ and probing of $B1$. The two experiments were performed under comparable conditions. In Figure 4.9, we give experimental traces for time delays around zero. The observed decay dynamics are very similar. For longer delays, i.e. for tens of picoseconds, the synchronism of the traces remains the same (not shown here). The signal quality of this measurement is not as good as for the (short delay) measurement shown in Fig. 4.8. Besides a lower signal-to-noise ratio, the time resolution is somewhat reduced and/or the influence of chirp seems to be increased. Therefore, the fitted time constants for the fast decay of *stimulated emission* are somewhat larger. This also explains the reduced intensity ratio of the fast decaying contribution of *stimulated emission* to the slow one of *nonlinear absorption* of approx. 1/3.

The $B1-B1$ experiment (solid circles) is a repetition of the previous experiment of this section, monitoring the relaxation out of the $k = 0$ states of the lowest band. The signal mainly stems from *nonlinear absorption* with an additional contribution

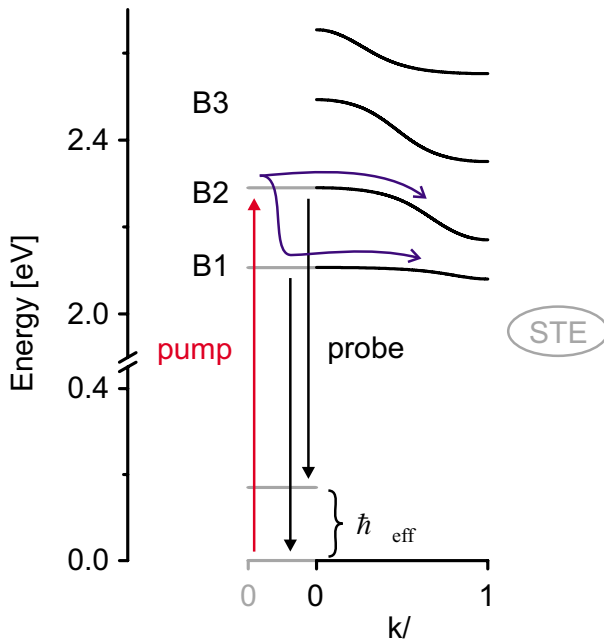


Figure 4.10: Schematic of possible transitions monitored by probe pulses for very short delays, while $B2$ -band states at $k = 0$ are depopulated. For later times, either band states at $k = \pi$, or even to self-trapped exciton states (STE) are populated.

by *stimulated emission* for time delays around zero. Thus, it is not astonishing to find nice agreement of the two experimental traces for large time delays, because then, *nonlinear absorption* from the common bleached ground state dominates the signals. In other words, for large time delays, we only monitor the bleached ground state and its repopulation, which is expected to be the same for the two experiments. The remarks concerning various processes contributing to *nonlinear absorption*, as discussed for the previous experiment, will also hold for this one.

However, our focus is on small time delays. There, the observed coincidence is rather astonishing. Thus, also the contribution from *stimulated emission* is comparable for both measurements. There are two possible interpretations, as shown in Fig. 4.10: First, the probe pulse monitors *stimulated emission* from band $B1$ to the relaxed ground state. And second, the probe pulse might monitor *stimulated emission* from band $B2$ to states of the non-relaxed ground state. In the following, we will argue that the second process is likely to be responsible for the signal.

As a consequence of the first scenario, the depopulation dynamics of the lowest band at $k = 0$ would need to be very similar for the two different excitation conditions $B1$ - $B1$ and $B2$ - $B1$. As we observe no lower rise for the *stimulated-emission* contribution, there must a dominant and quasi-instantaneous relaxation from the initially excited states of the second band to the states of the lowest band at $k = 0$. Quasi-instantaneous means in that context, considerably faster than the time resolution of the experiment of about 25fs. Having in mind that depopulation of the states at $k = 0$ of the lowest band has a time constant of about 50fs, this scenario seems rather unlikely.

As a consequence of the second scenario, the depopulation dynamics of the lowest band $B1$ would need to be very similar to the depopulation dynamics of the second band $B2$. Thus, the observed contribution of *stimulated emission* is attributed to the depopulation of the second band at $k = 0$. This explanation requires no quasi-instantaneous relaxation (from $B2$ to $B1$) and no qualitative differences for the depopulation of the different bands at $k = 0$. As the two bands belong to the same electronic transition,

”only” differing in their phononic states, similar depopulation dynamics of $B1$ and $B2$ seem to be reasonable.

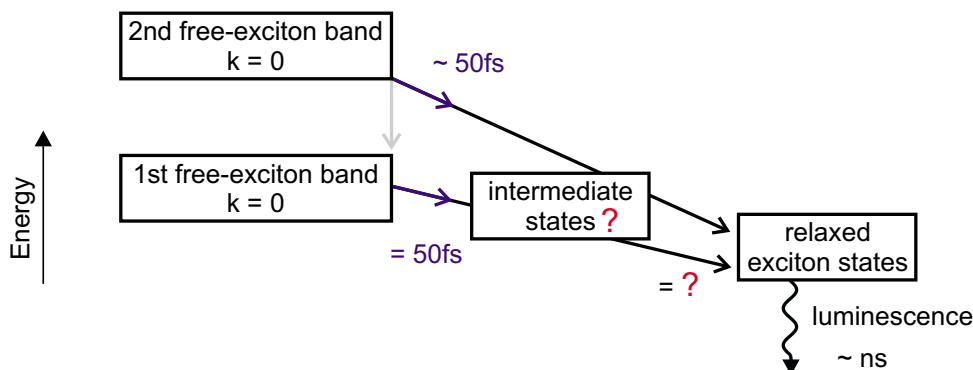


Figure 4.11: Schematic of exciton relaxation in the quasi-1D crystal of MePTCDI. Details are given in the text.

To summarize the gained results from the spectral integral TA measurements, we have found an ultrafast depopulation of the initially excited free-exciton states with a time constant of 50fs. The free excitons of second exciton band are likely to relax by intra-band relaxation or/and exciton self-trapping, and not via free-exciton states at $k = 0$ of the lowest band.

The luminescent, relaxed exciton states are populated within 10ps after excitation as we know from time-resolved luminescence. As we did not time-resolve this process, it is probably much faster than 10ps. However, intermediate relaxation steps between the ultrafast depopulation of the initially excited states and the population of the emitting states might be possible.

Relaxation into the emitting states

To get further insight in the excited state dynamics after depopulating the initially excited states, we have performed *TA* experiments with the probe pulse shifted to lower energies. Our objective is to suppress the contribution of *nonlinear absorption* to the signal, which monitors the bleached ground state. Additionally, we spectrally resolve the probe pulses after the interaction with the sample. The spectral-cut width is of about 4nm (15meV). These experiments allow to monitor the relaxed exciton states and any optically active intermediate state by *excited-state absorption* and, perhaps, *stimulated emission* exclusively. Thus, we are able to probe any relaxation process faster than the rise of luminescence from relaxed exciton states.

Two typical traces over tens of ps are shown in Fig. 4.12. Note that we observe a negative TA signal for probe energies below the optical band gap, i.e. the transmission of the perturbed sample is reduced in the chosen spectral windows. This is caused by transitions of the excited-state population to higher states (*excited-state absorption*). The observed signals can nicely be fitted by a single exponential decay of a time constant of about 19ps. As we know from time-resolved luminescence, the relaxation of free excitons to the luminescent, relaxed excited states takes less than 10ps, and is probably much faster. Thus, we find a rise of luminescence ($< 10ps$) which is faster than the

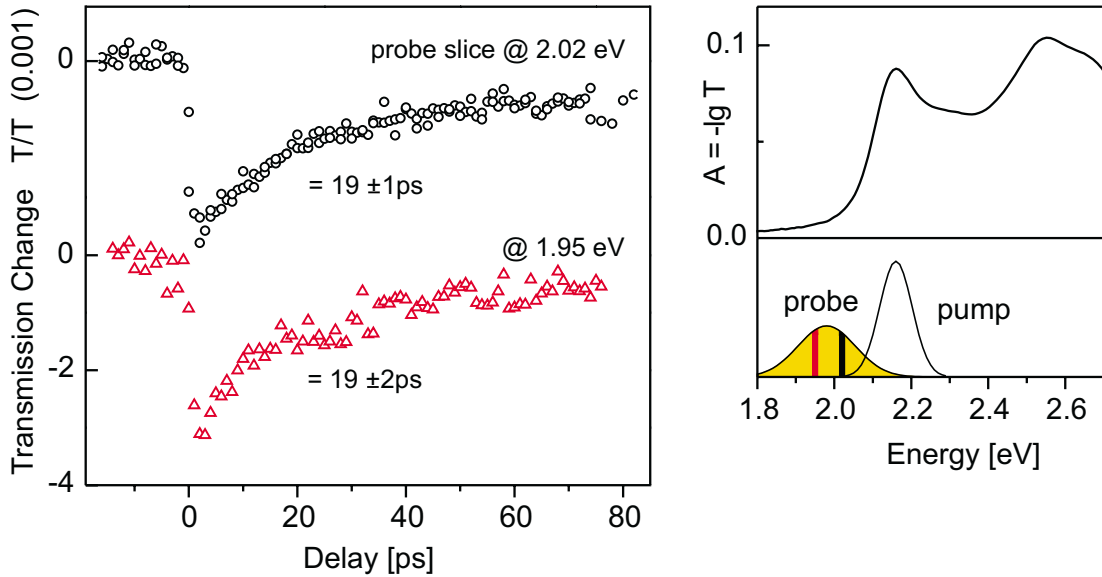


Figure 4.12: Spectrally resolved two-color transient absorption of MePTCDI at room temperature. The spectral selection of the probe pulse is done after the interaction with the sample. Left: Experimental results for two spectral positions. The signals are fitted by a single exponential decay. Right: Scheme of excitation conditions with spectrum of absorbance of MePTCDI at room temperature. The spectral cuts of the probe pulses are given schematically.

decay of the *excited-state absorption* (19ps) found in the spectrally integrated TA measurements. From this, we conclude that the *excited-state absorption*, observed between 1.95eV and 2.02eV, stems from the relaxed exciton states, and not from any intermediate state.

We will discuss now, on which time scale these relaxed exciton states are populated. For this, we have performed spectrally resolved TA measurements, similar to the previous experiments shown in Fig. 4.12 for the ps-time range, but now concentrating on the signal change at very early times.

Before discussing the experimental results, some remarks to this experiment shall be given. These measurements, covering a wide frequency range and providing a very high temporal resolution, are most demanding. The use of ultrabroad probe pulses requires a good control and/or correction of the chirp. We used a fused-silica prism compressor for zeroing the linear chirp. However, the remaining chirp of higher orders can not be neglected for measurements in the sub-ps range. Therefore, we always measure the spectral phase by frequency gating (see Sec. 3.1.2). In Figure 3.5, we give a typical example for the remaining quadratic chirp of our setup. All experimental traces of Fig. 4.13 are corrected with respect to the point of zero-delay. However, the chirp, which can not be compensated by the prism compressor, is present in the measurement and makes the interpretation of the signal more complicated. The remaining chirp and therefore the time-resolution of this measurement is not constant for the various slices of the probe pulse. This will sensitively affect the signal for early times. For instance the phononic modulations at around zero delay are very sensitive to chirp. Unfortunately, this is also the time window we are interested in. Nevertheless, the data are of high quality and useful for further interpretation.

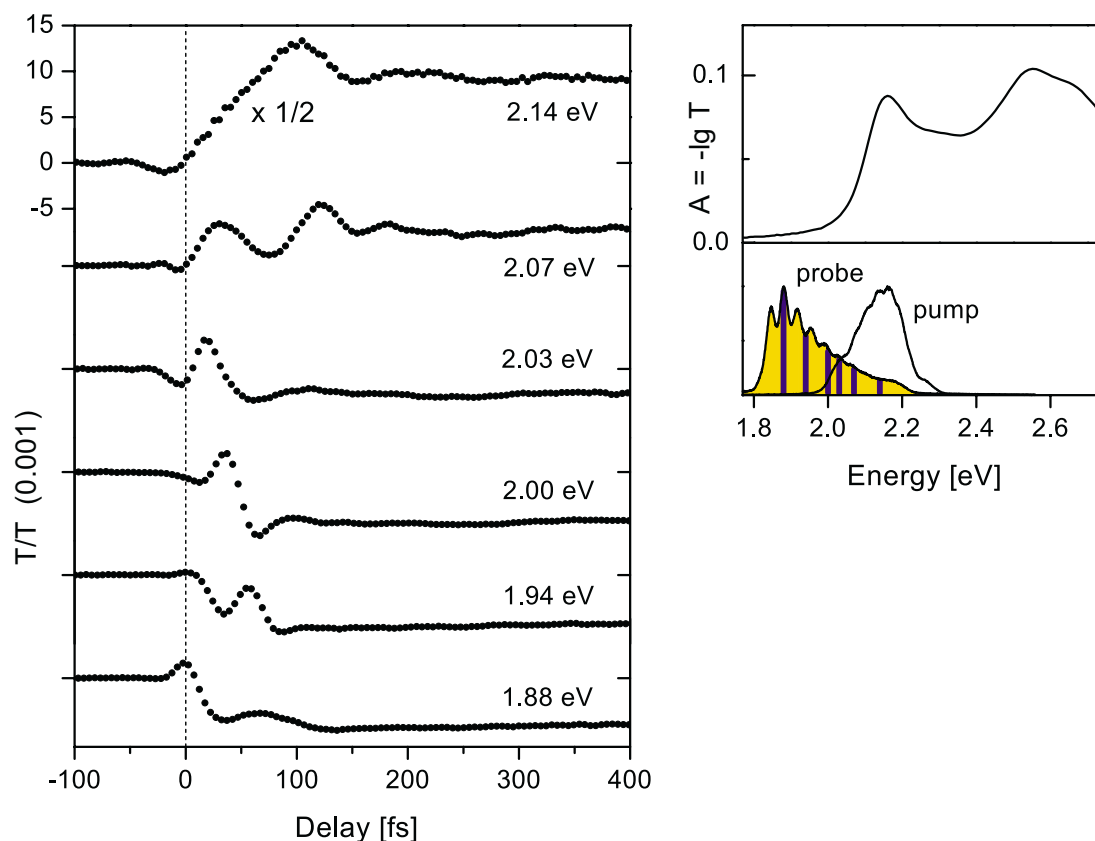


Figure 4.13: Spectrally resolved two-color transient absorption of MePTCDI at room temperature. The spectral selection of the probe pulse is done after the interaction with the sample. Left: Experimental results for six spectral positions. Right: Excitation conditions with absorbance of the MePTCDI sample at room temperature. The spectra of pump and the much weaker probe are normalized for visualization. The spectral cuts of the probe pulses are given schematically.

The experimental signal for six spectral "slices" of a 100-nm broad probe continuum are given in Fig. 4.13. The most obvious feature is the change of the signal from positive values at high probe energies to negative values for lower energies. This behaviour was already discussed in the previous TA experiments of this section. If the probe pulse is resonant to the lowest optical transition, the signal is dominated by *nonlinear absorption* from the bleached ground state ($\Delta T/T$ positive). At early times, *stimulated emission* will also contribute to the signal with a positive sign. In the spectrally integrated TA measurements, this contribution was nicely observed to decay with a time constant of about 50fs. We can not clearly observe *stimulated emission* in the trace with the probe sliced at 2.14eV. This is because this contribution interferes with the additional phononic modulation, which is present for all probe slices. For all traces of lower energy, *stimulated emission* is not expected to contribute to the signal. With decreasing energy the influence of *nonlinear absorption* from bleached ground state is suppressed and the signal is dominated by *excited-state absorption*. As in the measurements shown in Fig. 4.12, we find a negative transmission change for probe energies between 1.88eV and 2.03eV, which is due to *excited-state absorption* from the relaxed exciton states. Here, we observe that the relaxation from initially-excited free excitons

to relaxed exciton states is an ultrafast process with an overall time constant of about 50fs. From Figure 4.13 one might even extract somewhat smaller values. However, this is within the experimental errors, which are mainly due to the remaining chirp and the various omnipresent phononic wave-packets, which are superimposed on the signal at early times.

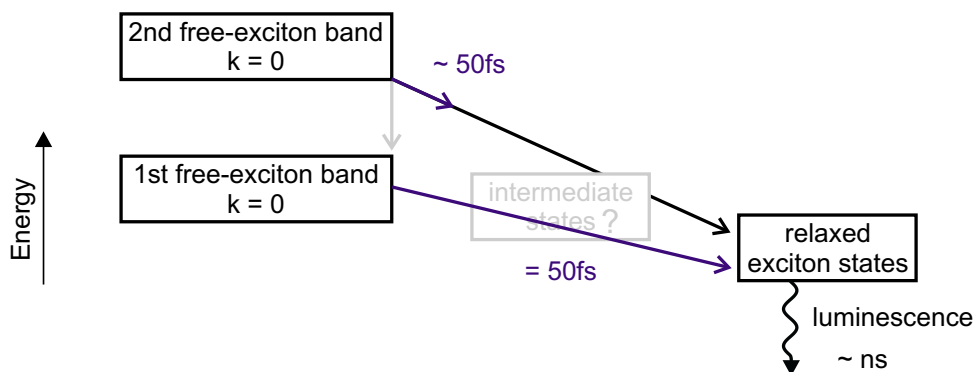


Figure 4.14: Schematic of exciton relaxation in the quasi-1D crystal of MePTCDI. Details are given in the text.

To summarize the gained results concerning exciton relaxation, we have found an ultrafast depopulation of the initially excited free-exciton states of two lowest bands with a time constant of about 50fs. The free excitons of the second exciton band do not relax via states at $k = 0$ of the lowest band. In the spectrally resolved TA measurements, we did not observe any (optically active) state which acts as an intermediate in the relaxation from optically excited states of the lowest band towards the luminescent, relaxed exciton states.

4.2 Dephasing of Free Exciton Transitions

By optical excitation of an electronic transition, a polarization is induced. To visualize the process of polarization dephasing, we imagine the macroscopic system to be a large assembly of microscopic transitions. Now we coherently induce a polarization by a short laser pulse, which is resonant to the electronic transitions. The microscopic polarization of all members of the ensemble starts with the same phase, resulting in a macroscopic polarization. As the phase depends sensitively on the interactions of the excited system with its surroundings, it gives insight in the interaction mechanisms on the microscopic scale. Therefore, the transitions will lose their initial phase relation. The macroscopic polarization vanishes due to destructive interference. Measuring the time constant of dephasing allows to distinguish between *homogeneous* and *inhomogeneous* broadening of transitions (see Sec. 3.2.2). This is an important information for the general understanding of OMCs, as well as from the viewpoint of technological application.

Dephasing of electronic transitions for molecules in solution were studied by *hole-burning spectroscopy* and *Four-Wave Mixing* (FWM). The dephasing time T_2 of the $S_0 - S_1$ transition was measured to be in the range of 10fs to 60fs for dyes like Nile blue or Malachite green [84, 85]. The dephasing times were determined on the assump-

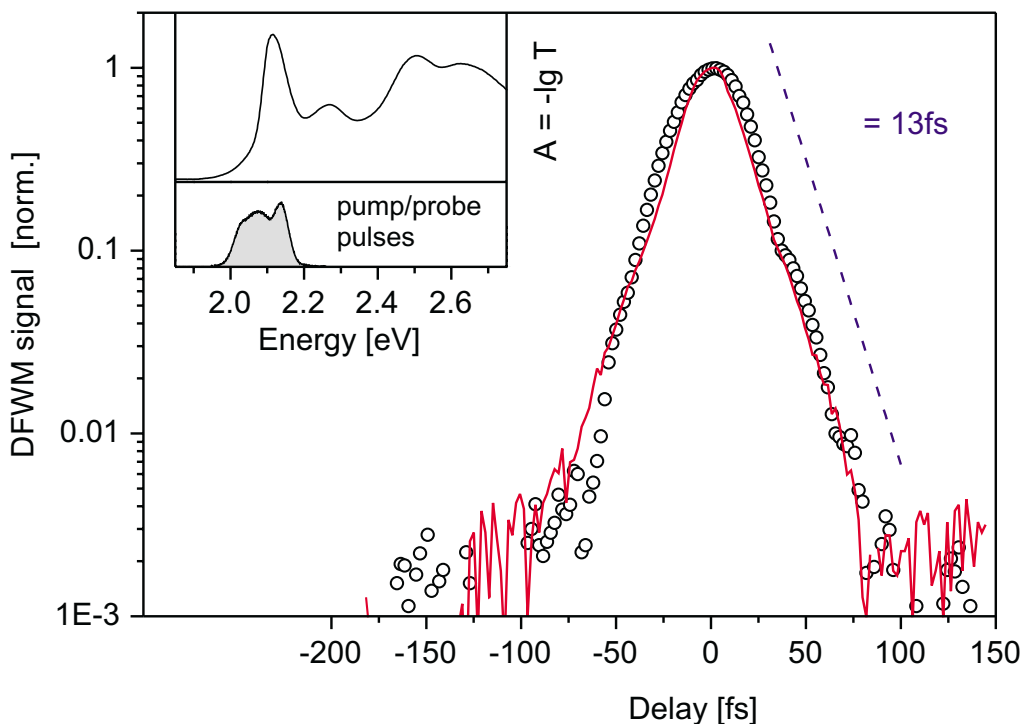


Figure 4.15: Degenerate four-wave-mixing signal (hollow circles) and auto correlation trace (solid line). Additionally shown is a fit of a 13-fs exponential decay (dashed line). Inset: Laser spectrum and absorbance of MePTCDI at 4K.

tion of either *homogeneous*, *inhomogeneous* broadening or non-MARKOVIAN relaxation. The non-MARKOV model describes the intermediate regime between the extreme cases of *homogeneous* and *inhomogeneous* broadening and results in a non-exponential polarization decay [86, 87]. Electronic dephasing in large molecules is, in the simplest picture, discussed in terms of the coherence loss of the transition dipole moment of a two-level system. Clearly, large molecules are multilevel systems, if one considers the vibrational sublevels of the FRANCK-CONDON active vibrations explicitly. Therefore, the *homogeneous* broadening will play an important role. However, both the manifold vibrational properties of the molecules itself and the coupling to the solvent will be crucial for the fast dephasing [88]. To the best of our knowledge, there is no complete understanding of dephasing in organic systems.

There are also a few measurements on organic condensed matter, i.e. on dyes in a polymer host or on polymers itself [89, 90]. The observed dephasing times are in the same range as for the molecules in solution. To our knowledge, there are no reports about measurements on OMCs so far.

To investigate the coherent regime of free-exciton transitions we have applied self-diffracted *Degenerate Four Wave Mixing* (DFWM). The experiments were finally not successful in the sense of obtaining the dephasing-time constant T_2 . Nevertheless, we can give some useful estimates about the dephasing process.

We use linearly polarized light pulses with about 25fs FWHM duration for the experiments of two-pulse DFWM with spectral integral detection. The spectrum of the

pulses, centered around 2.1eV, is shown as inset in Fig. 4.15. The photon energy is chosen to excite the lowest energy non-lattice relaxed exciton band - which has a weak negative dispersion - at $k = 0$. The pulses stem from white-light generation (WLG) and subsequent amplification by the NOPA, as described in Sec. 3.1.3. Afterwards, the pulses are split into the two pulse trains \mathbf{k}_1 and \mathbf{k}_2 of similar intensity by a beam splitter. To select the pump spectrum, we use a fused-silica prism dispersive delay line. The experimental auto-correlation width, measured with a 20 μ m BBO crystal at the position of the sample, was 23fs over the detected energy range. The DFWM intensity was detected using a PMT and a Lock-In amplifier. We use excitation densities of about 10^{18}cm^{-3} . As samples, we use polycrystalline thin films (approx. 15nm) of MePTCDI on glass substrate. The sample was kept at 4K throughout all optical measurements to suppress scattering by phonons.

The measured polarization decay is given as hollow circles in Fig. 4.15. The experimental curve is symmetric around zero delay, and the observed decay corresponds one to one to the autocorrelation (AC) of the laser pulses. The AC determines the time resolution of the experiment. However, one has to distinguish between various measures of time resolution: The AC of sech^2 -pulses of 23fs FWHM reveals an exponential rise and decay of about 13fs. In general, the DFWM signal represents the convolution of the pulses AC and the dephasing of the transition. Therefore, in our case, the detected polarization response does not represent the free induction decay rather than a polarization fully driven by the exciting pulses. Following (3.26), the dephasing of the lowest exciton transition under the experimental conditions is faster than $2 \times 13\text{fs} = 26\text{fs}$ for dominant *homogeneous* broadening, or $4 \times 13\text{fs} = 52\text{fs}$ in the case of *inhomogeneous* broadening.

The natural line width of a transition is directly connected to its dephasing. In the classical model of a damped harmonic oscillator, a *homogeneously* broadened transition is described by the LORENTZIAN line shape:

$$I(\omega) = \frac{\Gamma_{\text{hom}}/2\pi\hbar}{(\omega - \omega_0)^2 + (\Gamma_{\text{hom}}/2\hbar)^2} \quad (4.2)$$

where Γ_{hom} is the FWHM of the absorbance peak in linear absorption and ω_0 is the resonance frequency of the transition. The spectral profile expresses the polarization properties of the transition in frequency domain. The polarization for the *homogeneously* broadened transition decays exponentially with a time constant T_2 , which is given by:

$$T_2 = \frac{2\hbar}{\Gamma_{\text{hom}}} \quad (4.3)$$

In real systems, additional *inhomogeneous* broadening of the transition has to be considered. Thus, the line shape is described by a convolution of the LORENTZIAN function (4.2) with a distribution, describing the inhomogeneous broadening (usually assuming a GAUSSIAN shape). The total line width of the transition simply results to

$$\Gamma_{\text{total}} = \Gamma_{\text{hom}} + \Gamma_{\text{inhom}} \quad (4.4)$$

where Γ_{inhom} is the FWHM of *inhomogeneous* broadening. From low-temperature lin-

ear absorption, we can estimate a total line width for the lowest energetic exciton transition of $\Gamma_{\text{total}} \approx 80\text{meV}$ (see, e.g. Fig. 2.11). Assuming the absence of any *inhomogeneous* broadening, we can use (4.3), which results in an expected dephasing time of $\approx 17\text{fs}$. For the realistic assumption of both *homogeneous* and *inhomogeneous* broadening, this value is the lowest limit for dephasing time, i.e. $T_2 \geq 17\text{fs}$. Following the argumentation up to this point, one might estimate the dephasing time in the range of $17\text{fs} \leq T_2 \leq 52\text{fs}$. However, the situation is more complicated. The observation of the polarization decay in the DFWM experiment might be influenced by *excitation induced dephasing*. Additionally, the role of inhomogeneities for MePTCDI is not yet discussed. In the following, we will give relevant arguments and limitations, which are necessary to further classify the found estimation for T_2 .

- Inhomogeneous Broadening

For an *inhomogeneously* broadened transition, the total line width from absorption is not connected to the dephasing time T_2 anymore. Usually T_2 will be much larger than one might estimate from line width in the *homogeneous* limit. Therefore, we could only extract a lower limit for dephasing time from absorption. For our system, the assumption of the absence of any inhomogeneous broadening of the transitions is not justified. We do not know, whether the lowest optical transitions of the polycrystalline thin layers are dominated by inhomogeneous broadening. They are definitely affected by inhomogeneities, as we know from the comparison with single crystals, e.g. in absorption (total line width) and TR luminescence (line width and decay; see Sec. 4.1.1). A layer of MePTCDI of 15nm thickness corresponds to a maximum of 40 molecules stacking on top of each other. From atomic force microscopy (AFM) and X-ray diffraction, we estimate the average size of the polycrystallites within the layer to less than 100nm [10, 11]. As an example, for a given crystallite of a size of $50 \times 50 \times 15\text{nm}$, the ratio of surface to non-surface molecules is 1/6. Excitonic surface transitions of anthracene are estimated to show energetic shifts relative to the bulk modes of about $+25\text{meV}$ [91], showing that surface modes can not be neglected. On the other hand, *homogeneous* broadening is supposed play an important role in OMCs. Due to the rich variety of vibrational degrees of freedom, OMCs have to be considered as multilevel systems. The strong coupling of vibrational modes to electronic transitions in MePTCDI (see Sec. 2.1.1) might be responsible for rather large *homogeneous* broadening.

In summary, we can not exclude a dominant *inhomogeneous* broadening of the transitions, even though we expect a rather large *homogeneous* line width. However, from the conclusion that neither *inhomogeneous* nor *homogeneous* broadening can be neglected, we slightly modify the limits of our estimate of the dephasing time to $17\text{fs} < T_2 < 52\text{fs}$.

- Excitation Induced Dephasing

At low excitation densities, as realized in the linear absorption measurements (see, e.g. Fig. 2.11), the photo-excited states can be well described by isolated excitons. With increasing intensity, we reach a regime, where excitons are still good quasi particles, but their density n is so high that they start to interact with each other. Elastic and inelastic scattering processes between the excitons will significantly

change the dephasing rate ($T_2 = T_2(n)$). Thus, the obtained decay rates do not represent the free induction decay anymore. This is the regime of *excitation induced dephasing* [76, 73, 92].² A critical parameter to reach this scenario, besides the excitation density, is the exciton-BOHR radius.³ In the following, we try to compare our system with GaAs, which was extensively investigated by KUHLE et al. [92].

In GaAs, the excitonic binding energy is $E_{exc} \approx 4\text{meV}$. The excitons are of WANNIER-MOTT type with the BOHR diameter of $2a_B = 27\text{nm}$. In DFWM experiments, the dephasing time starts to drop at an exciton density of $2 \times 10^{14}\text{cm}^{-3}$, what corresponds to a mean exciton separation of 170nm. That means, a minimum separation of at least 6 times the exciton-BOHR diameter is necessary to reach the regime of *excitation induced dephasing*. However, reduction of dimensionality from bulk GaAs to 2D-quantum wells (GaAs/ $\text{Al}_x\text{Ga}_{1-x}\text{As}$) will increase this ratio by a factor of about 2 [93]. It should be kept in mind that MePTCDI is a quasi-1D system.

The excitonic binding energy for OMCs is of the order of $E_{exc} \approx 100\text{meV}$. The FRENKEL exciton is usually assumed to be localized on a single molecule. However, for MePTCDI we know that the lowest energetic excitations are strongly mixed FRENKEL-Charge Transfer excitons [32]. In the direction of close stacking, the BOHR diameter is about one or two times the distance between the molecular planes (3.40\AA). We estimate the BOHR diameter at $\approx 0.5\text{nm}$ within the 1D stacks.

In our experiment, μJ -pulses are focused to spot diameters of about $30\mu\text{m}$ on the 15nm thick sample, which has an optical density of 0.1. This results in a photon density of about 10^{13}cm^{-2} , creating exciton densities $n \approx 2 \times 10^{18}\text{cm}^{-3}$. Thus, the mean exciton separation is of about 8nm. This corresponds to 16 times the exciton BOHR diameter in the direction of the 1D stacks of MePTCDI, whereas in the other crystal directions this corresponds to only 5 times the molecular spacing. As we should concentrate on the 1D direction of strong coupling, we have to compare the ratio of 16 for the 1D system of MePTCDI with the ratio of 6 for the 3D system of GaAs for a lower threshold for *excitation induced dephasing*. This sounds not critical, but the differences of the systems concerning the excitonic properties and dimensionality should be kept in mind. Thus, we finally can not exclude *excitation induced dephasing* to be responsible for the very fast dephasing.

In summary, we estimate the dephasing time for the lowest excitonic transition from linear absorption to $T_2(n \approx 0) > 17\text{fs}$. From DFWM experiments, we can give an upper limit for the dephasing time $T_2(n \approx 2 \times 10^{18}\text{cm}^{-3}) < 52\text{fs}$. Assuming that an exciton density of $n \approx 2 \times 10^{18}\text{cm}^{-3}$ does not cause *excitation-induced dephasing*, the found dephasing time will represent the free induction decay, i.e. $T_2(n = 0) < 52\text{fs}$. However, we can not safely exclude *excitation induced dephasing* to be responsible for the very fast dephasing. The found limits for T_2 correspond to a homogeneous line width $80\text{meV} > \Gamma_{\text{hom}} > 27\text{meV}$.

²Here, the expression *excitation induced dephasing* is used under the assumption that it includes all the many-particle interaction-induced effects on the dephasing time. In the literature this term has been used differently from various authors.

³The lifetime of the excitons, as an additional parameter, should not play a role in correlation experiments at low repetition rates.

4.3 Vibronic and Phononic Wave Packets

The time-resolved measurements reported here are carried out using TA spectroscopy, similar to the experiments presented in Sec. 4.1.3. However, the focus is now on the vibrational properties of MePTCDI. We have directly time-resolved the dynamics of phononic wave packets in thin films of MePTCDI. We observe both coherent oscillations of intramolecular vibrational wavepackets (internal phonons) and, for the first time in a quasi-1D organic system, lower energetic modulations, which are related to coherent lattice phonons (external phonons).

As samples, we use polycrystalline thin (approx. 15nm) films of MePTCDI on a glass substrate. We use linearly polarized light pulses with about 25fs FWHM duration, with a photon energy chosen to excite the lowest energy non-lattice relaxed exciton band at $k = 0$. The pump pulse spectrum, centered around 2.15eV, is shown in Fig. 4.16. The pump pulses are generated by a NOPA, as described in Sec. 3.1.3, pumped by an amplified Ti:sapphire laser system running at a repetition rate of 1kHz. To select the pump spectrum, we use a slit in the fused silica prism dispersive delay line (see Sec. 3.1.2). TA measurements were carried out using collinear polarized probe pulses from a broadband femtosecond continuum, generated in a 1mm-thick sapphire plate. The probe spectrum was selected to monitor the dynamics at the lowest energy exciton band (see Fig. 4.16). The experimental cross-correlation width, measured with a 20 μ m BBO crystal at the position of the sample, was ~ 35 fs over the detected energy range. For the pump-probe measurements, the intensities of the transmitted probe and a reference beam were balanced and detected using a pair of photodiodes and a lock-in amplifier. We use excitation densities of about 10^{18}cm^{-3} ; all measurements are performed at room temperature.

By the pump pulse, phonon modes strongly coupled to the excitonic transition are excited by *Resonant Stimulated-Impulsive Raman Scattering* (RSIRS) [70]. The RSIRS excitation creates phonon wave packets that are a coherent superposition of the phonon eigenstates. These non-stationary phonon wave packets, which can be formed on both the ground and the excited potential energy surfaces, oscillate at the characteristic phonon frequencies of the material and are observed as a modulation of the differential transmission signal as a function of delay time (see Sec. 3.2.1). Only

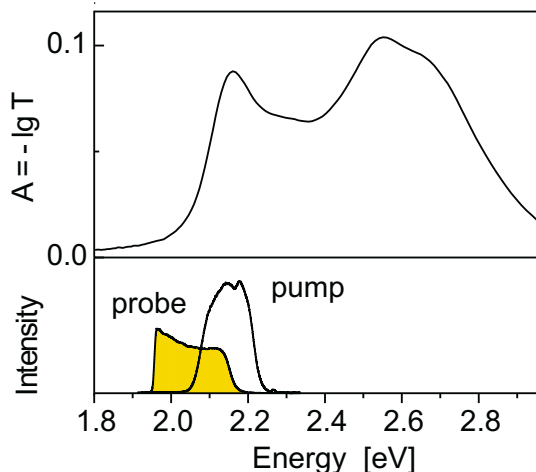


Figure 4.16: Top: Room-temperature absorbance spectrum of MePTCDI layer. Bottom: Spectral profiles of pump and probe pulses. The intensity ratio of the pulses pump/probe is at least 10/1.

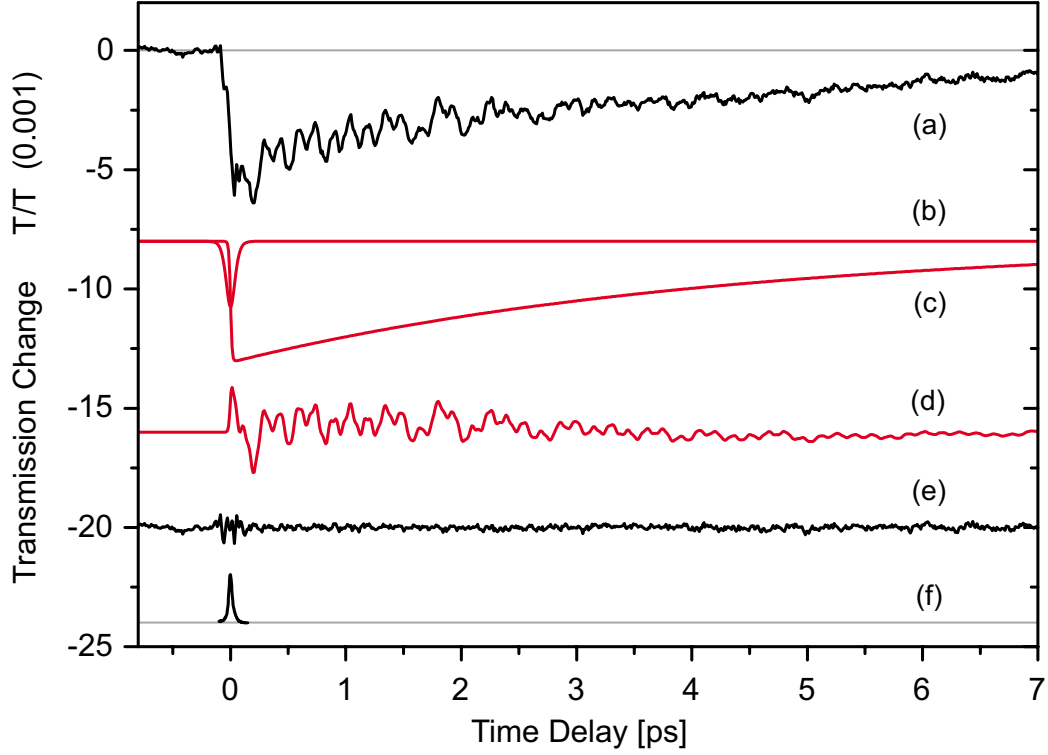


Figure 4.17: Time-resolved differential transmission of MePTCDI layer following excitation with 25fs pump pulses. From top to bottom: Experimental signal (a), fit of the short-lived contribution around zero delay (b), fit of the exponentially decaying contribution (c), fit of the oscillating contribution (d), the residuum of the fit (e), and the experimental cross-correlation (f). The curves are shifted for clarity.

those phonon modes will contribute to the signal by a time-dependent oscillation of transmission, the characteristic period of which is long compared to the laser pulses. The pulse duration of 25fs FWHM restricts the time resolution of the experiment and thus the detectable phononic energetic range to less than 700cm^{-1} ($= 87\text{meV}$).

The time-resolved transmission change following impulsive excitation of the lowest-energy exciton band is given as the upper graph (a) in Fig. 4.17. The most conspicuous feature is a strong modulation due to phonon wavepacket oscillations [94]. In addition, processes like the relaxation of exciton populations and vibrational thermalization contribute to the signal. For a quantitative oscillation data analysis, we fit (using a nonlinear least-squares MARQUARDT-LEVENBERG algorithm) the entire relevant delay time t range between pump and probe pulse with the following expression for the transmission change:

$$\begin{aligned} \frac{\Delta T(t)}{T} &= a S(t/\tau_p) e^{-t/\tau_{\text{decay}}} + b \text{sech}^2(t/\tau_{\text{peak}}) \\ &+ S(t/\tau_p) \sum_i c_i \cos(\omega_i t + \phi_i) e^{-t/\tau_i}, \end{aligned} \quad (4.5)$$

where $S(t) = [1 + \tanh(t/\tau_p)]/2$ is a smoothed step function, corresponding to the time

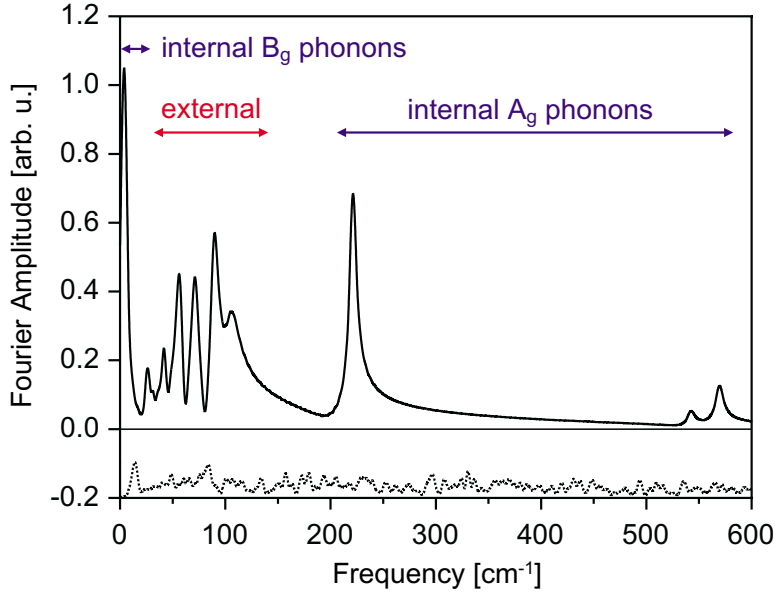


Figure 4.18: Absolute of the FOURIER amplitude spectrum of the oscillating part of the experimental data. Solid: FOURIER amplitude of the fitted oscillatory part, as derived from the least-square fitting in real time. The three highest energetic modes stem from intramolecular modes and the six modes between 33 and 105 cm^{-1} from external librational phonon modes. The residuum, given as dotted line (shifted for clarity to -0.2), shows the quality of the fit.

integral over a pump pulse intensity $I_{\text{pump}}(t) = \text{sech}^2(t/\tau_p)$. For simplicity, we use both for the exponentially decaying contribution and the oscillatory part the same smoothed step function $S(t/\tau_p)$.

The first part is the time integral over a pump pulse intensity $I_{\text{pump}}(t) = \text{sech}^2(t/\tau_p)$ multiplied by an exponential decay, given as graph (c) in Fig. 4.17. This term corresponds to *excited-state absorption* as dominant contribution, as well as to a weaker contribution from *nonlinear absorption*. Thus, it mainly reflects the depopulation processes of the relaxed exciton states, e.g. the recombination of the excitons. We find a time constant of $\tau_{\text{decay}} = 4.2 \pm 0.4\text{ps}$. The second part is a short-lived contribution localized around zero delay which is caused by *excited-state absorption*, given as graph (b) in Fig. 4.17. It reflects the ultrafast depopulation of optically excited states at $k = 0$ (see Sec. 4.1.3). For this contribution, we find a time constant $\tau_{\text{peak}} = 51\text{fs}$. The third part is a sum of decaying oscillations switched on at zero delay, using for simplicity the same smoothed step function $\int dt I_{\text{pump}}(t)$ as for the exponentially decaying contribution. This contribution is given as graph (d) in Fig. 4.17. The fit results for the pulse profile agree well with the experimentally determined FWHM of 25fs.

The results of the fit related to the oscillating contributions are shown in Table 4.2. The amplitude FOURIER spectrum of the oscillating part is shown in Fig. 4.18. The given residuum demonstrates the good quality of the fit. Analysis of the phase information, given in last row of Tab. 4.2, requires precise knowledge about the chirp of the used laser pulses and, at least, some more information about the involved potential surfaces. This is beyond the scope of this work, for further discussion, see Sec. 4.3.1).

In the following, we will show that the three highest-energy oscillations are due to a

wavepacket of internal phonons of A_g symmetry, the six oscillations following towards lower energy can be assigned to external phonons, and the two lowest oscillations are interpreted as due to internal B_g phonons. For a general introduction of the phononic properties of OMCs, see Sec. 2.4.

1.) Internal A_g phonons

To interpret the FOURIER spectrum, R. SCHOLZ calculated the internal phonon frequencies for an isolated MePTCDI molecule in the electronic ground state [97]. The crystal-formation might cause additional shifting of the vibrational frequencies and splittings of degenerate modes due to static field effects as well as changes in the RAMAN selection rules. In addition, DAVYDOV splitting is expected for crystals with more than one molecule per unit cell, as it is the case for MePTCDI. Nevertheless, in molecular crystals as MePTCDI, where covalent intramolecular forces dominate over the intermolecular VAN DER WAALS forces, shifts and splittings of internal A_g phonons are expected to be small compared to their absolute values [98].

The calculation of internal phonon frequencies is done using *density-functional tight-binding* (DFTB) methods [99] already tested for the similar perylene derivative PTCDA [17]. From group-theoretical arguments, only totally symmetric (A_g) vibrations can be elongated due to the dipole transitions from the electronic *highest occupied molecular orbital* (HOMO) to the *lowest unoccupied molecular orbital* (LUMO), and the

Table 4.2: Results of non-linear least-squares fit to the oscillating part of differential transmission measurements in Fig. 4.17. First column: fitted oscillation frequencies, second column: *resonant RAMAN scattering* (RRS) data [96], third column: mode frequencies calculated with the *density functional tight-binding* (DFTB) method for an isolated molecule with the corresponding symmetry, fourth column: external modes of β -perylene [35] scaled down by a factor of 0.8, and their symmetries for perylene. The last three columns give the amplitudes, dephasing times, and phases. The first three rows give results for internal modes, the next six rows for the external phonon modes. The last two rows are assigned to a DAVYDOV-split phonon doublet resulting from the same internal B_g vibration.

Mode cm ⁻¹	RRS cm ⁻¹	DFTB cm ⁻¹	Perylene*0.8 cm ⁻¹	Amplitude 10 ⁻⁴	Damping ps	Phase deg
569.2	565	577 (A_g)		1.6±0.3	1.9±0.4	91±14
542.0	536	537 (A_g)		0.8±0.3	2.0±0.9	29±23
221.1	218	219 (A_g)		6.8±0.3	2.4±0.2	41±3
104.9			96 (A_g)	5.0±0.9	0.8±0.2	-6±10
89.0			81 (B_g)	7.2±0.6	1.8±0.2	45±4
71.2			75 (A_g)	7.2±0.6	1.6±0.2	8±4
56.9			67 (B_g)	4.8±0.4	2.5±0.3	-32±4
43.0			42 (A_g)	0.7±0.2	13±12	-3±15
33.3			32 (B_g)	0.7±0.3	6±4	-68±22
25.3		16 (B_g)		0.5±0.2	16±26	165±21
4.7		16 (B_g)		6±2	4.3±0.7	-80±10

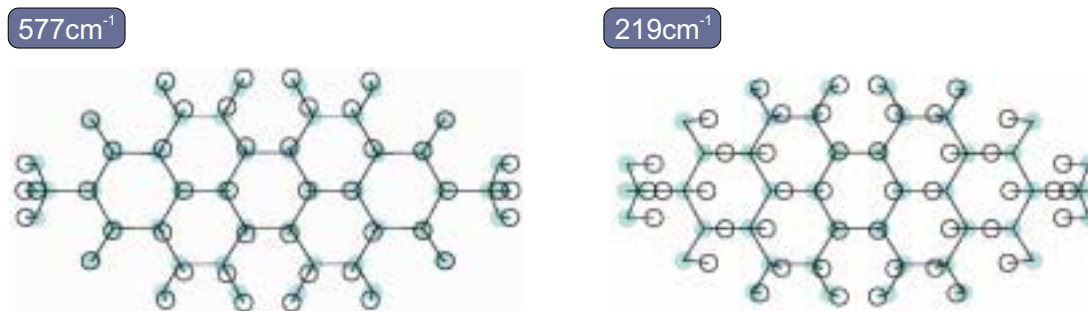


Figure 4.19: Calculated elongation patterns of two observed totally symmetric internal phonon modes at 577cm^{-1} (exp. 569cm^{-1}) and 219cm^{-1} (exp. 221cm^{-1}).

same symmetry argument applies to *Resonant RAMAN Scattering* (RRS) and RSIRS. Moreover, due to our limited temporal resolution, oscillations corresponding to energies above $\sim 700\text{cm}^{-1}$ are suppressed in our measurement. The calculated internal phonon energies in the relevant range are given in Tab. 4.2 and agree well with the experimental data.

Additionally, we compare the experimental oscillation energies with data from RRS on crystalline MePTCDI films [96]. We find an obvious one-to-one correspondence, although the frequencies show a shift of about $+1\%$, exceeding the fitting uncertainties, which is not understood up to now. From further pump-probe measurements on different conditions we can conclude that depopulation of the excited state occurs on sub-picosecond time scale (see Sec. 4.1.3). Therefore, the observed vibronic wavepacket motion is on the ground-state potential surface, as in the case in RRS measurements.

The deformation patterns of the observed 577cm^{-1} and 219cm^{-1} internal phonon modes as derived from the calculation of the vibrational eigenvectors are shown in Fig. 4.19. The lowest-frequency internal vibration corresponds to the in-phase shortening of the molecule, which is due to the vanishing of the node lines of the HOMO along the shorter in-plane molecular axis.

2.) External phonons

Considering the interpretation of the three higher energetic modulations as due to the lowest internal A_g phonons, we argue now that the six oscillations with energies between 33cm^{-1} and 105cm^{-1} are due to external phonons, i.e. rigid motions of the molecules in the unit cell of the organic crystal. The monoclinic $P2_1/c$ -symmetric MePTCDI crystal with two molecules per unit cell has 12 phonon branches: three acoustic translational, three optic translational and six optic rotational phonons (librational phonons). The translational optic phonons (B_u) are infrared active only, whereas the librational modes with even parity (three A_g and three B_g) are RAMAN active. The phonon modes of the MePTCDI crystal are given schematically in Fig. 2.12. As phonon modes are excited by RSIRS in our experiment, only the RAMAN active librations with $k \approx 0$ can contribute to the signal. We therefore assign the six observed low-frequency oscillations to librational phonons, i.e. hindered rotations of the rigid molecules around their fixed centers.

Since MePTCDI has the same crystal structure as β -perylene, we compare our data with the corresponding measured and calculated perylene phonon energies [35],

as outlined in [98]. The phonon frequency trends between different size conjugated molecules are not very pronounced, as was shown for, e.g. naphthalene and perylene [37]. This can be understood by a cancellation between mass (influencing the moment of inertia) and interaction related changes, which roughly conserves the pattern of the phonon frequencies. The expected conservation of the frequency pattern, we consider by a simple scaling factor. Therefore, we relate our measured external phonon modes to β -perylene with a scaling factor of 0.8, giving a rough estimate of both effects. The results of this estimation are given in Tab. 4.2. The good agreement with the experimental energies supports our interpretation that the lower frequency oscillations are indeed due to external phonons.

3.) Internal B_g vibrations

We now address the nature of the two lowest energetic modes. From group-theoretical arguments, only totally symmetric A_g vibrations of the isolated molecule can be elongated due to the dipole transitions from the HOMO to the LUMO, and the same symmetry argument applies to RRS.⁴ However, considering not the isolated MePTCDI molecule (symmetry group C_{2h}) but the two molecules in the unit cell, the symmetry is lowered from C_{2h} to the monoclinic centro-symmetric group $P2_1/c$ for crystalline MePTCDI. Hence, any vibrational mode of even parity is RAMAN active, including also the internal vibrations which would have B_g symmetry in the C_{2h} -symmetric isolated molecule.

Our calculation for the isolated molecule gives the lowest internal B_g vibrations at about 16cm^{-1} and 69cm^{-1} . The lower is due to a rotation of the methyl groups against the perylene core including the carboxylic groups, the higher due to a rotation of the carboxylic groups against the perylene core. Assuming that a possible RAMAN activity of the 69cm^{-1} mode is hidden under the rather strong contributions of the external phonons, the existence of the 16cm^{-1} mode can explain why we observe two further oscillatory contributions with frequencies below the expected six librational modes: We tentatively assign both the 5cm^{-1} and the 25cm^{-1} mode to a DAVYDOV-split phonon doublet resulting from the internal B_g vibration at 16cm^{-1} on both molecules. The splitting of about 20cm^{-1} is comparable to the DAVYDOV-splitting of the corresponding doublets of external modes, compare Table 4.2. The somewhat higher splitting can be related to the fact that a pair of degenerate modes is affected more by a coupling term of similar size if the mode frequency itself is low.⁵ The deformation pattern of the 69cm^{-1} and 16cm^{-1} mode, as derived from the calculation of the vibrational eigenvectors, are shown in Fig. 4.20.

In the following, we discuss the damping times of the different modes, as obtained

⁴Vibrational modes of B_g symmetry could only contribute to the signal if nearly degenerate electronic transitions with different orientations of the transition dipoles would be available, but for the isolated MePTCDI molecule, this is not the case in our range of photon energies.

⁵For the crystal modes, the dynamical matrix decouples into four submatrices of same size for the four different representations occurring in $P2_1/c$, e.g. A_g , which therefore can be diagonalized separately. Each of these submatrices contains both external and internal degrees of freedom, so that after the diagonalization the eigenvectors can have a mixed character. To simplify the discussion in the main text, we have discussed the modes in terms of *external* and *internal* if we expect that the eigenvector is dominated by the corresponding contribution.

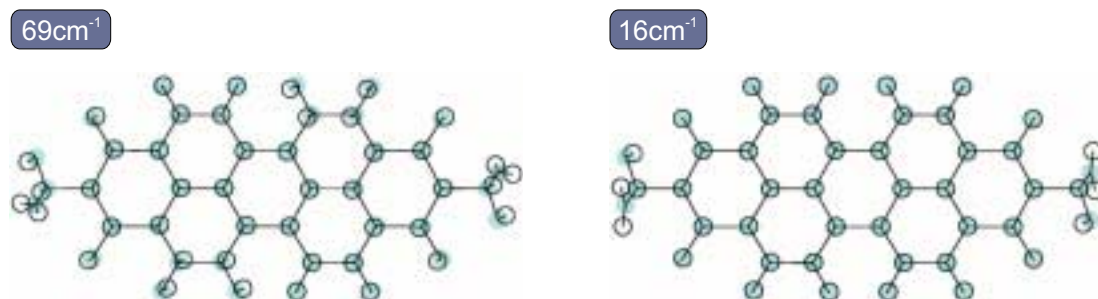


Figure 4.20: Calculated elongation patterns of two observed B_g symmetric internal phonon modes at 69cm^{-1} and 16cm^{-1} . The 16cm^{-1} mode was experimentally observed as a DAVYDOV-split phonon doublet at 5cm^{-1} and the 25cm^{-1} .

from the fits. Note that for some oscillations the decay time has a large uncertainty since they carry only minor amplitude. For the internal A_g phonon modes, we measure similar decay times around 2ps for all three modes. This is in close agreement with typical dephasing times for internal phonons of large organic molecules in solution on the ground electronic surface [100, 101]. In polymers, i.e. organic solids that lack the long-range order of crystals, values of 0.4 – 3ps have been measured [102, 103].

For the higher external modes, we obtain shorter damping times. The damping times show a clear trend with energy: They increase from 0.8ps for the 104.9cm^{-1} mode to 2.5ps for the 56.9cm^{-1} mode. For the two lowest energy external phonons, the times increase further, although the errors become very large. The only comparable measurements have been performed for crystals of pyrene, where the molecules arrange not quasi-1D in a chain, but pairs of the molecules align sandwich-like. In this case, a damping of external phonon wavepackets within some picoseconds was observed [42].

From further TA measurements, we know that depopulation of the initially photoexcited states at $k = 0$ occurs on sub-picosecond time scale, i.e. faster than the observed phonon coherence (see Sec. 4.1.3). The observed vibronic wavepacket motion is, according to this, on the ground-state potential surface, which is solely accessible in RRS measurements. To our knowledge, no microscopic theory of external as internal phonon damping exists for organic crystals.

In summary, the results presented here are the first observation of coherent external and internal phonon wavepackets in quasi-1D OMCs with strong orbital overlap. We were able to coherently prepare and probe wavepackets within an energy range of $5 - 600\text{cm}^{-1}$. Eleven modes strongly coupled to the lowest excitonic transition are identified, their damping times lie in the range of some picoseconds. In the case of external phonons, we find a strong increase of damping time with decreasing energy. The found phonon modes have to be related to the electronic ground-state potential energy surface.

4.3.1 Frequency vs. Time-Domain Vibrational Spectroscopy

Vibrational spectroscopy has traditionally been performed in the frequency domain. By comparing time-resolved vibrational spectroscopy with depolarized resonant RA-

MAN spectroscopy, as a frequency domain technique, one might expect the information content to be the same. Thus, the time-domain signals can be FOURIER transformed, using the pump-probe delay as the time variable. However, the information content is not necessarily the same.

There are more experimentally controllable variables that influence the signal for time-resolved vibrational spectroscopy (pump and probe pulse width, pulse shape, spectrum, chirp, etc.) which can be varied to produce significant changes in the observed signals. Here, we want to give only two intuitive examples for a possible influence of experimental conditions on observed frequencies. For a more detailed discussion of this topic, we refer to [104, 105].

In time-resolved TA spectroscopy, the photon energy of the pump beam influences the results in the following way: Scanning the pump laser to higher energies might lead to a modest down shift of observed frequencies, since higher vibrational states are excited. This is a direct consequence of the anharmonicity of the potentials. Additionally, there is a dependence on the photon energy of the probe. When probing the wave-packet motion at the point of return, the observed oscillation is equal to the vibrational frequency. Probing in the center of the potential yields oscillations at twice the vibrational frequency, since the wave packet passes the probed region twice per cycle. We have not observed this effect in our experiments, while overtone progression is a prominent feature in RRS spectra. The argument for the dependence of observed frequencies on pump-photon energy will also hold for a dependence on probe-photon energy.

In general, all experimentally relevant parameters, as enumerated above, will influence the phase of the oscillations. A quantitative analysis of the observed phases, in order to obtain the potential surfaces of the system, will only work for small molecules containing few electrons. Furthermore, the chirp of the used pulses is required to be very small and measured with high precision. In our experiment, pump and probe pulses differ in spectrum and chirp. One might think of obtaining detailed information about the potential surfaces from these data. However, further analysis and interpretation of coherent phonons in MePTCDI would require much more experimental data, e.g. as a function of probe spectrum and chirp. This is far beyond the scope of this work.

The advantage of time-resolved spectroscopy is the sensitivity at low vibrational frequencies, a region that is often obscured by laser scatter in the frequency domain. In addition, using this technique, we potentially have access to the vibrational dynamics in the excited state, which is not accessible by RRS spectroscopy.

The advantages of conventional RAMAN spectroscopy are the simplicity and ease of measurement, and the sensitivity at high vibrational frequencies, which require very short pulses for time-domain observation. For instance, the use of unchirped 20fs laser pulses restricts the accessible frequency range to less than 1000cm^{-1} . However, decreasing the pulse width causes a loss in information about low-frequency modes, because the decreased propagation time on the excited state surface allows less motion of the wave packet and, thereby, a smaller contribution to the signal for slower vibronic motions.⁶ Also, a simple FOURIER transformation, using the pump-probe delay as the

⁶More precisely, it is the effective excited-state frequency in the FRANCK-CONDON region and not the ground-state frequency that is important, since the velocity of the wave packet in the excited state

time variable, can give misleading results since this procedure implicitly, and incorrectly, assumes a constant phase for all oscillatory components of the signal. The potentially better method of obtaining the power spectrum is to fit the time-domain signal to a sum oscillatory components (4.5), as done in our case.

determines the distance traveled within the pulse width.

5 Conclusion

Summary

Within the framework of this thesis, we have investigated excitonic and phononic properties of MePTCDI as a model system for quasi-1D organic molecular crystals. Whereas absorption properties are understood in principle, knowledge about relaxation and recombination processes is still limited. Therefore, we have investigated the nature of emitting states and the exciton relaxation to these states. Furthermore, the dynamic properties (internal and external phonons) were investigated in the time domain. At this point, we put together the answers to the questions from Sec. 2.6, as far as possible.

- On which time-scale are optically excited states depopulated (away from $k = 0$)?

We found for both the two lowest free-exciton bands identical ultrafast depopulation of the states at $k = 0$ with a time constant of about 50fs.

Relaxation from the second lowest free-exciton band is not via states at $k = 0$ of the lowest band.

- How long does it take to complete excited-state relaxation? To say it in other words, how long does it take to populate the luminescent states?

We found the ultrafast relaxation from optically excited band states at $k = 0$ to the emitting states to have an overall time constant of about 50fs. We did not observe any intermediate state to slow down this relaxation or just to appear in our measurements.

- What is the nature of the emitting states?

We presented measurements on time-resolved luminescence to give a database for this discussion. We found three dominant luminescent transitions, showing different decay dynamics. These are intrinsic transitions, not determined by defects. We introduced two models to explain the emission properties: a bandlike description (emission from free-exciton band states at $k = \pi$), and a localized description (emission from self-trapped states). Both, the models seem to be reasonable, and finally, we can not exclude one of them.

- Are the optical transitions determined by homogeneous or inhomogeneous broadening?

To investigate the coherent regime of free-exciton transitions we have applied degenerate four-wave mixing. Unfortunately, the signals (showing exponential decays of 13fs) are limited by the time resolution of the experiment. Therefore, we can

only estimate the dephasing time for the lowest excitonic transition in the range of $17 < T_2 < 52\text{fs}$ (corresponding to a homogeneous line width $80 > \Gamma_{\text{hom}} > 27\text{meV}$). It is thus not clear, whether the transition is dominated by *homogeneous* or *inhomogeneous* broadening. The lower limit of the estimate is given under the assumption of the linear-excitation regime, e.g. no contributions of *excitation-induced dephasing*. In the nonlinear-excitation regime, even shorter T_2 -times are possible.

- What can we learn about the phononic properties of a quasi-1D crystal of small molecules?

Phonon modes are strongly coupled to the optical transitions of the quasi-1D OMC of MePTCDI. We were able to coherently prepare and probe wavepackets on the electronic ground-state potential energy surface. We could observe both coherent oscillations of intramolecular vibrational wavepackets (internal phonons) and, for the first time in a quasi-1D organic system, lower-energetic modulations which are related to coherent lattice phonons (external phonons). All phononic wavepacket motion is attributed to the electronic ground-state potential surface. The coherence decay of all observed vibrations is in the range of some picoseconds. In the case of external phonons we find a strong increase of damping time with decreasing energy.

Outlook

Two of the questions given above could not be answered satisfactory. Thus, this outlook should motivate how to find the answers and how to overcome the related problems.

There are two main points to discuss: The first point is directly connected to our experiments; the quality of our ultrabroad laser pulses is still not sufficient for sub-20fs or phase-sensitive measurements. The second point is the lack of understanding of the relaxed excited states. Does excitons in MePTCDI as quasi-1D crystal undergo self-trapping? If yes, this probably would prevent this promising material from emitter applications.

One of the main problems of our time-resolved measurements in the femtosecond-time range, which was already discussed in Chapter 3, is the omnipresent frequency sweep of the pulses (the so-called *chirp*). This problem can be overcome by usage of an electronically driven pulse shaper with the possibility of flexible control and compensation of higher order chirp (see Sec. 3.1.2). Thus, the next step is to successfully implement the pulse shaper in the setup, resulting in sub-10fs pulses at around 550nm. Then, time resolution might be sufficient for DFWM measurements concerning the coherent regime of free-exciton transitions. Various TA measurements on the ultrafast exciton relaxation in the sub-100fs range could also be redone, as there still might be processes being not yet time-resolved. Additionally, the variable phase control of the pulse frequency allows more detailed investigation of coherent phononic properties. And let me mention that there are various experiments of ultrafast spectroscopy not performed yet, such as *hole-burning spectroscopy*, *transient polarization rotation* or *two-photon spectroscopy* which might give further insight into relaxation processes.

The second point, which should be in the focus of future work, is the identification of relaxed exciton states. Time-resolved observation of luminescence and TA spectroscopy are probably the most powerful techniques to investigate excited-state relaxation and the nature of relaxed excited states. However, these techniques, as any kind

of spectroscopy, investigate transitions between states and not the states itself. The interpretation of experimental results, especially for TA spectroscopy, is not straightforward and requires knowledge about the involved states. Therefore, identification of the luminescent states probably requires additional experimental approaches: *Femtosecond resolved luminescence* can be used to investigate emission at very early times. In particular, *picosecond X-ray spectroscopy* might be the key to monitor any lattice relaxation of the excited state, such as exciton self-trapping. Recently, first promising results of applying this technique to OMCs were presented [106].

So far, quasi-1D OMCs, such as MePTCDI and related perylene derivatives, are used in solar cells and as electron transport layers [13, 14]. Many more possible applications are not yet explored. Therefore, in the future, our methods of time-resolved optical spectroscopy should also be applied to thin films of MePTCDI with applied electric field and carrier injection.

Part II

Self-Assembled Monolayers of Photochromic Molecules

6 Introduction

Nanotechnology will be among the key technologies of the 21st century. With the discovery of manipulation techniques of the individual elements of matter, a world-wide industrial conquest of nanoscale dimensions began within the last decade. The technological exploitation is based on the increasing insight into self-organization principles of these elements. It is providing commercial products even today, for example hard disks and reading heads for data storage, covered with thin films of a few nanometers, and scanning tunneling microscopes making individual atoms and molecules visible. Ultrathin films are among the main elements of nano technology with widely varying applications in microelectronics, optics, medical equipment, and wear protection.

Purely geometrically, the prefix "nano" (greek: dwarf) describes a scale 1000 times smaller than that of present elements of the micrometer world. This scale has become accessible both by application of new physical instruments and procedures and by further diminution of present microsystems. So far, two ways in the generation of nanosystems have been taken and pursued in research and development within the respective fields:

- On the one hand, technology was taking direction into the nanometer dimension by constantly manufacturing smaller structures and basic elements of new materials (*top-down strategy*). The gained experiences contribute especially to the fields of electronics, optoelectronics and sensor technology. In this way, it is necessary to make use of new physical interaction mechanisms, which causes are based on the transition from classical (continuum) physics to quantum physics. For the future production of sub-100nm-scale structures most diverse ideas are being discussed. These refer usually to projecting, but also to serially writing techniques with light and particle beams.
- On the other hand, a strongly increasing number of processes running in animated nature is well understood and utilized today. The principles of self-organizing of atomic or molecular units to larger systems, the growth of functional units, and the selective chemical or physical coupling of molecular systems at prepared surfaces are understood today (*bottom-up strategy*). The knowledge gained is applied particularly for the development of new materials, for instance within the areas of life sciences.

Finally, an additional leap in technology development will be achieved, if the advantages of *top down* (parallelism and thus high throughput) can be combined with those of *bottom up* (selforganizing growth and thus reproducible nanometer dimensions).

For a multitude of reasons, organic ultrathin films have attracted considerable attention over the last years. BLODGETT did the first study on the deposition of long

chain carboxylic acids on solid substrates in the 1930s [107]. A strong activity in the area of ultrathin films and especially self-assembled monolayers (SAM) started in the 1980s with the progress in the understanding on a microscopic level. Around that time, important experimental tools like scanning probe microscopy and grazing-incidence X-ray diffraction were developed. Nowadays, with various microscopic tools available, one can attempt to correlate macroscopic to microscopic properties, e.g. the wetting properties to molecular structure and layer formation.

Besides applications in "classical" areas of technology, ultrathin organic films can play an important role in interfacing biotechnological devices. Furthermore, ultrathin and nanostructured films have become important elements of present-day optics and optoelectronics or photonics. Intense research is proceeding on active optoelectronic elements consisting of ultrathin films. As latest examples of novel light-emitting substances, semiconductor nanocluster for Si-based light emission and organic light-emitting diodes may be mentioned. X-ray mirrors consisting of stacks of ultrathin films of a few nm thickness are increasingly applied as beam shaping elements in analytics.

Probably, one of the most fascinating application is the combination of functional molecular systems and the abilities of monolayer growth to achieve functionalized layers with control in different ways (optical, electric, magnetic, ...). Possible applications for functional layers are filter layers, reflex-reducing layers, electro-optical layers, memory layers, sensor surfaces (bio-, chemosensors, mm-wavesensors), and surfaces with catalytic activity [108]. Particular interest has been concentrated on the exploitation of photofunctionality of ultrathin films to lead to the photoregulation of versatile physical properties, including ionic permeability, membrane potential, and electroconductivity and alignment of liquid crystals. Well investigated modules to be controlled by light are photochromic molecules, such as azobenzene. The configuration of photochromic molecules can be switched reversibly by light of appropriate wavelengths. Especially, the implementation of photochromic units seems to be very promising, and first examples are realized. However, the starting point for this technology is to grow ultrathin films of molecules with photochromic units and to realize the functionality of the layer.

Within the framework of this work, highly ordered SAMs of photochromic molecules could be realized and investigated. However, these layers do not show photochromic behaviour. A collective photoisomerization requires more space than given in our densely packed SAMs. The next step to achieve functionalized monolayers is to provide the required space by modification of the layer structure and/or molecular structure.

This part of the thesis is organized as follows. In the following sections of Chapter 6, we introduce the basic concepts of photochromic reactions and the growth of ultrathin films by self-assembly. For the latter topic, we follow the ideas of some comprehensive review articles and books: SCHREIBER gives a nice overview about the growth and structures of SAM [109], as well as ULMAN is doing in his comprehensive books on that topic [110, 111]. In Section 6.2.2, we address the status of research and open questions concerning SAMs of photochromic molecules. In Chapter 7, we introduce the experimental setups and techniques. The necessary background for data interpretation is provided. All experimental results are given in Chapter 8. First, we present the results concerning the structural investigations of SAMs. Therefore, we have performed measurements using scanning tunneling microscopy (STM) and IR spectroscopy. Ad-

ditionally, we show second-harmonic generation to be a powerful tool to investigate conformational changes of photochromic monolayers. Conclusions and an outlook to further measurements are presented in Chapter 9.

6.1 Photochromic Reactions

The molecular mechanism of several photoregulated biological processes, such as vision, is based on photochromic molecules. In biological systems, photochromic molecules are embedded in macromolecular matrices. The photoisomerization of a photochromic component induces variations in the conformation of the macromolecule and triggers the subsequent reactions. Incorporation of a photochromic component into an artificial supramolecular structure can lead to artificial photoresponsive species that may be fairly valuable as model systems for theoretical studies and as photochemical devices.

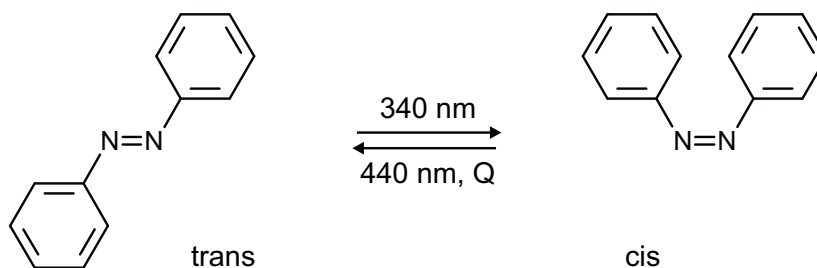


Figure 6.1: Isomerization of azobenzene.

The best studied and most widely used chromophores in artificial supramolecular systems are the aromatic azo and olefin-type compounds, namely azobenzene and stilbene [18, 112]. Azobenzene and stilbene have the same geometry as the ethylene group and are, thus, comparable. Azobenzenes have been employed most extensively as representative photoactive molecules triggering photoresponsiveness of materials on account of their good availability and acceptable photofatigue resistance. The photoisomerization of azobenzene is reversible and one of the cleanest photoreactions known. In purified solvents with exclusion of oxygen, irradiation with visible or near-UV radiation induces no side reactions.

We will recall the principal characteristics of the photoinduced processes that cause conformational change in azo-type compounds. Azo compounds received their name from the azo group $-\text{N}=\text{N}-$. There are two stable configurations, the *trans* (or "E") and the *cis* (or "Z") forms (see Fig. 6.1). The two geometric isomers of *trans* and *cis* azobenzene can be separated; their molecular structure has been confirmed by X-ray analysis [112, and references therein]. The interconversion of these two isomers can be effected by light and heat. As the *trans* form is generally more stable, by about 50kJ/mol in the case of azobenzene, the thermal isomerization is generally in *cis* \rightarrow *trans* direction. Light induces transformation in both directions.

Beside the binding π electrons, azobenzene has unbound pairs of electrons (n) on both nitrogen atoms, which have to be considered discussing *cis-trans* isomerization. The molecules are characterized spectroscopically by a low intensity transition $n\pi^*$ in the visible ($\sim 450\text{nm}$) and a high-intensity transition $\pi\pi^*$ in the UV ($\sim 340\text{nm}$). Figure

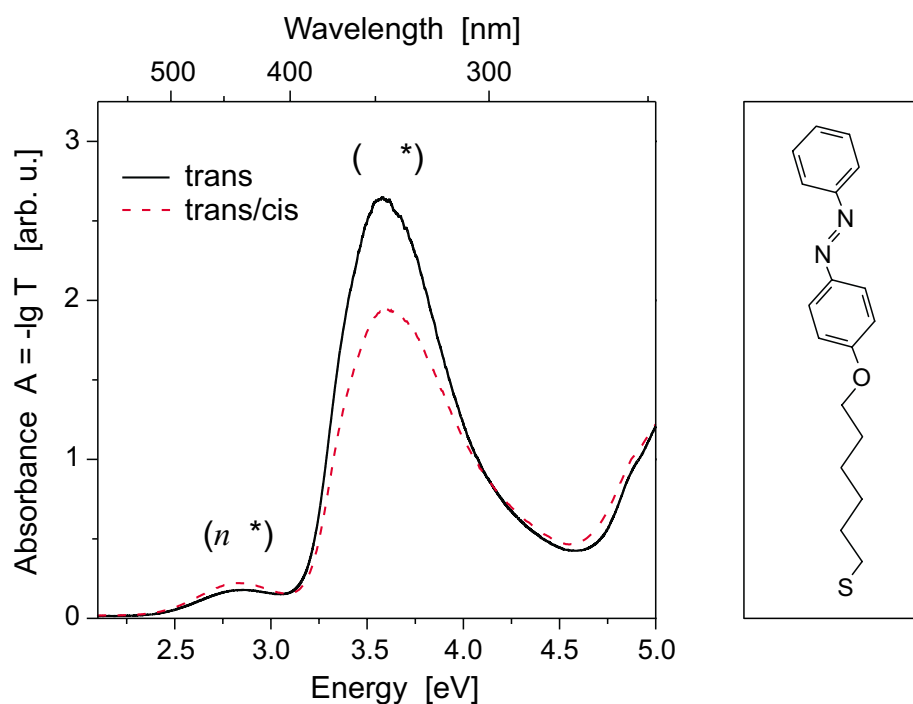


Figure 6.2: Absorption spectra of [4-(phenylazo)phenoxy]hexane-1-thiol (given as inset) in dichloromethane at room temperature. Shown are spectra of the molecules in *trans* configuration (solid line) and after partial *trans* \rightarrow *cis* isomerization (dashed).

6.2 shows typical absorption spectra of [4-(phenylazo)phenoxy]hexane-1-thiol (short: AzoC₆) in its configurations. This is the molecule as used for all our investigations. The linkage of alkanethiol to the azobenzene group influences the transitions only very little. The $n\pi^*$ transition in the visible is (mainly) symmetry forbidden in the *trans* isomer (C_{2h}) but allowed in the *cis* isomer (C_{2v}). Its maximum absorbance at around 450nm is about three times larger for the *cis* form. Still, the $n\pi^*$ transition of the *trans* isomer is intense, which is attributed to nonplanarity of the molecule and vibrational coupling.

There are two possible isomerization coordinates: (i) twisting about the $-\text{N}=\text{N}-$ double bond, as the exclusive path in the case of stilbene, and (ii) in-plane conversion at one of the two nitrogen atoms. It is not yet clear whether photoisomerization takes place exclusively via inversion or via twisting and inversion, depending on the excited state populated by light excitation [112, 113]. Besides the structural rearrangement, photoisomerization of azobenzene involves a big change in the dipole moment. The *trans* form is planar and has no dipole moment, whereas the *cis* form is nonplanar and exhibits a dipole moment of 3.0 D [114].

Photoisomerization is a statistical process, the isomerization quantum yields $\phi_{c \rightarrow t}$ and $\phi_{t \rightarrow c}$ can be obtained from the evaluation of the reaction kinetics. Table 6.1 shows typical values for excitation of azobenzene within the lowest two absorption bands. Either uncertainty of the given values must be rather high or experimental conditions strongly influences the results, because values in literature differ rather strongly [18, 112, and references therein]. Azo compounds are quite stable, only the *cis*-azobenzene tends

to undergo thermal decomposition into nitrogen and radicals.

Table 6.1: Isomerization quantum yields for azobenzene on $n\pi^*$ and $\pi\pi^*$ -excitation in solution (taken from [112]).

$n\pi^*$		$\pi\pi^*$	
$\phi_{c \rightarrow t}$	$\phi_{t \rightarrow c}$	$\phi_{c \rightarrow t}$	$\phi_{t \rightarrow c}$
0.24	0.55	0.12	0.40

Recent examples for possible implementation of photochromic molecules in devices are optical shutters [115] and memories [116] realized by azobenzene containing polymer liquid crystals, and full-color rewritable "paper" based on azobenzene containing nonpolymer liquid crystals [117]. Examples for the SAM-based devices are given in Sec. 6.2.2.

6.2 Organic Thin Films

In view of several million organic compounds known, and a correspondingly wide variety of molecular properties, it is not surprising that there are different routes for the preparation of organic thin films. For the group of crystalline films of relatively small molecules, several methods can be applied:

- LANGMUIR films consist of amphiphilic molecules spread on a liquid surface like water. The hydrophilic headgroup has an affinity to the water while the hydrophobic endgroup stick out on the other side.
- LANGMUIR-BLODGETT (LB) films are prepared by transferring LANGMUIR films onto a solid substrate. The monolayer is physisorbed to the substrate. Multilayers are prepared by repeated dipping of the substrate in appropriate solutions.
- Organic Molecular Beam Epitaxy (OMBE) is very similar to evaporation techniques in ultrahigh vacuum for inorganic materials. For example, various perylene-derivatives, which form crystals in the bulk, are typical materials for OMBE.
- Self-Assembled Monolayers (SAM), grown from solution or from the gas-phase, represent a further class of organic thin films. The defining feature is the chemisorption (or, generally, strong interaction) of the headgroup with a specific affinity to the substrate. Since SAMs are the subject of this work, the concept of self-assembly is discussed in more detail in the next section.

The boundaries between some of these techniques are not rigid. For example, some systems prepared from the gas phase in the monolayer regime, might be considered in principle both as OMBE systems and as SAMs. Also, one might view the distinction between LANGMUIR layers and SAMs as not absolutely sharp.

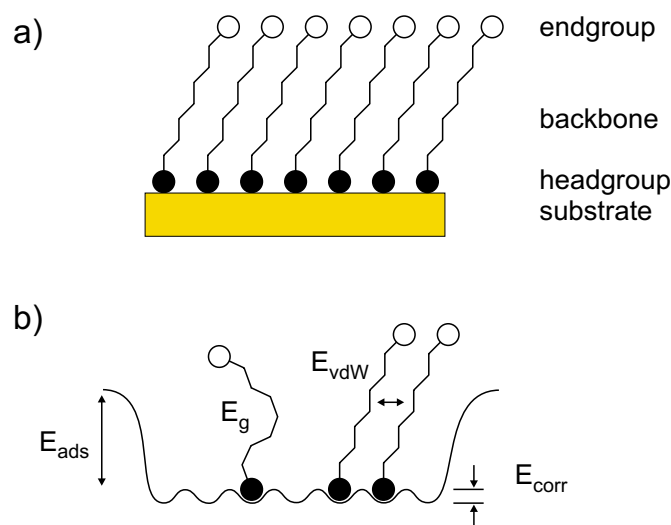


Figure 6.3: (a) Schematic of SAM. Shaded circle indicates chemisorbing headgroup and open circle endgroup, which can be chosen from variety of functionalities. (b) Schematic of different energies. ΔE_{ads} stands for adsorption energy, ΔE_{corr} corrugation of substrate potential experienced by the molecules, ΔE_{vdW} VAN DER WAALS interaction of tails, and ΔE_g energy of deviation from fully stretched backbone.

6.2.1 Concept of Self-Assembly

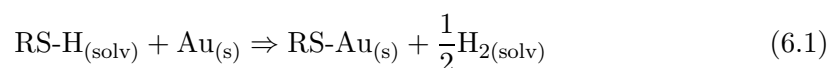
Self-assembly, in a general sense, might be defined as the spontaneous formation of complex hierarchical structures from pre-designed building blocks, typically involving multiple energy scales and multiple degrees of freedom. Self-assembly is a very general principle in nature and not limited to surfaces, as seen in the formation of, e.g. membranes from lipid molecules.

SAMs are ordered molecular assemblies that are formed spontaneously by the adsorption of a surfactant with a specific affinity of its headgroup to a substrate. The affinity is provided by a covalent chemical reaction, as in silanes on silicon oxide [118], by an ionic interaction, as in carboxylic acids on alumina [119], or by a charge transfer complex, as in alkanethiols on noble metals [120]. A common feature of these systems is the strong interaction between the functional group of the adsorbate and the bare substrate. Besides that, VAN DER WAALS interactions among the adsorbate molecules give rise to a dense packing of the monolayer. Figure 6.3 shows a schematic, including the constituents of a SAM-molecule (headgroup, chain or backbone, endgroup). The headgroup-substrate pair is usually used to define the individual SAM-systems.

As already mentioned, SAMs can be prepared both from solution and from the gas phase. The traditional route is solution deposition. Growth from the gas phase generally requires a more expensive experimental setup (i.e. usually a vacuum chamber), but offers also some advantages, such as better control of the cleanliness of the environment as well as the applicability of essentially all the established methods known in surface science including in situ structural methods, like e.g. grazing-incidence X-ray diffraction (GIXD) and low-energy electron diffraction (LEED). In contrast, the number of in situ methods for solution growth is limited.

Alkanethiols are the most intensively studied system because they react with several metals that are inert to almost any other reaction and, thus, allow a wide variety of functional groups to be placed at the opposite end of the alkyl chain. It was found that sulfur compounds coordinate very strongly to gold, silver, copper and platinum surfaces [110]. However, most of the work to date has been made on gold surfaces, mainly because of the fact that gold does not have a stable oxide, and thus, it can be handled in ambient conditions. Furthermore, the thiol group forms the strongest interaction with the gold surface over all headgroups studied. For these reasons, the alkanethiols/gold system was chosen for our experiments.

Chemisorption of alkanethiols on gold surfaces yields the thiolate-gold (RS-Au) species. The formation of RS-Au requires the loss of the SH hydrogen, but it has not been determined yet whether this proton is lost as H₂, or as H₂O in a reaction with another oxidant. The current understanding of the reaction is given in [111]. The primary reaction reads as



A fresh, clean, hydrophilic gold substrate is usually immersed into a dilute solution (10⁻³M) of the organosulfur compound in an organic solvent. Immersion times vary from several minutes to several days for alkanethiols depending on, e.g. the solvent, endgroup and chain length. The result is a close-packed, oriented monolayer. Concerning the dependence on the chain length, it was found that the kinetics is faster for longer alkyl chains. This is due to the fact that VAN DER WAALS interactions are a function of the chain length.

6.2.2 Status of Research / Open Questions

Self-assembled monolayers on solid surfaces have been investigated to a large extent during the last decade. A thorough overview concerning SAMs is given by SCHREIBER [109]. The by far best analyzed systems are linear *n*-alkanethiols on Au(111) [121]. Since the main driving mechanism for the ordering within the thiol monolayer is the strong interaction between the thiol head group and the gold substrates, the idea to attach a functional group to the tail of the alkyl chain in order to achieve ordered arrays of these functional units has been developed.

The structure of SAMs of various azobenzene functionalized thiols on Au(111) has been investigated previously by means of real space analysis [122, 123, 124, 125, 126, 127] (STM or atomic force microscopy (AFM)) and X-ray diffraction [123, 127]. One result of these investigations is that the azobenzene moieties form an *incommensurate* surface mesh. This is in contrast to the typical situation for SAMs of linear *n*-alkanethiols with a commensurate ($\sqrt{3} \times \sqrt{3}$)R30° cell caused by the covalent bond between the sulfur atoms of the thiol groups and the gold atoms of the substrate surface. Apart from this commensurate lattice, there exists a c(4 × 2) superlattice in most alkanethiol SAMs which is believed to be mainly caused by head group interactions, i.e. sulfur atoms binding to nonequivalent gold lattice sites [128]. Nonequivalent binding sites are also quoted to explain the incommensurate unit cell in SAMs of AzoC₆ on Au(111) [122].

More often, it is assumed that the strong interaction between the azobenzene moieties causes the formation of an incommensurate lattice of the molecular end groups (azobenzene), with the sulfur atoms of the head group still occupying equivalent gold lattice sites, i.e. distances between the head groups on the substrate are still related to the 5.0\AA distances within the Au(111) plane while the spacings between the azobenzene moieties are not. The discrepancy between the latter assumption and the incompatible lattice constants as observed in STM/AFM investigations [123, 126, 127, 129] has been tried to overcome with the help of the so-called *bundle model*. In this model the alkyl chains of the molecules in a domain have different tilt angles and are leaning inwards the domain center. Therefore, the domain size is assumed to be limited by the amount of tilting the alkyl chains can undergo [123].

Different lattice constants were reported for azobenzene-terminated alkanethiol SAMs. For AzoC₁₀ [126] and AzoC₁₁ [123] rectangular lattices with two molecules in the unit cell were reported. In both cases a herringbone arrangement of the molecules was suggested for sterical reasons (area per molecule significantly below 20\AA^2) and the bundle model was used to explain the SAM structure. On the contrary, WOLF and DELAMARCHE [122, 125] obtained an almost rectangular lattice of AzoC₆ with two molecules per unit cell but an area per molecule of about 24.1\AA^2 . The significant difference in lattice constants was attributed to experimental conditions [129] (WOLF et al. investigated their SAMs in ethanol), or the credibility of their results was even called into question [127].

One goal of this work is to revisit AzoC₆ SAMs on Au(111) in the light of the results mentioned above. We will demonstrate that we neither have to assume an incommensurate structure nor is the bundle model necessary to explain the observed SAM structure of AzoC₆.

None of the publications on azobenzene thiols on Au(111) cited above, report on photoisomerization of the SAMs. The photofunctionalization of monolayers incorporating azobenzene units can only be realized by guaranteeing a free volume in the film for *trans-cis* photoisomerization since the photochemical process requires a sweep volume. The required sweep volume is not provided for SAMs of azobenzene thiols on Au(111). In contrast, photoisomerization was observed for azobenzene-containing LANGMUIR-BLODGETT multilayers [130, 131]. In [131], the area per molecule was found to be $30.4 \pm 0.5\text{\AA}$. However, *trans*→*cis* photoisomerization increased the area per molecule by more than 30% in the top layers. Therefore, we can not expect photoisomerization for SAMs of AzoC₆-thiol on gold as used in our experiments.

The required sweep volume can be provided by "mixed monolayers" containing the azobenzene molecules and short spacing molecules [132]. Another approach to provide sweep volume is the use of spacious molecules containing azobenzene residues (see also Chap. 9). The group of ICHIMURA could obtain SAMs of azobenzene-functionalized calix[4]resorcinarenes showing high level photoisomerizability [133]. These ideas are beyond the the scope of this thesis, but will trigger our further investigations.

7 Techniques for Studying Monolayers

In order to understand how to control and generate desired surface and thin film properties, it is necessary to characterize the physical and chemical structure of the film. Modern day surface science provides a great number of techniques for surface characterization. In nanoanalytics highly developed procedures and devices are used, operating with electron-, ion-, neutron-, neutral particle- and photon-beams, with field emission and tunnel effects as well as according to acoustic-, electrical-, thermal-, and magnetic principles. The application of different methods of analysis is necessary, depending upon each specific problem definition.

In this section we want to introduce the analytic techniques used to characterize SAMs. For quality control of highly ordered SAMs, scanning probe techniques are of high importance and have developed into the standard tool of surface scientists. Another very helpful technique for the investigation of the molecular structure, intermolecular bonding, as well as the orientation of molecules within SAMs is infrared spectroscopy in external reflection geometry. In order to investigate conformational changes, as e.g. photochromic reactions of SAMs, second-harmonic generation (SHG) is a sensitive technique. Additionally, it opens up the possibility to time-resolve joint activation of such functionalities.

7.1 Scanning Tunneling Microscopy (STM)

All STM images presented in this work were obtained by S. MANNSFELD with a Nanoscope III (Digital Instruments) in air at room temperature. The STM tips were cut from a PtIr wire (0.25mm). To obtain images with molecular resolution of AzoC₆, the tunneling current had to be < 5pA which in turn implies a rather low scanning frequency < 6Hz. The tunneling voltage applied was in the range of 0.8... 1.2V. Since a low scanning frequency introduces significant distortion into the STM images due to thermal drift of the scanner, special care has been taken to correct the images by recording consecutive STM scans. It can be shown that simple averaging of lattice vectors obtained from two consecutive images, like described in [122], does not give correct values unless the amount of drift is very small. However, in that case a drift correction would be obsolete anyway. We use the drift correction procedure described by STAUB et al. [134]. Based on the assumption that the drift vector is constant for two consecutive scans and negligible for a single scan line (which means that the scan lines are always horizontal), this method yields three correction parameters for each of the two images: two scaling factors (horizontal and vertical) and a shear angle.

Other errors, like nonlinear piezo response or nonorthogonality of the scanning axes, have been tried to overcome by calibration of the STM for exactly the scanning speed

and scanning size used to image AzoC₆ samples. This has been achieved by imaging graphite single crystals. Both, the correction for drift and the calibration can be written as 2×2 matrices. Before any image analysis, the product of these matrices was applied to STM images using standard image processing software. Because these corrections are based on measurements in distorted images, they implicitly contain experimental errors themselves. Since it would be quite complicated to calculate experimental error bars for measurements in corrected STM images, we assumed the correction methods to be error free and estimated the experimental error bars (2 pixels inaccuracy in the respective FFT images).

7.2 Infrared (IR) Spectroscopy

Infrared Spectroscopy covers the wavelength range from 2.5 to 50 μm or 4000 to 200 cm^{-1} . Unlike spectrophotometric, or actually most other techniques which respond to the electronic structure of a molecule, the IR-based probes give molecular structure and intermolecular bonding. The relatively high IR absorption cross section (compared to RAMAN and non-linear optical probes) and the relative ease in interpretability of IR spectra contribute to making IR vibrational probes the most generally useful optical probes for studying thick films. For the investigation of ultrathin films the approach of external reflection geometry at grazing incidence results in a sensitivity even adequate for submonolayer detection. The film to be analyzed is placed on a mirror. The absorption of the sample reduces the reflectance of the mirror, and kind of a squared transmission spectrum of the film results. Therefore, the technique belongs to the class of *reflection absorption* experiments. Unfortunately, there is no uniformly widespread name for the approach used in our investigations; we use the name *FOURIER transform infrared-reflection absorption spectroscopy* (FTIR-RAS).¹ Besides obtaining simply the IR spectrum from ultrathin films on metal surfaces it can be used for extracting orientation and physical structure information, intermolecular bonding from ultrathin organic films. For the introduction of this technique we follow partly the comprehensive review article by DEBE [135].

As indicated by Figure 7.1, external reflection-absorption IR spectroscopy probes the interface region above a metal surface by measuring the absorption of a reflected IR beam, incident at grazing angles. It differs from ordinary transmission IR spectroscopy, then, by the requirement of a reflective substrate and a non-arbitrary, large incidence angle. We will assume the substrate is a metal.² There are both classical electromagnetic and practical reasons for what the optimum angle is. The optical response of the metal dominates the reflectivity of a thin film overlayer plus metal substrate system. The reflectivity for the *s*- and *p*-polarized components of an electromagnetic wave incident at an angle θ on a metal surface, from air, is described by the FRESNEL equations. As the IR absorption intensity depends on the square of the electric field strength vec-

¹Combining the words infrared, reflection, absorption, spectroscopy and FOURIER transform, the following acronyms are also used in literature to describe this singular approach: RAS, RAIS, RAIR, IRRS, IRAS, IRRAS, RAIRS, FT-IRAS, FT-IRRAS, IR-ERS, etc.

²Even though, the technique loses its strongly enhanced sensitivity, it was shown to work also for non-metallic surfaces as multilayers on glass or monolayers on water. Extracting information is more difficult since the simple, strong surface selection rules will no longer apply and optical artifacts may appear [135].

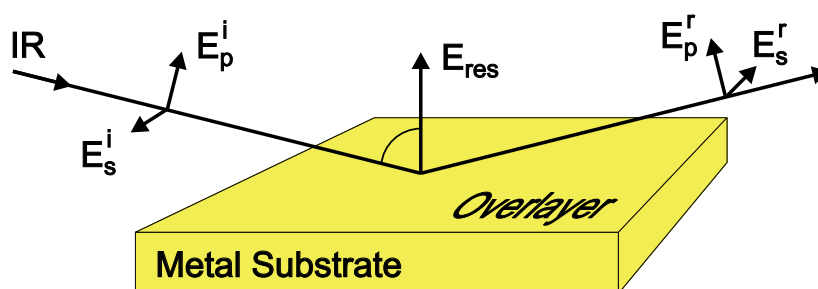


Figure 7.1: Definition of the configuration for glancing incidence external reflection-absorption infrared spectroscopy (FTIR-RAS). At near glancing incidence on a metal substrate, the p -polarized IR standing wave has a maximum at the surface, because the incident and reflected p components interfere constructively, whereas the s waves incident and reflected are out of phase by nearly π resulting in destructive interference.

for \mathbf{E} , the objective is to operate at conditions which will make \mathbf{E} as large as possible at the surface of the metal. We note in Figure 7.1 that E_p^i (incident) and E_p^r (reflected) each have a surface normal (\perp) and a surface parallel (\parallel) component, while E_s^i and E_s^r are both parallel to the surface. The incident and reflected fields produce a resultant field at the surface, the magnitude and direction of which depends on the phase change occurring upon reflection by the s and p components. The actual functional form of the phase shifts $\Delta\varphi_s$ and $\Delta\varphi_p$ for the reflected components of the electric field can be found in literature, e.g. [136]. The phase shift is $\Delta\varphi_s \sim \pi$ at all angles of incidence. Since E_s^r and E_s^i are nearly exactly out of phase, they cancel producing a very small resultant field parallel to the substrate at all angles. The phase shift $\Delta\varphi_p$ is small for the larger part of the angular range before it increases sharply to π when approaching grazing incidence. These contributions of the incoming and reflected wave interfere constructively. Provided the reflectance of the substrate is close to unity, the resultant field vector is of nearly twice the incident field strength and oriented perpendicular to the metal surface. Depending on intensity, the absorption signal is increased up to a factor of four. An equally significant realization is that this technique is highly polarized because the surface normal component of the effective intensity is a thousand times larger than the surface parallel contribution. Therefore, an interaction is exclusively possible with transition moments or components oriented perpendicular to the surface. This selection rule is a result of great significance for extracting orientation information. Models for quantitative orientational analysis of FTIR-RAS spectra are presented in [135]. Fortunately, our experiment reveals a special case, where no further modeling is needed.

Another effect improving sensitivity is a simple geometrical effect. If the beam has cross-section area A , then at an incidence angle θ , the area of the sample illuminated is $A/\cos\theta$, assuming the sample is large enough. Recalling again that the absorption depends on E^2 , the total "enhancement" of the absorption compared to normal incidence results in a factor of about thirty.

Now, if a thin overlayer is introduced, the reflectivity will still be dominated by the metal surface, but effected by the complex refractive index of the film. The absorption enhancement is reduced because the electric field strength within the film is reduced. For monolayers, the concept of refractive index becomes questionable and E^2 is not

changed much over the film depth. For such ultrathin films, i.e. thickness $d \ll \lambda$, the absorbance will vary quite linearly with the film thickness [137].

We discuss now how the spectrum is measured. Since a change in reflected intensity produced by the overlayer is the basic quantity being sensed, the experimentally quantities to be measured are the reflectivity with and without the ultrathin film, R_p and R_p^0 . As the s component produces little resultant intensity near the surface it carries no absorption information to the detector. So, usually a linear polarizer is used to allow only the in-plane polarized intensity to be measured. Renunciation of the polarizer would double the background level and so the noise contributions! The physical quantity which is probed is the absorption of the overlayer in reflection geometry, so the absorbance spectrum is given by $-\log(R_p/R_p^0)$. Finally, it should be noted that for practical reasons (restricted sample size, use of circular beams) most IR interferometers work at incidence angles of 80° .

7.3 Second Harmonic Generation (SHG)

A different approach to investigate ultrathin films of molecules on surfaces is *Second Harmonic Generation*. The method is especially suitable to investigate (sub-) monolayers because it is a surface-sensitive method. In comparison to other nonlinear optical techniques, such as, e.g. surface Coherent Anti-STOKES RAMAN Scattering (CARS) or stimulated RAMAN gain techniques, SHG is much simpler in the experimental arrangement and much stronger in the signal output. Another advantage is its sensitivity to conformation of the photochromic unit. Even if SHG is not a microscopic technique, it is easily possible to investigate conformational changes. Potentially, it opens up the possibility of time-resolved measurements of photochromic reactions of monolayers in the sub-ps time range.

Molecular materials consist of chemically bonded molecular units that interact in the bulk (or even monolayer) through weak VAN DER WAALS interactions. For these materials the optical nonlinearity is primarily derived from the molecular structure. For instance, organic materials with conjugated structure that involve alternate single and multiple bonds exhibit large optical nonlinearities. This property is caused by the delocalized π -electron system [138]. This behaviour is very different from inorganic semiconductors or ionic crystals in which no single molecular unit in the bulk can be identified; consequently, the nonlinearity in these materials is a bulk effect. First, we start to derive the requirements for molecular units to show high second-order nonlinearity. Finally, the expression of the nonlinearity is highly dependent on the geometrical arrangement of the molecules in the condensed medium in the case of second-order nonlinear process, but much less so for third-order nonlinearities.

We have already introduced some nonlinear optical techniques in Sec. 3.2. In analogy, the interaction of the radiation field with a molecular unit induces a molecular polarization \mathbf{p} which can be described in dipole approximation as a power series of the field strength \mathbf{E} :

$$\mathbf{p} = \alpha \cdot \mathbf{E} + \beta : \mathbf{E}\mathbf{E} + \gamma : \mathbf{E}\mathbf{E}\mathbf{E} + \dots \quad (7.1)$$

This equation is the microscopic analogy to (3.18) describing the induced macroscopic

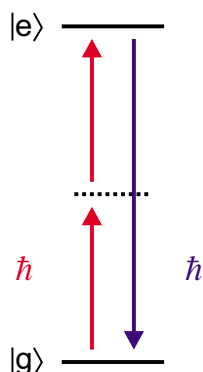


Figure 7.2: Excitation scheme for second-harmonic generation of a two-level system. Excitation is chosen to result in resonance enhancement while one-photon absorption does not occur ($E_e - E_g = 2\hbar\omega$).

polarization of the bulk. The quantity α is the linear polarizability, which describes the linear optical response to the applied electric field. The coefficients β and γ describe, respectively, microscopic second- and third-order nonlinear optical responses of a molecule, and are called the first and second hyperpolarizabilities. They are third and fourth rank tensors, respectively. In the sum-over-states approach, the expression for the microscopic second-order coefficient $\beta(-2\omega; \omega, \omega)$, which is responsible for SHG, is given by [139]:

$$\beta(-2\omega; \omega, \omega) \propto P \sum_{n,m} \frac{\langle g|\mu|n\rangle \langle n|\mu|m\rangle \langle m|\mu|g\rangle}{(\omega - \omega_{ng} + i\Gamma_{ng})(2\omega - \omega_{mg} + i\Gamma_{mg})} \quad (7.2)$$

where g represents the ground electronic state, n, m are various excited states, ω_{ng} are the transition frequencies, and Γ_{ng} are the corresponding damping terms. P stands for various permutation terms. The SHG process is represented as three-wave mixing in which two waves at frequencies ω mix to produce an output at a frequency 2ω . Resonance enhancement occurs when $\omega_{ng} = \omega$ or when $\omega_{mg} = 2\omega$. In other words, both the one-photon and two-photon resonances are important for SHG. The summation generates terms that are products of transition dipole matrix elements and also sums and differences of dipole moments between ground and excited states as well as between various excited states. This expression simplifies into an intuitively appealing expression if we consider the properties of the molecule to be approximated by a simple two-level model. In this case, one treats a molecule as if having only two levels: a ground state g , and an excited state e . In the two-level model, neglecting the damping terms for simplicity, (7.2) reduces to

$$\beta(-2\omega; \omega, \omega) \propto \frac{\omega_{eg} |\mu_{eg}|^2 (\mu_{gg} - \mu_{ee})}{(\omega_{eg}^2 - \omega^2)(\omega_{eg}^2 - 4\omega^2)} \quad (7.3)$$

In this equation, ω_{eg} is the frequency of the optical transition $g \rightarrow e$, $|\mu_{eg}|^2$ is its oscillator strength, and $(\mu_{gg} - \mu_{ee})$ is the difference between ground and excited state dipole moment. With this expression it is possible to establish trends in relationship between β and the molecular structure in terms of relatively simple physical organic notions. As the oscillator strength or extinction coefficient increases, β is expected to increase. As the difference in polarity between ground and excited state increases, an increase in β is also anticipated. This can be achieved by a more ionic character of the molecular structure (see Fig. 7.3). And, to point it out again, when ω or 2ω is close to the absorption band, β is enhanced.

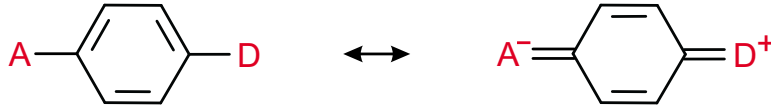


Figure 7.3: Ground state and low-lying charge-transfer excited state of a polar molecular unit. The structure possesses large values of the hyperpolarizability β (adapted from [138]).

In our experiments, we chose $2\omega = \omega_{eg}$ to use the resonance enhancement while there is no one-photon absorption present (see Fig. 7.2). The sensitivity to conformation of the photochromic group is given by μ_{gg} , μ_{ee} , and μ_{eg} being considerably different for *trans* and *cis* conformation.

Simple symmetry considerations lead to the fact that in molecules with inversion symmetry, all tensor elements of β are equal to zero and no second-order nonlinear response exists (in the approximation of only dipolar contributions to the polarization).

The arguments regarding symmetry of the medium extend to the macroscopic nonlinear polarization. To describe the bulk optical nonlinear response \mathbf{P} , one can again use the power series of the field strength in dipole approximation:

$$\mathbf{P} = \chi^{(1)} \cdot \mathbf{E} + \chi^{(2)} : \mathbf{E}\mathbf{E} + \chi^{(3)} : \mathbf{E}\mathbf{E}\mathbf{E} + \dots \quad (7.4)$$

This equation is the bulk analogue to (7.4). The coefficients χ^n describe the n th order bulk susceptibilities. They can be related to the microscopic coefficients α , β and γ of (7.4) if one uses the weak intermolecular coupling limit of an oriented gas model [138]. Under this model, the bulk susceptibilities χ^2 is derived from corresponding microscopic coefficient β with appropriate local field correction:

$$\chi^{(2)}(-\omega_3; \omega_1, \omega_2) = f(\omega_1)f(\omega_2)f(\omega_3) \sum_n \langle \beta^n(\theta, \phi) \rangle \quad (7.5)$$

In this equation, β^n is the microscopic second-order nonlinear coefficient at site n , which is averaged over molecular orientations θ and ϕ , and summed over all sites n . The terms $f(\omega_i)$ are the local field corrections for a wave of frequency ω_i . In a simple schematic way, the local field effect says that the microscopic polarizability of a molecule is affected by the electron density in its neighbors [140, 73]. From (7.5), it is clear that even for molecular systems with $\beta \neq 0$, the bulk second-order nonlinearity determined by the second-order susceptibility χ^2 will be absent if the bulk structure is centrosymmetric, in which case $\sum_n \langle \beta^n(\theta, \phi) \rangle = 0$. Therefore, for a molecular system to give rise to second-order effect, the conditions are that: (i) $\beta \neq 0$, and (ii) the bulk structure is noncentrosymmetric.

Regardless of the symmetry properties of a bulk medium, any inversion symmetry is broken at the surface or at an interface between two dissimilar media. This automatically allows electric dipole, second-order nonlinear optical effects to be observed. In other words, the electric quadratic contribution can dominate completely if sufficient field gradient exists at the interface. Thus, once the symmetry of the medium is correct, SHG is sensitive enough to detect even a submonolayer coverage. Let us mention that (7.5) was derived in limit of weak intermolecular coupling. This assumption will not

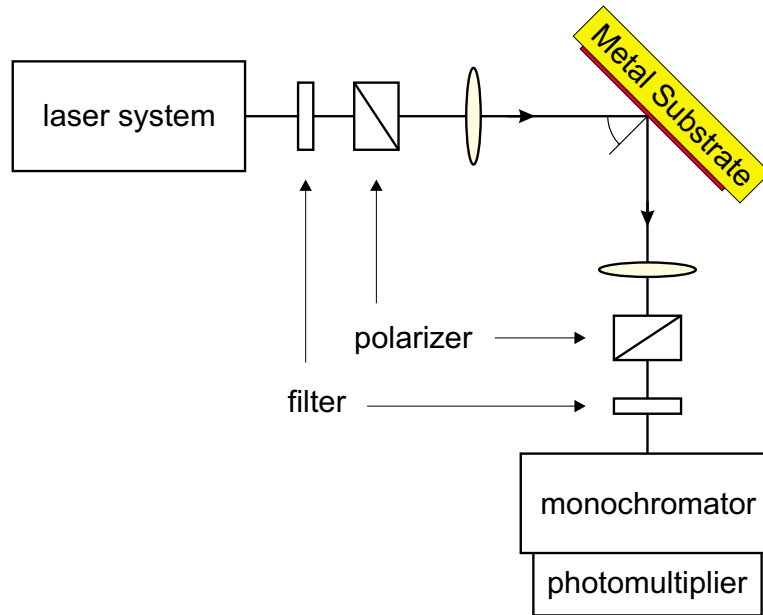


Figure 7.4: Experimental schematic for surface second-harmonic generation by reflection from monolayers on a metal substrate. The exciting laser pulses stem from an Optical Parametric Amplifier (OPA-800C, Spectra Physics), tunable from 300 to 2500nm, and pumped by a regenerative amplifier (Spitfire, Spectra Physics).

hold for densely-packed monolayers as obtained by self-assembly. The molecules of the SAM will interact to form different types of aggregates depending on the arrangement of molecular transition dipole moments [19]. Both, the effect of aggregation and local field effects were shown to strongly enhance SHG response of SAMs relative to the monomeric molecules [110, and references therein].

If the bulk has no inversion symmetry, then of course the surface contribution $\chi_S^{(2)}$, will be overwhelmed by that from the bulk. However, for any isotropic substrate, the surface electric dipole SH signal has only to compete with the bulk quadrupole and magnetic dipole contributions, which are generated by a layer of $\lambda/2\pi$ thickness near the surface. As these contribution can be neglected in most cases, SHG is clearly a viable method for studying adsorbates at centrosymmetric substrates, as in our case SAMs on gold. In this case, the surface susceptibility can be written as

$$\chi_S^{(2)} = \chi_{SA}^{(2)} + \chi_{SS}^{(2)} \quad (7.6)$$

where $\chi_{SA}^{(2)}$ denotes the part arising from adsorbed molecules, and $\chi_{SS}^{(2)}$ from the surface layers of the substrate. If $|\chi_{SA}^{(2)}| \gg |\chi_{SS}^{(2)}|$, or the contribution of $\chi_{SS}^{(2)}$ can be suppressed or subtracted, then the SHG can be used to probe the adsorbate. The total intensity of the second-harmonic signal in reflection geometry has the expression [73]

$$I(2\omega) \propto \frac{\omega^2}{\epsilon_\omega \epsilon_{2\omega}^{1/2} \cos^2 \theta} \left| \chi_{S,\text{eff}}^{(2)} \right|^2 I^2(\omega) A \tau_p \quad (7.7)$$

where $I(\omega)$ is the laser pulse intensity, τ_p the pulse width, and A the beam cross section. $\chi_{S,\text{eff}}$ is the effective surface second-order susceptibility (modified by local-field correction factors [73]), ε_ω is the dielectric constant at frequency ω , and θ is the angle of incidence to the surface.

8 Experimental Results and Discussion

In this chapter, the results of the growth and structural investigations of AzoC₆ monolayers are presented. In STM images, two types of domains are observed which have equal unit cell dimensions and two molecules per unit cell, but a different arrangement of the molecules within the unit cell. The relation of the molecular lattice to the substrate lattice is found to be commensurate. The orientation of the molecules relative to the surface is determined by IR spectroscopy. Finally, SHG is applied to the SAMs to demonstrate its applicability for the future observation of photochromic reactions of monolayers.

8.1 Azobenzene-thiols on Au(111)

Sample Preparation

The molecules of 4-phenylazophenoxyhexane-1-thiol were synthesized by S. STUMPF. For detailed information on the synthesis, we refer to [141]. The SAMs of these molecules were prepared by S. MANNSFELD. For this purpose, mica was freshly cleaved and baked at 750K for 5h in a UHV-chamber. Subsequently, 50 – 100nm gold (Aldrich, 99.5% purity) was deposited onto the mica substrate at a pressure of 10^{-7} mbar. After the deposition, the substrate was annealed at 750K for another 2h. This procedure leads to surfaces with atomically flat terraces and grain sizes of typically several hundred nanometers as shown in Fig. 8.1. The samples were taken out of the chamber immediately before immersion and put into a 1mM solution of AzoC₆ in dichloromethane for about 24h at room temperature. After removal from the solution, the sample was carefully rinsed with the pure solvent and blown dry with N₂ and investigated with STM. Some samples were additionally annealed at 90°C for 12h in order to investigate possible changes in the sample composition following this treatment.

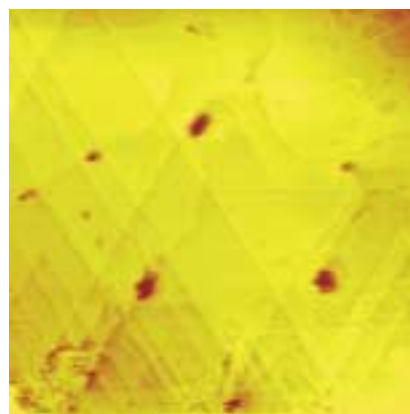


Figure 8.1: STM image of a 433×433 nm detail of a Au(111) surface on mica as used for SAM preparation. One can nicely see the triangular shape of the terraces.

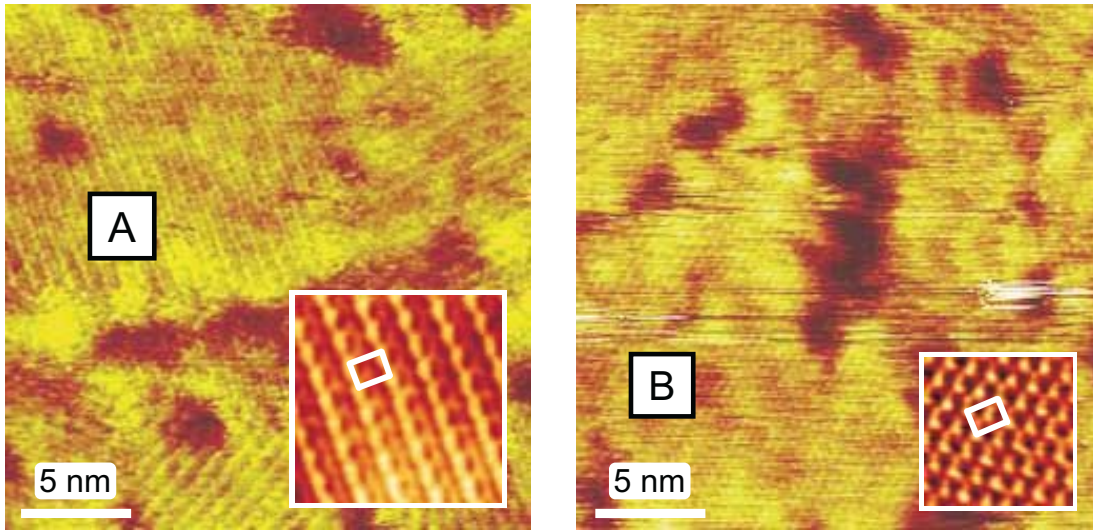


Figure 8.2: STM images showing a SAM of AzoC₆ on Au(111) ($V_t=1.2\text{V}$, $I_t=3\text{pA}$). Two types of domains are occurring: domain type A with a pattern of bright lines; domain type B with uniform contrast. There is an contrast enhanced inset in the lower-right part of each image, showing the two different types of contrast. Both domains feature the same nearly rectangular lattice with $a = 6.3 \pm 0.4\text{\AA}$, $b = 8.2 \pm 0.4\text{\AA}$, $\gamma = 88 \pm 2^\circ$ (white box in the respective inset).

Structural Investigation with STM

S. MANNSFELD obtained all STM images presented herein and was mainly responsible for the structural characterization [141] which will be presented in the following. Figure 8.2 shows two typical STM scans of AzoC₆ SAMs on Au(111). We find a densely packed monolayer consisting of domains with diameters between 10 – 20nm separated by so-called "etch pits" which are known from SAMs of simple alkanethiols and are caused by the relaxation of the Au(111) surface reconstruction upon adsorption of the thiol group [142]. Two types of domains featuring a different molecular contrast were observed. Domains of type A (inset in Fig. 8.2 shows a pattern of bright stripes whereas domains of type B show a more regular tunneling contrast of molecules, i.e. every resolved object appears with the same brightness. The insets were contrast enhanced by application of a correlation averaging procedure [143].

Table 8.1: The experimentally obtained lattice parameters vs. those of the commensurate model unit cell. The matrix C in the last column represents the epitaxial relation between adsorbate and substrate lattice. The matrix elements are all integers which indicates a commensurate relation between the two lattices.

	$a/\text{\AA}$	$b/\text{\AA}$	γ/deg	δ/deg	C
STM	6.3 ± 0.3	8.2 ± 0.3	88 ± 2	38 ± 3	
model	6.3	8.0	87	37	$\begin{pmatrix} -4 & 3 \\ 1 & 1 \end{pmatrix}$

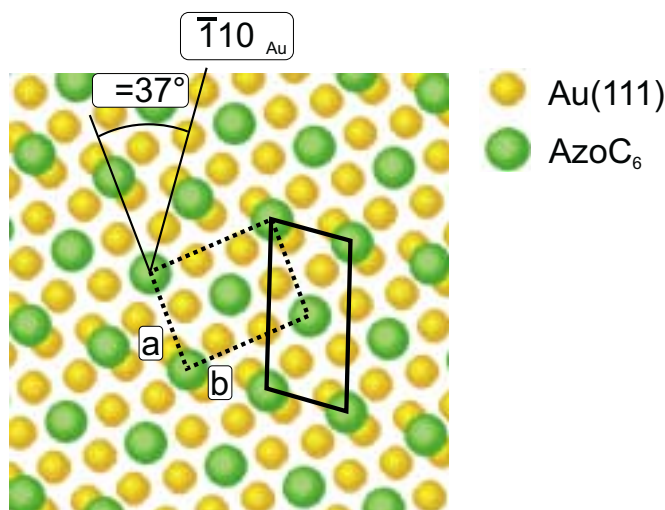


Figure 8.3: Model for the AzoC₆ SAM on Au(111) lattice structure with $a = 6.3\text{\AA}$, $b = 8.0\text{\AA}$, $\gamma = 87^\circ$. The rectangular unit cell (solid lines) in this model corresponds to the measured unit cell (Fig. 8.2). The equivalent dotted unit cell is commensurate with two molecules per unit cell. A commensurate unit cell fits well to the fact that the self-assembly of thiols is usually established by a chemical bond between sulfur and gold.

Measurements in FOURIER-transformed sections showing type *A* domains yield a nearly rectangular lattice with $a = 6.3 \pm 0.4\text{\AA}$, $b = 8.2 \pm 0.4\text{\AA}$, $\gamma = 88 \pm 2^\circ$. The corresponding unit cell area is $52 \pm 6\text{\AA}^2$. Molecular mechanics calculations in which the VAN DER WAALS interactions in an array of rigid *trans*-AzoC₆ molecules (rigid especially means that the alkyl chains could not bend) were optimized, resulted in an area per molecule of $21 - 22\text{\AA}^2$ [141]. This suggests that there are two molecules in the rectangular unit cell.

Additional confirmation for the assumption of two molecules per unit cell comes from the appearance of the molecules in domain type *B*. The lattice parameters in this domain are found to be exactly the same as those of domain type *A*. The only significant difference is that the second molecule in the unit cell appears with the same contrast as the corner molecule. However, in both cases the molecular contrast is not sufficient to allow an exact determination of the mutual arrangement of the two molecules, especially that of the azobenzene moieties, within the unit cell from our STM images.

WOLF et al. [122] not only found similar lattice constants for AzoC₆, but also observed the two domain types *A* and *B*, concluded to a dimer arrangement of azobenzene moieties for domain type *A* from STM image contrast. We sometimes observe tip-induced *A*→*B* domain transitions. We have not observed the opposite change in contrast (*B*→*A* domain transition), but also have no indication for a single equilibrium phase as we still find the two phases in annealed samples with more or less unchanged domain diameters.

To describe the relation between the molecular lattice and the substrate lattice, we define the angle $\delta = \angle(a, \langle \bar{1}10 \rangle_{Au})$, where a is the short lattice vector of AzoC₆. The determination of the substrate lattice relative to the molecular lattice is a difficult task because the SAM completely covers the substrate surface which prevents the direct

observation of the substrate lattice. We find that the angle between the bright stripes of type *A* domains on the same terrace is often very close to 60° . This fact suggests that these domains are equivalent by rotational symmetry of the substrate. This means that the gold substrate is determinant for the orientation of the AzoC_6 lattice. Furthermore, we find domains which can not be transformed into each other via rotation by 60° or 120° , but by a mirroring operation. With the help of this information, we can deduce an angle $\delta = 38 \pm 3^\circ$ for the rectangular lattice of AzoC_6 [141].

To further investigate the structure, we checked whether there is an epitaxial solution for the obtained molecular lattice by using a numerical geometric lattice match model [141]. The calculation yielded exactly one commensurate unit cell (Table 8.1) within the screened lattice parameter range with an angle $\delta = 37^\circ$, which is very close to the experimental value $\delta = 38^\circ$. A model for this commensurate relation with two molecules per unit cell is given in Fig. 8.1. The rectangular unit cell which corresponds to the unit cell deduced from the STM experiments is drawn with solid lines whereas the equivalent commensurate unit cell is drawn with dotted lines.

From the STM investigations we cannot tell the exact position of the second molecule within the unit cell. If we assume a centered lattice (which is suggested by the appearance of domain type *B*), the second molecule in the unit cell would have to bend slightly in order to occupy a chemisorption site equivalent to that of the first molecule. A simple trigonometric estimation for this situation results in a tilt angle of about 8° for the alkyl chain of the second molecule, based on the assumption that the first molecule is standing upright. This angle would still be in agreement with the FTIR-RAS results for AzoC_6 SAMs.

On the other hand, the two molecules in the unit cell could in fact occupy nonequivalent adsorption sites. Although it is widely assumed that the sulfur of the thiol group is covalently bond to Au(111) lattice sites of one type (hcp hollow or bridging sites), more recent investigations have shown that this is not the case at least for alkanethiol SAMs on Au(111) [128, 144, 145, 146]. As the structure of the SAM represents a minimum in the total potential energy of the system which is the *sum* of all substrate \leftrightarrow adsorbate interactions and intermolecular interactions, the energetic gain resulting from a specific arrangement of the two AzoC_6 molecules in the unit cell could be sufficient to "force" the second molecule into a different position relative to the substrate lattice.

Whatever the actual situation is like, the commensurate unit cell represents the "natural" situation of a SAM on gold and does not stress-limit the domain size of the SAM, like it is the case for the *bundle model* proposed for similar azobenzene-functionalised thiols [123, 126, 127]. Due to the striking agreement between the commensurate model and the experimental values we strongly suggest that AzoC_6 SAMs grow in a commensurate structure on Au(111).

8.2 IR Spectroscopy

IR spectroscopy was performed using a Bruker IFS-66 spectrometer equipped with a liquid- N_2 cooled MCT detector and an internal reflection unit Bruker A 518. The optical path was evacuated. An p-polarized beam at an incident angle of 80° to the surface normal was used for measurements in reflection-absorption geometry (FTIR-RAS). The spectra were taken at a 2cm^{-1} resolution, and 1000 interferograms were

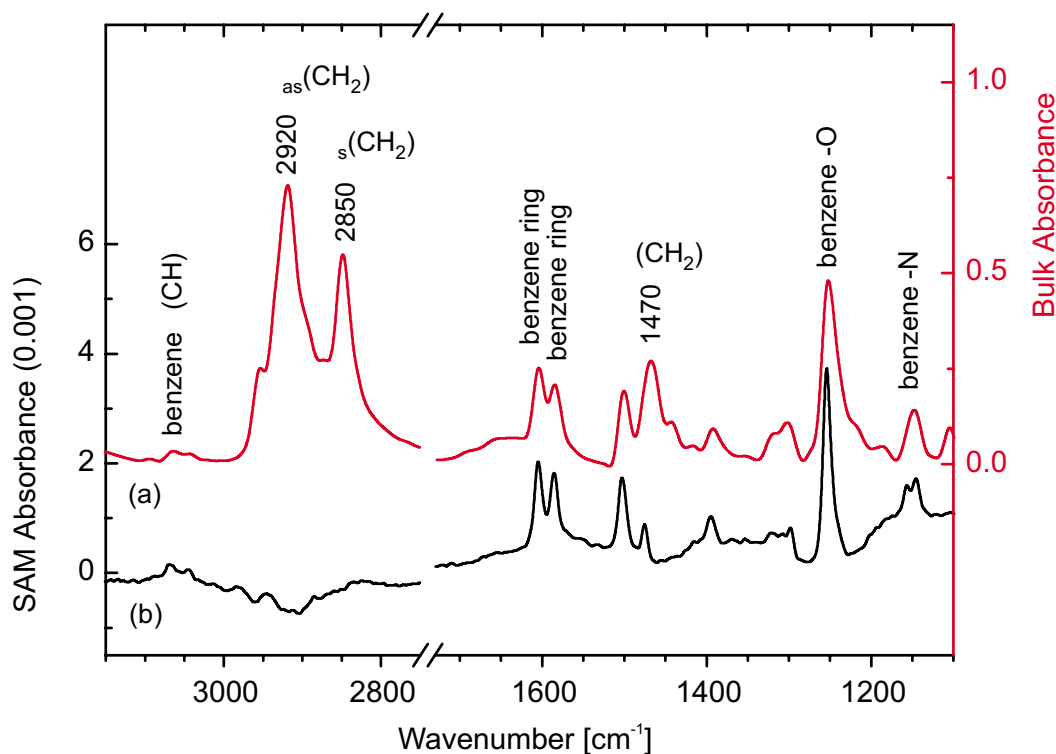


Figure 8.4: Infrared spectra of AzoC₆: (a) FTIR spectrum of the bulk substance (dispersed in KBr, transmission); (b) FTIR-RAS spectrum of the SAM on Au(111). The curves are shifted and scaled for better comparability. General assignment of modes is given on top of the peaks. Observed CH₂ vibrations are: ν - stretching mode, δ - bending mode.

averaged to yield spectra of high signal-to-noise ratio. Reference spectra of the bulk compounds dispersed in KBr were obtained in transmission at normal incidence.

Figure 8.4 shows the FTIR spectrum of the bulk AzoC₆ (dispersed in KBr, transmission) together with the FTIR-RAS spectrum of the corresponding SAM on Au(111). By comparison with literature, e.g. [147], we can assign several of the peaks to the corresponding vibrational modes. The high energy region is mainly governed by the symmetric and antisymmetric stretching modes of the CH₂ group at 2850 and 2920cm⁻¹, respectively. We also observe the CH₂ bending mode δ at 1470cm⁻¹. The modes of the CH₂ group are characteristic for the alkyl chain backbone of the molecules.

We find a good agreement in the low-frequency region (1100–1600cm⁻¹) of the two spectra which is dominated by modes of the azobenzene group. However, the bending mode of the CH₂ group as well as the CH₂ stretching modes in the high energy region are completely absent in the SAM spectrum. The differences between the spectra indicate the alignment of molecules.

Both the transition dipoles of symmetric and antisymmetric CH₂ vibrations (ν_s and ν_{as} , respectively) lie in a plane normal to the long axis of the alkyl chain, as shown in Fig. 8.5. The same holds for the CH₂ bending mode δ . Note that $\nu_s(\text{CH}_2)$ and $\delta(\text{CH}_2)$ are parallel to each other whereas $\nu_{as}(\text{CH}_2)$ stands orthogonal to them. As discussed in Section 7.2, only the E-field component normal to the substrate contributes to the FTIR-RAS signal. Therefore, the transition dipoles of the $\nu_s(\text{CH}_2)$, $\nu_{as}(\text{CH}_2)$, and

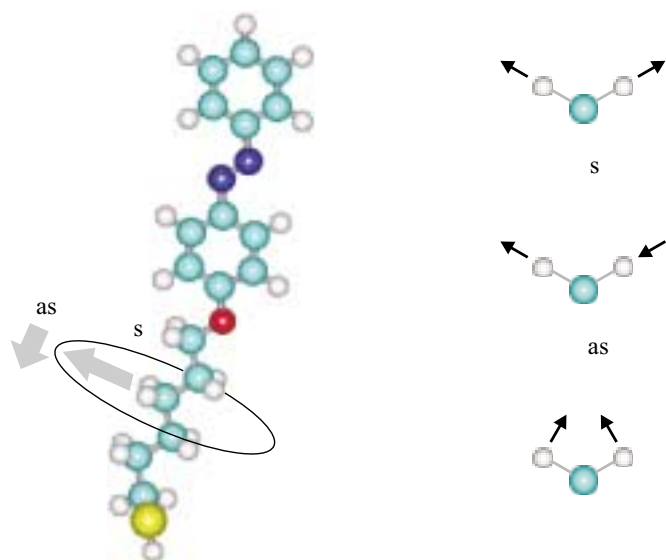


Figure 8.5: Left: AzoC₆ and transition dipoles of some CH₂ modes. Right: Schematics of the CH₂ symmetric and anti-symmetric stretching mode (ν_s and ν_{as} , respectively), and bending mode (δ).

$\delta(\text{CH}_2)$ modes have to be parallel to the substrate to be absent in the spectrum. In other words, the long axis of the alkyl chain has to be nearly normal to the surface. However, the relatively short alkyl chain would only yield small stretching mode signals for other tilt angles close to 0° as well. We assume a large error of $\pm 10^\circ$ for that reason. A tilt angle close to 0° was also reported for annealed layers of AzoC₁₁ by CALDWELL et al [123].

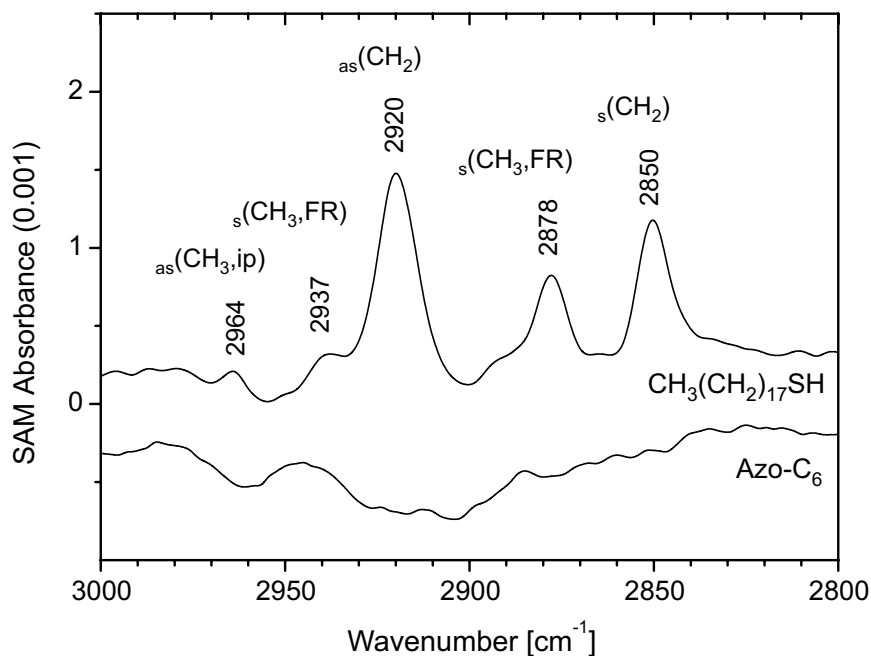


Figure 8.6: FTIR-RAS spectra of comparable SAMs on Au(111): octadecanethiol (top) and AzoC₆ (bottom). CH₃ modes are only expected for octadecanethiol: $\nu_{as}(\text{CH}_3, \text{ip})$ - asymmetric in-plane stretching mode; $\nu_{as}(\text{CH}_3, \text{FR})$ - this symmetric mode is split owing to Fermi resonance interactions with the lower frequency asymmetric deformation mode [149].

For SAMs of plain n -alkanethiols, tilt angles of $\geq 30^\circ$ are observed for $10 \leq n \leq 30$ [148]. For chain lengths $n < 10$ the growth of highly ordered monolayers is increasingly disturbed, since chain-chain interaction can no longer compete with headgroup-substrate interaction. This suggests that the azobenzene head group is important for the ordered growth and upright orientation. Figure 8.6 shows a comparable FTIR-RAS spectrum of an octadecanethiol SAM on Au(111), provided as kind of reference. This molecule exhibits tilt angles from the surface normal of $\sim 30^\circ$ [149] in SAMs on Au(111). The ν_{as} and ν_s CH₂ stretching modes are clearly visible in the respective spectrum. Although octadecanethiol has an alkyl chain three times larger than that of AzoC₆, this confirms that the tilt angle of AzoC₆ in fact has to be much smaller than 30° .

8.3 Second Harmonic Generation (SHG)

Within the time frame of this work, no potentially photo-isomerizable SAMs could be prepared since the substances could not be synthesized in time by our chemistry partners. As already discussed in Section 6.2.2, the photofunctionalization of monolayers incorporating azobenzene units can only be realized by guaranteeing free volume in the film for *trans-cis* photoisomerization since the photochemical process requires a sweep volume. The SAMs of AzoC₆ investigated so far provide an area per molecule of only 26\AA^2 , which is not sufficient for joint photoisomerization of the layer. For this reason, the measurements presented here only show the applicability and the potential of SHG for the investigation of monolayers. Besides that, we find non-quadratic dependence of SHG intensity on excitation density which we discuss at the end of this section.

The measurements for SHG require laser pulses of both high intensity and correctly chosen photon energy in order to resonantly enhance the second-harmonic signal. We use linear polarized laser pulses of about 200fs FWHM and pulse energies of few μJ generated by an optical parametric amplifier (OPA). The OPA is pumped by the regenerative Ti:Sapphire amplifier system running at a repetition rate of 1kHz. We are using a PMT to detect the second-harmonic signal. A small fraction of the exciting beam is split off by a beam splitter for simultaneous measurement of the excitation intensity using a Si photodiode. All signals are collected and amplified by a lock-in amplifier. Measurements are performed on air at room temperature.

The probing photon energy is chosen to be half of the energy of the dominant optical transition $\pi\pi^*$ of the photochromic molecular unit (see Fig. 8.7). For the molecules in solution, we have checked that excitation densities are not critical. That means, we could not observe photoisomerization due to two-photon absorption of the molecules, or even photodegradation.

Figure 8.8 shows the dependence of SHG intensity $I(2\omega)$ on incident probe pulse intensity $I(\omega)$. The given traces stem from two identical substrates (gold on mica), one bare and the other covered by a SAM of AzoC₆.

In general, the contribution to the signal might be threefold: (I) SHG of the monolayer of AzoC₆, (II) surface SHG of the gold surface, and (III), there might be also straylight of the incident fundamental reaching the detector. We can exclude the last contribution to have any significant impact on our measurement: Spectral filtering guarantees that solely SHG signal is detected. The SHG measurement of the substrate

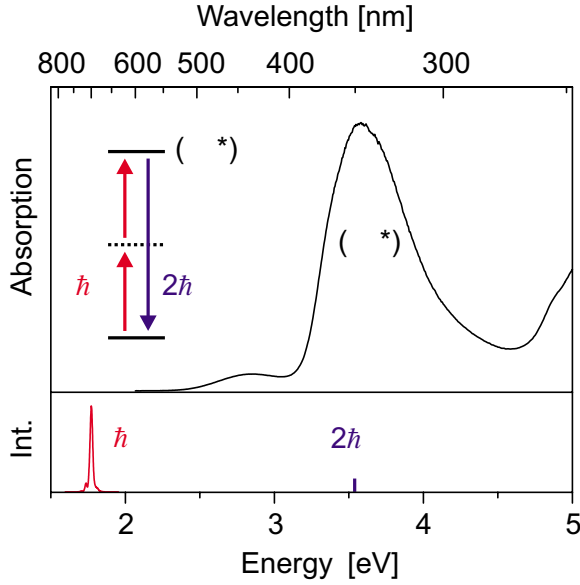


Figure 8.7: Excitation conditions for surface SHG measurements. The inset gives a scheme of the involved levels and photons. Top: Absorption spectrum of AzoC₆ in *trans* configuration (in dichloromethane at room temperature). Bottom: Spectrum of probing laser pulses.

without monolayer was done to distinguish between the contribution of the monolayer and the gold surface. We always find the signal of the SAM of AzoC₆ to be at least one order of magnitude stronger than the signal of the uncovered gold substrate (see Fig. 8.8). For the bare gold surface, the dependence of SHG intensity on excitation density is fitted reasonably by a quadratic function. This is the expected dependence for a second-order nonlinear process as introduced in Sec. 7.3. Surprisingly, the measurements for the monolayer of AzoC₆ follow not the expected nonlinear dependence. We can nicely fit the experimental data by a cubic function. The dynamic range of the measurements allows only variation of the incident intensity within one order of magnitude. Nevertheless, due to the quality of the data we can not ignore the observed cubic dependence.

So, even if the signal stems from SHG, as we know from spectral analysis, it can not be attributed to a second-order process. From literature, we only know of one observation of superquadratic SHG by FROMENKO et al. [150]. The measurements on oxide covered semiconductor surfaces show superquadratic power dependence up to the power of seven. This behavior can be explained to result from photomodulation of an electric field-induced contribution to the second-harmonic response of the system. The interfacial electric field arises from laser-induced charging of oxide traps. It can be described in the electric dipole approximation by a third-order nonlinear process called *electric field-induced second-harmonic generation* (EFISH). By this process, one measures an additional component contributing to SHG, but derived from third-order nonlinearity $\chi^{(3)}$ and the molecular second-order hyperpolarizability γ . Following the nomenclature of Sec. 7.3 the macroscopic polarization is written as [138]:

$$P(2\omega) = \underbrace{\chi^{(2)}(-2\omega; \omega, \omega)E(\omega)E(\omega)}_{2^{\text{nd}} \text{ order SHG}} + \underbrace{\chi^{(3)}(-2\omega; \omega, \omega, 0)E(\omega)E(\omega)E_{\text{DC}}(0)}_{\text{EFISH}} \quad (8.1)$$

where $E_{\text{DC}}(0)$ is a quasi-static electric field over the medium. If E_{DC} is independent on the light field $E(\omega)$ and constant for the measurement, one expects again the usual quadratic SHG dependence. However, the incident electric field of the laser might

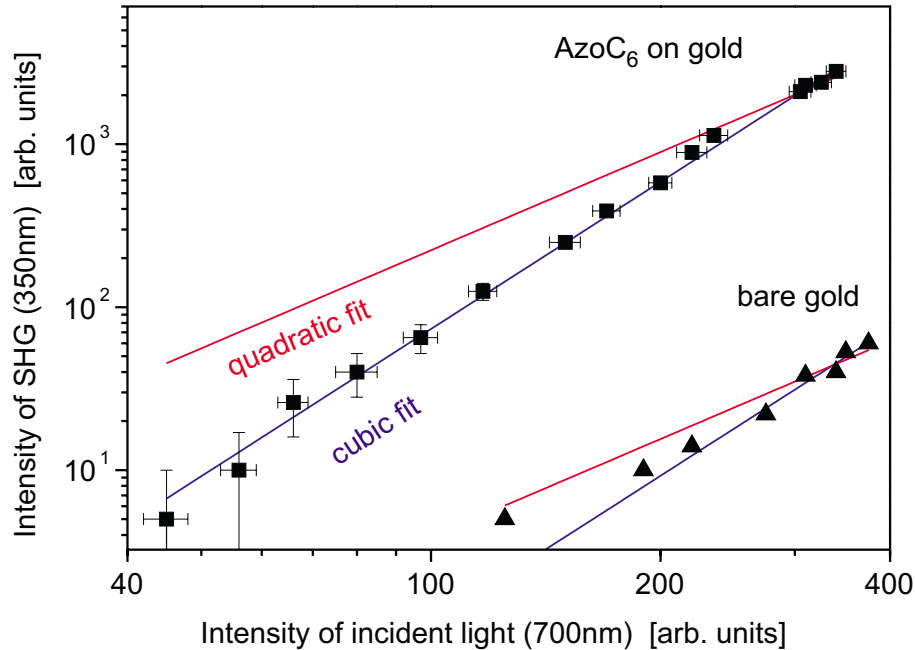


Figure 8.8: Dependence of SHG intensity at 2ω on intensity of incident probe light at ω . The double-logarithmic plot shows results for measurements on a monolayer AzoC₆ on gold (■) and on bare gold (▲). Additionally shown are lines, revealing quadratic and cubic fits.

be also the source of the DC electric field on the surface, or it might modulate an existing quasi-static electric field by screening. The above mentioned experiment [150] impressively shows (SHG dependence up to the power of seven!), that the EFISH term might dominate the polarization response at 2ω . To explain our experiment in this framework, we have to assume the effective electric field at the azobenzene group to be linearly dependent on the incident light field $E_{DC} \propto E(\omega)$. The existence of any laser modulated E_{DC} is hard to motivate for our system. As we have a metal substrate (thin gold film on mica) there are no traps or other "charge separators" to act as source for the DC field. Finally, we have to admit that we can not present a conclusive explanation for an EFISH effect.

There is another contribution to optical nonlinearities that may play an important role. The cascading effect occur when lower-order nonlinearities contribute in a multistep or cascaded manner to higher-order nonlinear effects [138]. These effects arise, when, in addition to the electric laser field applied to the sample, microscopic electric fields are generated by lower-order nonlinear polarizations. Interactions between these field components lead to cascaded polarization terms which are superimposed upon the process. This process was only observed in third-harmonic generation measurements [151], and it is questionable if this process is possible in SHG processes. However, strong local field enhancement is expected on the surface of our samples due to the excitation of *surface plasmon polaritons* (SPP) [152]. SPP is used to denote an evanescent electromagnetic wave, propagating along the surface. It is caused by coupling of a volume electromagnetic wave to the "free electron" like plasma of the metal surface. As we use an angle of incidence $\theta \simeq 45^\circ$ (see Fig. 7.4), SPP might be excited "by accident".

Further measurements, e.g. as function of angle of incidence or polarization are

required for a final interpretation of the surprising power dependence of SHG.

9 Conclusion

Summary

Within the framework of this thesis, we could obtain highly ordered monolayers of photochromic molecules by self assembly. As a first step towards photochromic monolayers, we use simple alkanethiols functionalized with the photoactive azobenzene group (AzoC₆). The thiol group assures the growth on single-crystalline gold surfaces of (111) orientation. We were able to characterize the SAMs concerning their structure.

We find a commensurate growth of the SAM on gold, yielding a nearly rectangular lattice with two molecules in the unit cell. The unit cell area is $52 \pm 6 \text{ \AA}^2$. The molecules were found to stand nearly upright within the SAM. This is distinctly different from plain *n*-alkanethiols which show tilt angles of $\approx 30^\circ$ [148]. For chain lengths $n < 10$ the growth of highly ordered monolayers is increasingly disturbed, since chain-chain interaction can no longer compete with headgroup-substrate interaction. This suggests that the azobenzene group is important for the ordered growth and upright orientation.

Furthermore, we could show second-harmonic generation (SHG) to be a powerful tool for the investigation of monolayers. The sensitivity to the conformation of the photochromic unit makes this technique particularly interesting. Potentially, it opens up the possibility of time-resolved measurements of photochromic reactions of monolayers in the sub-ps time range.

Outlook

The photofunctionalization of monolayers incorporating azobenzene units can only be realized by guaranteeing free volume in the film for *trans-cis* photoisomerization, since the photochemical process requires a sweep volume. The dense packing of AzoC₆ on Au(111), providing only $26 \pm 3 \text{ \AA}^2$ per molecule, prevents the SAM from photoisomerization for steric reason.

The main goal for the future is to obtain not only monolayers of photochromic molecules, but photoswitchable monolayers. All routes to achieve this objective have to assure to provide enough volume per photochromic group. One might apply three different approaches:

- a) Self-assembly of one type of molecules from solution.

We are already working on specially designed molecules incorporating bulky headgroups. This will assure more volume per molecule in the layer, resulting in the required sweep volume.

- b) Isolation of photochromic molecules in densely packed matrix layers.

A different approach to achieve *trans-cis* isomerization of the monolayer is the adsorption of photochromic molecules in intrinsically present vacancies of a densely-packed matrix layer. This isolation approach can be realized following two different strategies: First, by co-adsorption of matrix- and photochromic molecules from solution. Or second, by first adsorbing a defect-rich matrix layer, and subsequent adsorption of the photochromic molecules from a second solution. The matrix might be formed of short-chain alkanethiols. The growth of these molecules is well established and investigated.

- c) Generation of a molecular template by evaporation and subsequent adsorption of photochromic molecules from solution.

This is a new approach not yet discussed in literature. By combining two different methods, it should be possible to achieve regular arrangement of photochromic molecules. In a first step, a monolayer of molecules is evaporated in ultra-high vacuum (UHV). If the molecules are properly chosen, the monolayer shows a regular arrangement of places with unoccupied substrate. In a second step, photochromic molecules will be adsorbed on the substrate at the empty spaces.

Evaporated monolayers of high order usually show dense packing. However, there are first reports in literature about new materials resulting in open layers [153, 154]. The materials used are sub-phthalocyanines showing a three-fold symmetry. On Ag(111), these molecules form open layers of a regular honeycomb structure.

In the near future, research on photochromic SAMs will shift from fundamental understanding of the formation and structure of SAMs towards their potential technological application. Some of the envisioned areas are photo-functional layers, memory layers, sensor surfaces (bio-, chemosensors, mm-wavesensors), surfaces with catalytic activity, and electro-optical layers regulating versatile physical properties including ionic permeability, membrane potential, electroconductivity and alignment of liquid crystals.

To achieve specific properties, a simple photochromic conformational change of the molecular layer is obviously not sufficient. The translation of the photo-functionality into the specific application can be achieved by, e.g. attaching functional groups on the photochromic unit [108]. Additionally, the arrangement of photochromic units relative to each other and the implementation of supramolecular units give the necessary playground for the realization of the given ideas.

Bibliography

- [1] C.K. Chiang, C.R. Fincher, Y.W. Park, A.J. Heeger, H. Shirakawa, E.J. Louis, S.C. Gau, and A.G. MacDiarmid, *Phys. Rev. Lett.* **39** (1977) 1098.
- [2] C.W. Tang and S.A. van Slyke, *Appl. Phys. Lett.* **51** (1987) 913.
- [3] M. Pfeiffer, T. Fritz, J. Blochwitz, A. Nollau, B. Plönnigs, A. Beyer, and K. Leo, in *Festkörperprobleme / Advances in Solid State Physics* **39**, ed. by B. Kramer, published by Vieweg, Braunschweig (1999) 77.
- [4] H. Klauk, D.J. Gundlach, J.A. Nichols, and T.N. Jackson, *IEEE Trans. Electron. Devices* **46** (1999) 1258.
- [5] J.H. Schön, Ch. Kloc, and B. Batlogg, *Phys. Rev. Lett.* **86** (2001) 3843.
- [6] G. Klebe, F. Graser, E. Hädicke, and J. Berndt, *Acta Cryst. B* **45** (1989) 69.
- [7] P.M. Kazmeier and R. Hoffmann, *J. Am. Chem. Soc.* **116** (1994) 9684.
- [8] F. Graser and E. Hädicke, *Liebigs Ann. Chem.* (1984) 483.
- [9] N. Karl and J. Marktanner, *Mol. Cryst. Liq. Cryst.* **315** (1998) 163.
- [10] M. Hoffmann, Ph.D.-thesis, *Frenkel and Charge-Transfer Excitons in Quasi-One-Dimensional Molecular Crystals with strong Intermolecular Orbital Overlap*, Technische Universität Dresden (2000).
- [11] M. Hoffmann, private communication.
- [12] K. Floreck, Diploma-thesis, *Untersuchung zum Zusammenhang zwischen Excitonendynamik und Schichtstruktur in organischen Farbstoffaufdampfschichten*, Technische Universität Dresden (1997).
- [13] P. Peumans, V. Bulović, and S.R. Forrest, *Appl. Phys. Lett.* **76** (2000) 2650.
- [14] D. Meissner and J. Rostalski, *Synthetic Metals* **121** (2001) 1551.
- [15] E. Hädicke and F. Graser, *Acta Cryst. C* **42** (1986) 189.
- [16] H. Haken and H.C. Wolf, *Molekülphysik und Quantenchemie*, published by Springer, Berlin (1998).
- [17] R. Scholz, A. Yu. Kobitski, T.U. Kampen, M. Schreiber, D.R.T. Zahn, G. Jungnickel, M. Elstner, M. Sternberg, and Th. Frauenheim, *Phys. Rev. B* **61** (2000) 13659.
- [18] M. Klessinger and J. Michl, *Excited States and Photochemistry of Organic Molecules*, published by VCH, New York (1995).
- [19] M. Kasha, H.R. Rawls, and M. Ashraf El Bayoumi, *Pure and Applied Chemistry* **11** (1965) 371.

- [20] M. Pope and C. Swenberg, *Electronic Processes in Organic Crystals*, published by Oxford University Press, Oxford (1999).
- [21] J.B. Birks, *Rep. Prog. Phys.* **38** (1975) 903.
- [22] J. Tanaka, *Bull. Chem. Soc. Jpn.* **36** (1963) 1237.
- [23] T.M. Wu, D.W. Brown, K. Lindenberg, *Phys. Rev. B* **47** (1993) 10122.
- [24] K. Puech, H. Fröb, M. Hoffmann, K. Leo, *Opt. Lett.* **21** (1996) 1606.
- [25] R.S. Knox, *Theory of Excitons*, published by Academic Press, San Diego (1963).
- [26] L.E. Lyons, *J. Chem. Soc.* (1957) 5001.
- [27] R.E. Merrifield, *J. Chem. Phys.* **34** (1961) 1835.
- [28] V.M. Agranovich, A.A. Zakhidov, *Chem. Phys. Lett.* **50** (1977) 278.
- [29] A.S. Davydov, *Zhur. Eksptl. Teoret. Fiz.* **18** (1948) 210.
- [30] Ch. Kittel *Einführung in die Festkörperphysik*, published by Oldenbourg, München (1996).
- [31] H. Fidder, J. Knoester, D.A. Wiersma, *J. Chem. Phys.* **95** (1991) 7880.
- [32] M. Hoffmann, K. Schmidt, T. Fritz, T. Hasche, V.M. Agranovich, and K. Leo, *Chem. Phys.* **258** (2000) 73.
- [33] M. Hoffmann, and Z.G. Soos, *Phys. Rev. B* (2002) in press .
- [34] I. Vragović, R. Scholz, and M. Schreiber, *Europhys. Lett.* **57** (2002) 288.
- [35] T.J. Kosic, C.L. Schosser, and D.D. Dlott, *Chem. Phys. Lett.* **96** (1983) 57.
- [36] Y. Toyozawa, Exciton-lattice interaction-fluctuation, relaxation, and defect formation, in *Vacuum Ultraviolet Radiation Physics*, ed. by E.E. Koch, R. Haensel, C. Kunz, published by Pergamon-Vieweg, Braunschweig (1974) 317.
- [37] E.A. Silinsh, V. Čápek, *Organic Molecular Crystals*, published by AIP Press, New York (1994).
- [38] K.S. Song, R.T. Williams, *Self-trapped excitons*, in Springer Series in Solid States **105**, ed. by M. Cardona, published by Springer, Berlin (1993).
- [39] Y. Toyozawa, Localization and Delocalization of an Exziton in the Phonon Field, in *Organic Molecular Aggregates*, ed. by P. Reineker, H. Haken, H.C. Wolf, published by Springer, Berlin (1983) 90.
- [40] A. Matsui, *J. Opt. Soc. Am. B* **7** (1990) 1615.
- [41] B. Walker, H. Port, H.C. Wolf, *Chem. Phys.* **92** (1985) 177.
- [42] L.R. Williams, K.A. Nelson, *J. Chem. Phys.* **87** (1987) 7346.
- [43] T. Kobayashi, A. Shirakawa, H. Matsuzawa, H. Nakanishi, *Chem. Phys. Lett* **321** (2000) 385.
- [44] S.L. Dexheimer, A.D. Van Pelt, J.A. Brozik, B.I. Swanson, *Phys. Rev. Lett.* **84** (2000) 4425.
- [45] S. Tomimoto, H. Nansei, S. Saito, T. Suemoto, J. Takeda, and S. Kurita, *Phys. Rev. Lett.* **81** (1998) 417.

-
- [46] S. Tomimoto, S. Saito, T. Suemoto, K. Sakata, J. Takeda, and S. Kurita, *Phys. Rev. B* **60** (1999) 7961.
- [47] M.H. Henessy, Z.G. Soos, R.A. Pascal Jr., and A. Girlando, *Chem. Phys.* **245** (1999) 199.
- [48] F.F. So and S.R. Forrest, *Phys. Rev. Lett.* **66** (1991) 2649.
- [49] U. Gómez, M. Leonhardt, H. Port, and H.C. Wolf, *Chem. Phys. Lett.* **268** (1997) 1.
- [50] M. Leonhardt, O. Mager, and H. Port, *Chem. Phys. Lett.* **313** (1999) 24.
- [51] A.Yu. Kobitski, R. Scholz, I. Vragović, H.P. Wagner, and D.R.T. Zahn, submitted to *Phys. Rev. B Rapid Comm.* (2002).
- [52] M. Nisoli, S. De Silvestri, O. Svelto, S. Sartania, Z. Cheng, M. Lenzner, Ch. Spielmann, F. Krausz, *Appl. Phys. B* **65** (1997) 5158.
- [53] A.E. Siegman, *Lasers*, published by University Science Books, Sausalito (1986).
- [54] C. Rullière, *Femtosecond Laser Pulses*, published by Springer, Berlin (1998).
- [55] R.L. Fork, O.E. Martinez, and J.P. Gordon, *Opt. Lett.* **9** (1984) 150.
- [56] R.L. Fork, C.H. Brito Cruz, P.C. Becker, and C.V. Shank, *Opt. Lett.* **12** (1987) 483.
- [57] A.M. Weiner, *Rev. Sci. Instrum.* **71** (2000) 1929.
- [58] A.M. Weiner, D.E. Leaird, J.S. Patel, and J.R. Wullert, *Opt. Lett.* **15** (1990) 326.
- [59] P. Tournois, *Opt. Comm.* **140** (1997) 245.
- [60] J.C. Diels, W. Rudolph, *Ultrashort Laser Pulse Phenomena: Fundamentals, Techniques, and Applications on a Femtosecond Time Scale*, published by Academic Press, San Diego (1996).
- [61] M.K. Reed, M.K. Steiner-Shepard, M.S. Armas, and D.K. Negus, *J. Opt. Soc. Am. B* **12** (1995) 2229.
- [62] The calculations were performed using the free and recommendable software macros "LabII". For further information see <http://www.lab2.de>.
- [63] M. Bellini, T.W. Hänsch, *Opt. Lett.* **25** (2000) 1049.
- [64] R. Huber, H. Satzger, W. Zinth, J. Wachtveitl, *Opt. Commun.* **194** (2001) 443.
- [65] T. Wilhelm, J. Piel, E. Riedle, *Opt. Lett.* **22** (1997) 1494.
- [66] G.M. Gale, M. Cavallari, T.J. Driscoll, and F. Hache, *Opt. Lett.* **20** (1995) 1562.
- [67] V. Krylov, O. Ollikainen, J. Gallus, U. Wild, A. Rabene, A. Kalintsev, *Opt. Lett.* **23** (1998) 100.
- [68] S. Lochbrunner, T. Wilhelm, J. Piel, P. Huppmann, S. Spörlein, and E. Riedle, in *Ultrafast Phenomena XI*, ed. by T. Elsaesser, J.G. Fujimoto, D.A. Wiersma, and W. Zinth, published by Springer, Berlin (1998) 57.
- [69] A. Shirakawa, I. Sakane, M. Takasaka, and T. Kobayashi, *Appl. Phys. Lett.* **74** (1999) 2268.
- [70] W.T. Pollard, S.-Y. Lee, and R.A. Mathies *J. Chem. Phys.* **92** (1990) 4012.

-
- [71] J. Chesnoy and A. Mokhtari, *Phys. Rev. A* **38** (1988) 3566.
- [72] W.T. Pollard, H.L. Fragnito, J.-Y. Bigot, C.V. Shank, and R.A. Mathies, *Chem. Phys. Lett.* **168** (1990) 239.
- [73] Y.R. Shen, *The principles of nonlinear optics*, published by John Wiley, New York (1984).
- [74] C.F. Klingshirn, *Semiconductor Optics*, published by Springer, Berlin (1995).
- [75] T. Yajima and Y. Taira, *J. Phys. Soc. Jpn.* **47** (1979) 1620.
- [76] C. Dörnfeld and J.M. Hvam, *IEEE J. Quantum Electr.* **QE-25** (1989) 904.
- [77] W. Demtröder, *Laserspektroskopie, Grundlagen und Techniken*, published by Springer, Berlin (1993).
- [78] see e.g. <http://www.hamamatsu.com>
- [79] K. Seibert Ph.D.-thesis, *Femtosekunden-Spektroskopie an Festkörpern*, RWTH Aachen (1990).
- [80] A. Nollau, M. Hoffmann, K. Floreck, T. Fritz, and K. Leo, *J. Appl. Phys.* **87** (2000) 7802.
- [81] U. Gómez, Ph.D.-thesis, Universität Stuttgart (1997).
- [82] V. Gulbinas, M. Chachisvilis, L. Valkunas, and V. Sundström, *J. Phys. Chem.* **100** (1996) 2213.
- [83] I.V. Ryzhov, G.G. Kozlov, V.A. Malyshev, and J. Knoester, *J. Chem. Phys.* **114** (2001) 5322.
- [84] P.C. Becker, H.L. Fragnito, J.Y. Bigot, C.H. Brito Cruz, R.L. Fork, and C.V. Shank, *Phys. Rev. Lett.* **63** (1989) 505.
- [85] E.T.J. Nibbering, D.A. Wiersma, and K. Duppen, *Phys. Rev. Lett.* **66** (1991) 2464.
- [86] R. Kubo, A stochastic theory of line-shape and relaxation, in *Fluctuations, Relaxation and Resonance in Magnetic Systems*, edited by D. ter Haar, published by Plenum, New York (1962).
- [87] S. Mukamel, *J. Chem. Phys.* **82** (1985) 5398.
- [88] C.J. Bardeen and C.V. Shank, *Chem. Phys. Lett.* **226** (1994) 310.
- [89] A.M. Weiner, S. De Silvestri, and E.P. Ippen, *J. Opt. Soc. Am. B* **2** (1985) 654.
- [90] T.A. Pham, A. Daunois, J.-C. Merle, J. Le Moigne, and J.-Y. Bigot, *Phys. Rev. Lett.* **74** (1995) 904.
- [91] J.M. Turlet, Ph. Kottis, M.R. Philpott, *Advan. Chem. Phys.* **54** (1983) 303.
- [92] J. Kuhl, A. Honold, L. Schultheis, and C.W. Tu, in *Festkörperprobleme / Advances in Solid State Physics* **29**, published by Vieweg, Braunschweig (1989) 157.
- [93] A. Honold, L. Schultheis, J. Kuhl, and C.W. Tu, *Phys. Rev. B* **40** (1989) 6442.
- [94] T. Hasche, T.W. Canzler, R. Scholz, M. Hoffmann, Th. Frauenheim, and K. Leo, *Phys. Rev. Lett.* **86** (2001) 4060.
- [95] W.T. Pollard, S.L. Dexheimer, Q. Wang, L.A. Peteanu, C.V. Shank, and R.A. Mathies, *J. Phys. Chem.* **96** (1992) 6147.

-
- [96] U. Guhathakurta-Ghosh and R. Aroca, *J. Phys. Chem.* **93** (1989) 6125.
- [97] T.W. Canzler, T. Hasche, R. Scholz, and K. Leo, *Physica B* **316-317C** (2002) 48.
- [98] D.A. Tenne, S. Park, T.U. Kampen, A. Das, R. Scholz, and D.R.T. Zahn, *Phys. Rev. B* **61** (2000) 14564.
- [99] M. Elstner, D. Porezag, G. Jungnickel, J. Elsner, M. Haugk, Th. Frauenheim, S. Suhai, and G. Seifert, *Phys. Rev. B* **58** (1998) 7260.
- [100] H.L. Fragnito, J.-Y. Bigot, P.C. Becker, and C.V. Shank, *Chem. Phys. Lett.* **160** (1989) 101.
- [101] T. Joo and A.C. Albrecht, *Chem. Phys.* **173** (1993) 17.
- [102] G. Cerullo, G. Lanzani, M. Muccini, C. Taliani, and S. De Silvestri, *Phys. Rev. Lett.* **83** (1999) 231.
- [103] A. Vierheilg, T. Chen, P. Waltner, W. Kiefer, A. Materny, and A.H. Zewail, *Chem. Phys. Lett.* **312** (1999) 349.
- [104] A.E. Johnson and A.B. Myers, *J. Chem. Phys.* **104** (1995) 2497.
- [105] C.J. Bardeen, Q. Wang, and C.V. Shank, *Phys. Rev. Lett.* **75** (1995) 3410.
- [106] S. Techert, F. Schotte, and M. Wulff, *Phys. Rev. Lett.* **86** (2001) 2030.
-
- [107] K. Blodgett, *J. Am. Chem. Soc.* **57** (1935) 1007.
- [108] S. Flink, F.C.J.M. van Veggel, and D. Reinhoudt, *Adv. Mater.* **12** (2000) 1315.
- [109] F. Schreiber, *Progress in Surface Science* **65** (2000) 151-256.
- [110] A. Ulman *An Introduction to Ultrathin Organic Films: From Langmuir-Blodgett to Self-Assembly*, published by Academic Press, San Diego (1991).
- [111] A. Ulman, *Thin Films, Volume 24: Self-Assembled Monolayers of Thiols*, published by Academic Press, San Diego (1998).
- [112] J.F. Rabek, *Photochemistry and Photophysics*, Volume **II**, published by CRC Press, Boca Raton (1990).
- [113] V. Balzani and F. Scandola, *Supramolecular Photochemistry*, published by Horwood, Chichester (1991).
- [114] G.S. Kumar and D.C. Neckers, *Chem. Rev.* **89** (1989) 1915.
- [115] S. Kurihara, K. Masumoto, and T. Nonaka, *Appl. Phys. Lett.* **73** (1998) 160.
- [116] A. Stracke, J.H. Wendorff, D. Janietz, and S. Mahlstedt, *Adv. Mater.* **11** (1999) 667.
- [117] N. Tamaoki, S. Song, M. Moriyama, and H. Matsuda, *Adv. Mater.* **12** (2000) 94.
- [118] K.L. Prime and G.M. Whitesides, *Science* **252** (1991) 1164.
- [119] P.E. Laibinis, J.J. Hickman, M.S. Wrighton, and G.M. Whitesides, *Science* **245** (1989) 845.
- [120] R.G. Nuzzo, L.H. Dubois, and D.L. Allara, *J. Am. Chem. Soc.* **112** (1990) 558.

- [121] E. Delamarche, B. Michel, H.A. Biebeck, and C. Gerber, *Adv. Mater.* **8** (1996) 719.
- [122] H. Wolf, H. Ringsdorf, E. Delamarche, T. Takami, H. Kang, B. Michel, C. Gerber, M. Jaschke, H.-J. Butt, and E. Bamberg, *J. Phys. Chem.* **99** (1995) 7102.
- [123] W.B. Caldwell, D. J. Campbell, K. Chen, B.R. Herr, C.A. Mirkin, A. Malik, M.K. Durbin, P. Dutta, and K.G. Huang, *J. Am. Chem. Soc.* **117** (1995) 6071.
- [124] T. Takami, E. Delamarche, B. Michel, C. Gerber, H. Wolf, and H. Ringsdorf, *Langmuir* **11** (1995) 3876.
- [125] E. Delamarche and B. Michel, *Thin Solid Films* **273** (1996) 54.
- [126] R. Wang, T. Iyoda, L. Jiang, K. Hashimoto, and A. Fujishima, *Chem. Lett.* (1996) 1005.
- [127] K. Tamada, J. Nagasawa, F. Nakanishi, K. Abe, T. Ishida, M. Hara, and W. Knoll, *Langmuir* **14** (1998) 3264.
- [128] P. Fenter, A. Eberhardt, and P. Eisenberger, *Science* **266** (1994) 1216.
- [129] S.W. Han, C.H. Kim, S.H. Hong, Y.K. Chung, and K. Kim, *Langmuir* **15** (1999) 1579.
- [130] T. Sato, Y. Ozaki, and K. Iriyama, *Langmuir* **10** (1994) 2363.
- [131] R. Wang, L. Jiang, T. Iyoda, D.A. Tryk, K. Hashimoto, and A. Fujishima, *Langmuir* **12** (1995) 2052.
- [132] S.D. Evans, S.R. Johnson, H. Ringsdorf, L.M. Williams, and H. Wolf, *Langmuir* **14** (1998) 6436.
- [133] S.-K. Oh, M. Nakagawa, and K. Ichimura, *Chemistry Lett.* **4** (1999) 349.
- [134] R. Staub and D. Alliata, *Rev. Sci. Instrum.* **66** (1995) 2513.
- [135] M.K. Debe, *Progress in Surface Science, Volume 24: Optical Probes of Organic Thin Films: Photons-in, Photons-out*, published by Pergamon Press, New York (1987).
- [136] M. Born and E. Wolf, *Principles of Optics*, published by Cambridge University Press, Cambridge (1999).
- [137] J.D.E. McIntyre and D.E. Aspnes, *Surf. Sci.* **24** (1971) 417.
- [138] P.N. Prasad and D.J. Williams, *Introduction to Nonlinear Optical Effects in Molecules and Polymers*, published by Wiley and Sons, New York (1991).
- [139] P.N. Prasad, Nonlinear Optical Effects in Organic Materials, in *Contemporary Nonlinear Optics*, edited by G.P. Agrawal and R.W. Boyd, published by Academic Press, San Diego (1992).
- [140] P. Ye and Y.R. Shen, *Phys. Rev. B* **28** (1983) 4288.
- [141] S.C.B. Mannsfeld, T.W. Canzler, T. Fritz, H. Proehl, S. Stumpf, G. Goretzki, K. Gloe, and K. Leo, *J. Phys. Chem. B* **106** (2002) 2255.
- [142] G.E. Poirier, *Langmuir* **13** (1997) 2019.
- [143] F. Sellam, T. Schmitz-Hübsch, M. Toerker, S. Mannsfeld, H. Proehl, T. Fritz, and K. Leo, *Surf. Sci.* **478** (2001) 113.

-
- [144] R. Staub, M. Toerker, T. Fritz, T. Schmitz-Hübsch, F. Sellam, and K. Leo, *Langmuir* **14** (1998) 6693.
- [145] M.S. Yeganeh, S.M. Dougal, R.S. Polizzotti, and P. Rabinowitz, *Phys. Rev. Lett.* **74** (1995) 1811.
- [146] P. Fenter, F. Schreiber, L. Berman, G. Scoles, P. Eisenberger, and M. Bedzyk, *Surf. Sci.* **412/413** (1998) 213.
- [147] B. Schrader, *Infrared and Raman Spectroscopy: Methods and applications*, published by VCH, Weinheim (1995).
- [148] P. Fenter, A. Eberhardt, K.S. Liang, and P. Eisenberger, *J. Chem. Phys.* **106** (1997) 1600.
- [149] M. Porter, T. Bright, D. Allara, and C. Chidsey, *J. Am. Chem. Soc.* **109** (1987) 3559.
- [150] V. Fomenko, J.-F. Lami, and E. Borguet, *Phys. Rev. B* **63** (2001) 121316(R).
- [151] G.R. Meredith and B. Buchalter *J. Chem. Phys.* **78** (1983) 1938.
- [152] *Surface Polaritons*, ed. by V.M. Agranovich and D.L. Mills, published by North-Holland, Amsterdam (1982).
- [153] H. Suzuki, S. Berner, M. Brunner, T.A. Jung, H. Yanagi, D. Schlettwein, and H.-J. Güntherodt, *11th Intern. Conf. on Scanning Tunneling Microscopy/Spectroscopy and related Techniques*, Book of Abstracts (2001) 81.
- [154] S. Berner, M. Brunner, L. Ramoino, H. Suzuki, T.A. Jung and H.-J. Güntherodt, *11th Intern. Conf. on Scanning Tunneling Microscopy/Spectroscopy and related Techniques*, Book of Abstracts (2001) 148.

Publications

Parts of this work have been published or presented:

Articles

- I. T. Hasche, T.W. Canzler, R. Scholz, M. Hoffmann, K. Schmidt, Th. Frauenheim, and K. Leo, Coherent External and Internal Phonons in Quasi-One-Dimensional Organic Molecular Crystals, *Phys. Rev. Lett.* **86** (2001) 4060.
- II. T. Hasche, T.W. Canzler, R. Scholz, and K. Leo, Coherent Phonons in Quasi-One-Dimensional Organic Crystals, *J. Lumin.* **94-95** (2001) 673.
- III. M. Hoffmann, T. Hasche, K. Schmidt, T.W. Canzler, V.M. Agranovich, and K. Leo, Excitons in quasi-one-dimensional crystalline perylene derivatives: Band structure and relaxation dynamics, *Int. J. Mod. Phys. B* **15** (2001) 3597.
- IV. S.C.B. Mannsfeld, T.W. Canzler, T. Fritz, H. Proehl, and K. Leo, S. Stumpf, G. Goretzki, and K. Gloe, The structure of [4-(Phenylazo)phenoxy]hexane-1-thiol Self-Assembled Monolayers on Au(111), *J. Phys. Chem. B* **106** (2002) 2255.
- V. T.W. Canzler, T. Hasche, R. Scholz, and K. Leo, Coherent Phonon Wavepackets in Quasi-1D Organic Molecular Crystals, *Physica B* **316-317C** (2002) 48.

Conference contributions

- I. K. Schmidt, T.W. Canzler, M. Hoffmann, T. Hasche, and K. Leo, Lowest energy excitons in thin films of perylene derivatives (poster), *XVIII. IUPAC Symposium on Photochemistry*, Dresden (Germany), 2000.
- II. M. Hoffmann, T. Hasche, K. Schmidt, T.W. Canzler, V.M. Agranovich, and K. Leo, Excitons in quasi-one-dimensional crystalline perylene derivatives: band structure and relaxation dynamics (talk), *International Conference on Excitonic Processes in Condensed Matter (EXCON 2000)*, Kobe (Japan), 2000.
- III. T.W. Canzler, T. Hasche, R. Scholz, M. Hoffmann, K. Schmidt, and K. Leo, Coherent Phonon Oscillations in Quasi-One-Dimensional Organic Molecular Crystals (talk), *MRS Fall Meeting 2000*, Boston (USA), 2000.

-
- IV. T. Hasche, T.W. Canzler, R. Scholz, and K. Leo, Coherent phonons in quasi-one-dimensional organic crystals (talk), *Int. Conference on Dynamical Processes in Excited States of Solids (DPC'01)*, Lyon (France), 2001.
 - V. T.W. Canzler, T. Hasche, R. Scholz, and K. Leo, Coherent External and Internal Phonon Oscillations in Organic Molecular Crystals (talk), *Quantum Electronics and Laser Science Conference (QELS 2001)*, Baltimore (USA), 2001.
 - VI. T. Hasche, T.W. Canzler, M. Hoffmann, and K. Leo, Ultrafast relaxation of free excitons in quasi-1D organic molecular crystals (talk), *Quantum Electronics and Laser Science Conference (QELS 2001)*, Baltimore (USA) 2001.
 - VII. T.W. Canzler, T. Hasche, R. Scholz, and K. Leo, Coherent Inter- and Intramolecular Phonons in Quasi-1D Organic Crystals (talk), *10th Int. Conference on Modulated Semiconductor Structures (MSS 10)*, Linz (Austria), 2001.
 - VIII. T.W. Canzler, T. Hasche, R. Scholz, and K. Leo, Coherent Phonon Wavepackets in Quasi-1D Organic Molecular Crystals (invited talk), *10th Int. Conference on Phonon Scattering in Condensed Matter (Phonons 2001)*, Hanover, NH (USA), 2001.

Danksagung

Ich möchte mich an dieser Stelle bei all denen bedanken, die zum Erfolg dieser Arbeit beigetragen haben. Insbesondere gilt mein Dank:

Meinem Betreuer Prof. Karl Leo für seine stete Unterstützung bei dieser Arbeit. Sein vorbildhafter Führungsstil ist ein Hauptgrund für die angenehme Arbeitsatmosphäre am *Institut für Angewandte Photophysik*. Insbesondere sein Eifer im Eintreiben von Forschungs-, Berufungs- und nicht zuletzt Preisgeldern ermöglichte eine traumhafte Ausstattung des Organik-Kurzzeitlabors.

Meinem Mentor und Mitstreiter Dr. Tom Hasche für die harmonische Zusammenarbeit an allen Experimenten zur Ultrakurzzeitphysik. Sein umfangreiches Wissen zur nicht-linearen Optik war die Basis für den zügigen Aufbau der entsprechenden Experimente. Zudem hat er die mit Abstand meisten Diskussionen mit mir ausgefochten.

Meinen Kollegen der Ultrakurzzeit-Arbeitsgruppe Ben Rosam, Dirk Meinhold, Falk Löser und Christian Holfeld für die unzählige Diskussionen und Ratschläge. Danke auch für die jederzeit unkomplizierte Hilfe und ungewöhnlich viel Spass.

Dr. Torsten Fritz für die Betreuung des Projektes zu den selbst-assemblierten Monoschichten (SAM) photochromer Moleküle und den gern geteilten Erfahrungsschatz zu verschiedensten Bereichen der Physik und Chemie.

Meinem Kollegen Stefan Mannsfeld für seinen großen Anteil an dem SAM-Projekt und die gute Zusammenarbeit.

Dr. Reinhard Scholz (Chemnitz) für den theoretischen Beitrag zu den kohärenten Phononen.

Prof. Vladimir M. Agranovich und Dr. Michael Hoffmann für ihre theoretischen Beiträge zum Verständnis der optischen Eigenschaften organischer Kristallsysteme und ihre Geduld mit Experimentalphysikern.

Prof. Vadim G. Lyssenko (Chernogolovka, Russland) für herzerfrischende, stimulierende Diskussionen über mögliche Messungen und Messtechniken.

Prof. Vladimir M. Agranovich (Troitsk, Russland) und Prof. Harald Giessen (Bonn) für die Begutachtung dieser Arbeit.

Prof. Norbert Karl (Stuttgart) für die Bereitstellung von MePTCDI Einkristallen und deren Untersuchung mittels Röntgenbeugung.

Der Arbeitsgruppe Organik für die Bereitstellung von MePTCDI Dünnschichtproben.

So einigen hilfreichen Spezialisten: Kai Schmidt (Computer), Volker Trepte (Mechanik), Sven Trogisch (Elektronik), Eva Schmidt (Verwaltung).

Der Deutschen Forschungsgemeinschaft für finanzielle Unterstützung.

Und zu guter Letzt meinen Freunden und meiner Familie.

Versicherung

Hiermit versichere ich, dass ich die vorliegende Arbeit ohne unzulässige Hilfe Dritter und ohne Benutzung anderer als der angegebenen Hilfsmittel angefertigt habe; die aus fremden Quellen direkt oder indirekt übernommenen Gedanken sind als solche kenntlich gemacht. Die Arbeit wurde bisher weder im Inland noch im Ausland in gleicher oder ähnlicher Form einer anderen Prüfungsbehörde vorgelegt. Ich erkenne die Promotionsordnung der Technischen Universität Dresden an.

Diese Arbeit wurde am Institut für Angewandte Photophysik der Technischen Universität Dresden unter der wissenschaftlichen Betreuung von Prof. Dr. Karl Leo angefertigt.

Dresden, den 15.07.2002

(Tobias W. Canzler)